

Development of high throughput X-ray instrumentation for fast timing studies

Dissertation
zur Erlangung des Grades eines
Doktors der Naturwissenschaften
der Fakultät für Mathematik und Physik
der Eberhard-Karls-Universität Tübingen

vorgelegt von

Michael Martin

aus Mutlangen
2009

Selbstverlegt von: M. Martin, Pfalzgrafenring 27, 72119 Ammerbuch
Tag der mündlichen Prüfung: 9. Oktober 2009
Dekan: Prof. Dr. W. Knapp
1. Berichterstatter: Prof. Dr. A. Santangelo
2. Berichterstatter: Prof. Dr. K. Werner

Zusammenfassung

Detektoren auf Silizium-Basis bilden das Rückgrat der beobachtenden Röntgenastronomie im Energiebereich zwischen 0,1 und 20 keV. Sie kombinieren gute Energieauflösung, die nahe am Fano-Limit liegt, mit hoher Quanteneffizienz und nutzen den Vorteil, dass durch die Verwendung von Silizium in der Halbleiterindustrie eine Vielzahl von hochentwickelten Prozesstechnologien zur Verfügung stehen. Dadurch wird die Entwicklung von Instrumenten mit hoher Orts- und Spektralauflösung ermöglicht, die optimal auf die gewünschten Eigenschaften des Teleskops abgestimmt sind.

In der kommenden Generation von Röntgensatelliten, wie das *International X-ray Observatory (IXO)* und *Simbol-X*, werden unter anderem ebenfalls abbildende Detektoren auf Silizium-Basis verwendet werden. *IXO* soll das nächste große gemeinsame Röntgenobservatorium der NASA, ESA und JAXA werden. Mit einer geplanten effektiven Sammelfläche von 3 m^2 bei 1,25 keV und fünf unterschiedlichen Instrumenten, die insgesamt den Energiebereich zwischen 0,1 und 40 keV abdecken, wird *IXO* in der Lage sein, die Entwicklung des „heißen“ Kosmos zu beobachten und die Physik in Regionen extremer Bedingungen zu untersuchen.

Als eines der Hauptinstrumente von *IXO* ist der *Wide Field Imager (WFI)* vorgesehen. Sein Detektor ist realisiert als „aktiver“ Pixel-Sensor, bestehend aus 1024×1024 Pixeln, in welchen die erste Verstärkerstufe bereits integriert ist. Diese besteht im Wesentlichen aus einem vollständig verarmten p-Kanal Feld Effekt Transistor (DePFET). Diese Art von Detektor steht im Mittelpunkt dieser Arbeit. Für die Beobachtung von hellen Quellen ist in der gegenwärtig geplanten Satellitenkonfiguration zusätzlich der *High Time Resolution Spectrometer (HTRS)* vorgesehen.

Das Hauptziel dieser Arbeit besteht in der Abschätzung der zu erwartenden Leistungsfähigkeit der DePFET-Matrizen, die für *IXO* und *Simbol-X* entwickelt werden, durch eine Kombination aus Messungen und Simulationen. In Zusammenarbeit mit dem Halbleiterlabor der Max-Planck-Institute, wurde dazu am Institut für Astronomie und Astrophysik der Universität Tübingen ein Teststand aufgebaut,

der es erlaubt, Prototypen der DePFET-Matrizen zu betreiben und zu untersuchen. Umfangreiche Messungen wurden unter verschiedenen Bedingungen wie z.B. Temperatur, Belichtung und Betriebsparametern des Detektors durchgeführt. Aspekte wie Zeit- und Energieauflösung, Ladungsverteilung und Pile-up wurden experimentell erforscht.

Es wurde ein Monte-Carlo Simulationscode entwickelt, um zahlreiche Aspekte von Halbleiterdetektoren zu untersuchen. Der Code ermöglicht eine realistische Darstellung von Quellspektren und erlaubt die Simulation von zeitlich variablen Quellen unter Berücksichtigung der entsprechenden Statistik. Anhand der am IAAT durchgeführten Messungen wurde der Code hinsichtlich Energie- und Zeitaufklärung, sowie der Ladungsverteilung überprüft. Die gemessenen Werte des Detektors unter Pile-up Bedingungen, welche durch die Belichtung mit hellen Quellen verursacht werden, konnten durch den Simulationscode reproduziert werden.

Die Übertragung der Simulation auf den WFI von *IXO* zeigt, dass die Beobachtungsmöglichkeiten von Galaktischen Röntgenquellen wie z.B. Röntgendoppelsternen und Überresten von Supernovae stark eingeschränkt sind, da die typischen Leuchtkräfte dieser Objekte die Leistungsfähigkeit der Detektoren übersteigen. Wir haben deshalb den Simulationscode um den HTRS erweitert. Wir kommen anhand unsere Ergebnisse zu dem Schluss, dass ein Instrument wie der HTRS, welches bauartbedingt hohe Zählraten mit großer Effizienz messen kann, unerlässlich ist, um mit *IXO* Galaktische Quellen beobachten zu können.

Abstract

Silicon based detectors are the current working horses of observational X-ray astronomy in the 0.1–20 keV energy band. They offer a nearly Fano limited energy resolution in combination with a high quantum efficiency and have the advantage that, through the commercial usage of silicon in the semiconductor industry, a multitude of sophisticated processing technologies are available. This allows to build instruments with high spectral and spatial resolution designed to match the characteristics of the telescopes.

The next generation X-ray missions like the *International X-ray Observatory (IXO)* and *Simbol-X* will use, among others, silicon based imaging detectors. *IXO* is currently studied as the next large aperture X-ray mission of NASA, ESA and JAXA. With a proposed large effective area of 3 m² at 1.25 keV and a set of five different instruments covering together the energy range from 0.1–40 keV, *IXO* will be able to observe the evolution of the “hot” universe and to probe the physics of extreme environments.

One of *IXO*’s main instruments will be the Wide Field Imager, an active pixel sensor where in each of its 1024 × 1024 pixels the first-amplifier stage is already integrated. The WFI pixels are realized as Depleted P-channel Field Effect Transistors (DePFET) which stand in the focus of this thesis. For the observation of bright sources, a High Time Resolution Spectrometer (HTRS) is included in the current model payload.

The main goal of this thesis is to estimate the expected performance of the DePFET matrices used for *IXO* and *Simbol-X* through a combination of measurements and simulations. In collaboration with the Max-Planck-Institut Halbleitertechnik, we have built a test setup at the Institut für Astronomie und Astrophysik der Universität Tübingen (IAAT) to operate and study laboratory prototypes of the DePFET detectors. Extensive measurements under different conditions of, e.g., temperature, exposure and detector biasing were conducted. Aspects like time and energy resolution, charge splitting and pile-up were experimentally investigated.

A Monte-Carlo based simulation code was developed to study the various aspects

of semiconductor based detectors. The code allows a realistic simulation of source spectra and can handle time variable sources with the proper statistics. The code was validated with laboratory measurements taken at IAAT, with respect to time and energy resolution, as well as charge splitting. The influence of pile-up in the detector when illuminated by a bright source was reproduced by the simulations.

The extrapolation from the laboratory simulations shows that pile-up limits the ability of the *IXO* WFI to observe Galactic X-ray sources, e.g., X-ray binaries and Supernova remnants, since the typical luminosities of these objects cause a severe deterioration of the detector performance. We therefore extended our simulations to the HTRS and we conclude that this instrument, with its intrinsic capability to efficiently measure high count rates, is vital for the observation of bright Galactic sources with *IXO*.

*To Wiebke
and
my parents*

Contents

Zusammenfassung	3
Abstract	5
1 Introduction	17
1.1 Origin of X-ray Astronomy	17
1.2 Future prospects	19
1.3 Goals and outline of the thesis	20
2 Future missions	23
2.1 The International X-ray Observatory	23
2.1.1 Scientific Objectives	24
2.1.2 Mission Design	27
2.1.3 Optics	28
2.1.4 Focal Plane	29
2.2 Simbol-X	34
2.2.1 Overview	34
2.2.2 Scientific Objectives	35
2.2.3 Focal Plane	35
3 Semiconductor Detectors	37
3.1 Introduction	37
3.1.1 Interaction of photons with matter	39
3.2 Semiconductor Detectors	43
3.2.1 pn-Junction	46
3.2.2 Charge collection	48
3.2.3 Ionization Statistics	50
3.2.4 Sideways Depletion Principle	52
3.3 MOSFET	54

4	The DePFET Detector	59
4.1	General considerations	59
4.2	The DePMOSFET	61
4.2.1	Operating principles	63
4.2.2	DePFET variants	66
4.3	Macropixel	68
4.4	DePFET Matrices	69
4.4.1	Hybrid	70
4.4.1.1	Matrix	70
4.4.1.2	CAMEX IC	72
4.4.1.3	Switcher II IC	78
4.5	Data acquisition system	81
4.5.1	Sequencer	83
4.5.2	XBoard	84
4.5.3	PixBoard	85
4.5.4	ADC	87
4.5.5	Power supplies	88
4.5.6	Chopper wheel	88
5	Measurements	91
5.1	General remarks	91
5.2	Standard measurements	92
5.2.1	HLLSAS Analysis	93
5.2.2	Front-/Back illumination measurements	96
5.2.3	Spectral analysis	100
5.2.4	Backside voltage scans	103
5.2.5	Temperature dependency of the offset	105
5.2.6	Incomplete Clear	108
6	Simulations	111
6.1	Pile-up in imaging detectors	111
6.1.1	Energy pile-up	113
6.1.2	Pattern pile-up	113
6.2	The simulation package	115
6.2.1	Simulation Code	115
6.2.2	Input Parameters	121
6.2.3	Response Files	123
6.3	Verification of the code	126
6.3.1	Timing performance	126
6.3.2	Charge Splitting	129

6.3.3	Pile-up	134
6.3.4	Spectral comparison	136
6.4	<i>IXO</i> and <i>Simbol-X</i> simulations	139
6.4.1	Motivation	139
6.4.2	<i>IXO</i> pile-up estimations	139
6.4.3	<i>Simbol-X</i> pile-up estimations	145
6.5	Simulation of astrophysical X-ray sources	146
6.5.1	The Crab	147
6.5.2	Neutron star eclipses	150
6.5.3	X-ray bursts	151
7	Summary and Outlook	155
7.1	Summary and Conclusions	155
7.2	Outlook	156
	Bibliography	159
	Acknowledgements	165
	Curriculum vitae	167
	Lebenslauf	168

List of Figures

2.1	Artistic view of <i>IXO</i>	24
2.2	<i>IXO</i> AGN study overview	26
2.3	<i>IXO</i> effective areas	28
2.4	Slumped glass and silicon pore optics	29
2.5	HTRS and WFI/HXI	30
2.6	<i>IXO</i> flight mirror assembly	32
2.7	Artistic view of <i>Simbol-X</i>	34
2.8	<i>Simbol-X</i> detectors	36
3.1	Photon interaction processes	40
3.2	Photon absorption coefficient of silicon	41
3.3	Compton scattering	42
3.4	Occupation probability of semiconductors	44
3.5	Pn-junction under different biasing conditions	47
3.6	Sideways depletion principle	52
3.7	Metal-Insulator-Semiconductor interface	55
3.8	Cross section through a p-channel MOSFET	56
3.9	Current-Voltage characteristic of a p-channel MOSFET	57
4.1	Model of a DePFET pixel	61
4.2	Connection scheme for source follower readout	63
4.3	Signal sequence for the DePFET readout	65
4.4	Layout of the PXD05 DePFET	67
4.5	<i>Simbol-X</i> macropixel layout	69
4.6	View of the hybrid	70
4.7	Pixel interconnection scheme	71
4.8	CAMEX functional blocks	73
4.9	CAMEX shift register content	74
4.10	CAMEX source follower readout scheme	75
4.11	CAMEX linearity and gain curves	77
4.12	SWITCHER II IC functional drawing	78
4.13	SWITCHER II IC interconnection scheme	79
4.14	SWITCHER II IC voltage levels and switching ranges	80

4.15	Flowchart of the experimental setup	82
4.16	View of the laboratory setup	83
4.17	XBoard and PixBoard	86
4.18	Chopper wheel elevation plot	89
4.19	Shutter wheels with 4 & 16 holes	90
5.1	Offset-, residual offset-, and noise map	94
5.2	Front vs. back illumination single event spectrum	98
5.3	Front vs. back illumination spectrum	99
5.4	DePFET matrix 2×2 pixel layout	101
5.5	Gain linearity plots	102
5.6	Back voltage scan split ratios	104
5.7	Back voltage scan energy resolution	105
5.8	Offset and gain vs. temperature	106
5.9	Low energy spectrum with clear correlations	108
5.10	Clear correlation distribution	109
6.1	Epatplot of RS Oph	114
6.2	Valid pattern types	117
6.3	Implementation of the clear process	119
6.4	Simulation flowchart	120
6.5	HTRS geometry	122
6.6	<i>IXO</i> and <i>Simbol-X</i> response	124
6.7	Laboratory Response	125
6.8	Detected pulse periods	127
6.9	Reconstructed pulse profiles	128
6.10	Split fraction for different parameters	129
6.11	Split ratio vs. frame time for low count rates	132
6.12	Split ratio vs. frame time for high count rates	133
6.13	Laboratory simulation count rates	134
6.14	Valid count rates for different source-distance combinations	135
6.15	Simulated single event spectrum	137
6.16	Non-linearity for different pattern types	138
6.17	<i>IXO</i> efficiencies	140
6.18	Pattern fractions of the <i>IXO</i> window mode	142
6.19	PSF for different window mode count rates	143
6.20	HTRS efficiencies	144
6.21	Efficiency comparison between <i>IXO</i> and <i>Simbol-X</i>	146
6.22	Crab spectrum from <i>IXO</i> window mode	147
6.23	Inter-frame split spectrum	149
6.24	HTRS crab spectrum	150
6.25	Crab light curve	151

6.26	Neutron star eclipse	152
6.27	X-ray burst of KS 1731–26	154

List of Tables

2.1	<i>IXO</i> science drivers	32
2.2	<i>IXO</i> instrument requirements	33
3.1	Intrinsic properties of semiconductor	45
4.1	Sequencer signals	84
4.2	Possible chopper wheel configurations	90
5.1	Hybrid 42 operation voltages	92

CHAPTER 1

Introduction

“The history of astronomy is a history of receding horizons.”

[Edwin Powell Hubble]

1.1 Origin of X-ray Astronomy

Throughout its history astronomy has always gained increasing knowledge from advancements in technology. From the first observations of the dark sky with the naked eye, over the first instruments to measure the culmination of stars and the invention of optical telescopes, to today’s sophisticated instrument sets, astronomy has come a long way. Through new generations of detectors, the increase in the sensitivity allows to observe fainter and fainter sources, or perhaps even opens up the possibility to study the Universe in a completely different “light”.

Compared to astronomy performed in the visible wavelength band, X-ray astronomy can be considered as a “young field”, but has already become an indispensable part of modern astrophysics. Since the Earth’s atmosphere is opaque for X-rays, ground based X-ray astronomy is not possible. For the first experiments balloons and rockets were therefore used, transporting the detectors to altitudes where observations could be performed. During a rocket flight in 1962, aimed to detect X-rays from the Moon, the first extra solar X-ray source, Scorpius X-1, was discovered by [Giacconi et al. \(1962\)](#). One of the major drawbacks of the rocket experiments was the limited observing time of only a few minutes. This limitation was overcome by the first X-ray satellite *Uhuru* which was launched in 1970 and discovered 339 X-ray sources during its operational time of more than two years. These sources are listed in the 4th *Uhuru* Catalog, which contains most of today’s well known X-ray objects ([Forman et al. 1978](#)).

The next major breakthrough came 1978 with the *Einstein* satellite (HEAO-2) (Giacconi et al. 1979), where for the first time grazing incident telescopes were used to image the X-ray sky. The arcsecond angular resolution of *Einstein* allowed to study extended objects and to resolve faint sources.

With *EXOSAT* the first X-ray observatory of the European Space Agency was launched in 1983 (White & Peacock 1988). *EXOSAT* discovered the first quasi-periodic oscillations in low mass X-ray binaries and X-ray pulsars and it featured one of the first on-board computers.

The first imaging X-ray survey was then performed by the German *ROSAT* mission (Pfeffermann et al. 1987). During the *ROSAT* operation from 1990 to 1999 more than 125 000 new X-ray sources were catalogued. A detailed review of X-ray telescopes from the beginning to the early 90's is given by Bradt et al. (1992). On the NASA High Energy Astrophysics Archive¹ a large database of high energy astronomy missions can be found, including projects led by other agencies.

In 1996 the Italian-Dutch mission *BeppoSAX* was launched. It carried the first broad band instrumentation covering the energy band of 0.1–300 keV (Boella et al. 1997). *BeppoSAX* provided the first positions of Gamma-Ray Bursts with arcminute precision and provided the first measurements that showed a connection between Supernova explosions and long Gamma-Ray Bursts.

In 1999, two major X-ray observatories were deployed into space and are still highly successfully operated today. With the NASA's *Chandra X-ray observatory* (Weisskopf et al. 2002) the mirror technology was pushed to new limits with the still yet unrivaled high angular resolution of less than one arcsecond allowing to resolve fine structures of X-ray sources. The ESA mission *XMM-Newton* (Jansen et al. 2001) has through its three mirror modules, each consisting of 58 nested mirror shells, a large effective area ($> 4500 \text{ cm}^2$ at 1 keV) which forms together with the focal plane instrumentation a powerful high throughput observatory.

In 2005, the *Suzaku* satellite was launched carrying the first X-ray micro-calorimeter into space (Mitsuda et al. 2007). With this superconducting detector, non-dispersing X-ray spectroscopy with an energy resolution of 7 eV at 6 keV, would have been possible. Unfortunately, after one month, a defect in the cooling system led to the loss of the liquid helium, rendering the micro-calorimeter inoperative. The mission is still a success, since the remaining two instruments work well within the specifications and allow measurements in the broad energy range of 0.2–700 keV.

In addition to the above mentioned satellites many more have been and are still being used during the last 40 years of X-ray astronomy, some of them were developed to fulfill highly specialized tasks, like *Rossi X-ray Timing Explorer*

¹<http://heasarc.gsfc.nasa.gov/docs/>

for all-sky monitoring and high time resolved observations, or like *Swift* to trace Gamma-Ray Bursts, a task that requires a fast slew ability.

1.2 Future prospects

Astronomy in general benefits from advancements in technology, but at the same time it is also the driver behind the development of new technologies. All fields within astronomy and astro-particle physics profit from the improvements made in the last decade, from the increasing computing power available, over efficient semiconductor sensors and superconducting detectors, to faster and less error-prone electronics. But building state-of-the-art instruments becomes more and more cost intensive. This is especially true when space based instruments are developed, where special effort is needed to ensure the proper functionality of all systems, since the repair of defect units is basically a non-existent option.

In astronomy, national and international cooperations on the European scale and beyond have been common for a long time. This will be even more the case for the future, where national funding agencies are forced to found alliances for the realization of cost intensive projects. On this background, the ASTRONET and the Astroparticle Physics European Coordination (ApPEC) committees were founded in order to assemble a strategic concept which recognizes possible synergies between the different fields of astronomy and develops a cost-effective way such that the most science can be realized with the available budgets.

In 2003, a memorandum was published by the [Deutsche Forschungsgemeinschaft \(2003\)](#), which was translated and updated in 2008, for the prospects of astronomy in Germany. For the field of astro-particle physics this was done by the [Komitee für Astroteilchenphysik \(2006\)](#). The recommendations of the European committees led to the [ApPEC \(2007\)](#) and the [ASTRONET \(2007\)](#) reports. Here the key questions, where major progress is expected in the next decade, are posed and the technology necessary to achieve this is identified. This long-term planning concept has already been successfully used by ESA with their Horizon 2000 and Horizon 2000+ programs. Parts of the current ESA's Cosmic Vision 2015–2025 program are therefore already included in the committee reports.

The identified key areas listed in the reports can be grouped around four main topics:

- *The Universe as a whole*
How did the Universe evolve during the early phases of the Big Bang? How did the large scale structures in the Universe form, and what is the role of the Dark Energy? What is the connection between the formation and evolution of galaxies and the supermassive black holes in their center?

- *Extremes in the Universe*

How can the most extreme places in the Universe (black holes, neutron stars, Gamma-Ray burst) be used to test our understanding of the most fundamental laws of physics, under conditions which are inaccessible in laboratories? Where are the accelerators and what are the processes that generate Cosmic Rays up to the yet highest detected energies? Furthermore, the detection of gravitational waves would open the possibility to observe completely different aspects of the Universe.

- *Stars and Planets*

Observe star forming regions to improve and test our knowledge of the stellar evolution. Trace the formation of planets within the circumstellar and proto-planetary disks. Investigate on the conditions necessary for the development of habitable planets.

- *The Solar System*

How does the Sun and the solar wind influence the environment in the Solar System? How did the Solar System form? What can we extrapolate from the current shape of the Solar System for the creation of life?

Many instruments ranging from ground based Cherenkov telescopes and Cosmic Ray detectors, over infrared observatories to probe the dust obscured regions of the Galaxy to the probes and landers for the exploration of the Solar System, are needed to make breakthrough discoveries in the above addressed topics. X-ray astronomy can be used in at least two out of the four key areas (*Extremes in the Universe* and *The Universe as a whole*) as a way to gain new insights. In the science cases of *Simbol-X* and *IXO* presented in Chapter 2, a more detailed account of possible observations is given.

1.3 Goals and outline of the thesis

One essential task during the design and definition phase of a mission is to obtain realistic values for the instrument performance needed to check whether the science requirements can be met. Therefore measurements in combination with simulations have to be performed. The goal of the thesis is to evaluate various aspects related to the timing and count rate performance of the semiconductor detectors which form the key instrumentation of two satellites planned within the framework discussed above. In the focus of this thesis lie detectors based on Depleted P-channel Field Effect Transistors (DePFET) and, to a certain extent on silicon drift detectors. For the performance evaluation, a simulation code was developed. This code was

validated with measurements on DePFET prototypes obtained with a test setup at IAAT. The building of the laboratory setup was an essential part of the work done for this thesis, necessary for the understanding of the devices and for the interactive optimization process of the simulations.

In Chapter 2 the two future satellite missions, *Simbol-X* and the *International X-ray Observatory (IXO)* are introduced. On these missions, a DePFET based X-ray detector is foreseen as main instrument. For both missions the scientific goals are outlined and the general satellite characteristics are described. A short account of the planned X-ray mirror assembly is given and their focal plane instrumentation is presented.

Chapter 3 is devoted to semiconductors and begins with a description of the essential interaction processes of radiation with matter. The pn-junction and the sideways depletion principle are explained to some extent, since they form the basic constituents of the silicon based detectors used at IAAT. Furthermore the ionization statistics of semiconductors and the operation of a MOSFET is introduced.

The DePFET detector and the laboratory setup needed for the operation of the device are in the focus of Chapter 4. The general operation principle of the DePFET together with the necessary front-end electronic and the data acquisition system is presented.

Basic measurements and the analysis of the obtained data are presented in Chapter 5. The difference between front- and back-illumination and the good achievable energy resolution of ~ 130 eV (at 6 keV) are shown. Results of the offset stability measurements are reported and the spectral analysis indicating that the special geometry of the used detector suffers from charge loss are discussed.

In Chapter 6, the phenomenon of pile-up in imaging detectors, which limits the possibility to observe bright sources is discussed. Thereafter, the simulation package and important parts of the code are explained. The simulation code is verified by measurements with respect to timing performance and spectral resolution. The ability of the code to model the charge splitting and the pile-up behavior of the detector used in the laboratory is shown. For the two satellite missions, *Simbol-X* and *IXO*, on which the DePFET detector is planned to be used as main instrument, performance simulations have been done to estimate the observation limits for bright X-ray sources. Areas where the code and the used detector response need improvements are addressed and possible solutions are investigated. The presentation of astrophysical simulation results for the Crab, a neutron star eclipse, and an X-ray burst mark the end of the chapter.

This thesis is then closed by a summary of the obtained results and an outlook to the future prospects for *Simbol-X* and *IXO* is given in Chapter 7.

CHAPTER 2

Future missions

“The Universe: a device contrived for the perpetual astonishment of astronomers.”

[Arthur C. Clarke]

In this Chapter, two X-ray satellite missions are introduced, the *International X-ray Observatory (IXO)* and the *Simbol-X* mission. In Section 2.1.1 a selection of three main scientific fields are presented which will be addressed by the *International X-ray Observatory*. Section 2.1.2 outlines the general mission design and the orbit of *IXO*, followed in Section 2.1.3 by a description of necessary developments in the mirror production technology. In Section 2.1.4 with introduction of the different focal plane instruments the main part of this chapter is concluded. Section 2.2 is dedicated to *Simbol-X* and begins with a short description of scientific objectives, followed by a brief outline of the detectors planned for this challenging mission.

2.1 The International X-ray Observatory

The *International X-ray Observatory (IXO)* is currently studied as the next large aperture X-ray mission of ESA, NASA, and JAXA. The *IXO* study began officially in Summer 2008. Its origins can be traced back to NASA’s *Constellation-X* (Bookbinder et al. 2008) and ESA’s *X-ray Evolving Universe Spectrometer (XEUS)* missions (Turner & Hasinger 2007). The *XEUS* mission was selected as one of three L-class missions to be studied by ESA in the context of the Cosmic Vision program. It eventually turned out that *XEUS* would not be feasible with the given budget, therefore ESA / JAXA / NASA decided to conduct a joint study, the *International X-ray Observatory*. Most of the material presented in this chapter is based on the *XEUS* proposal (Turner & Hasinger 2007), the *IXO* payload definition

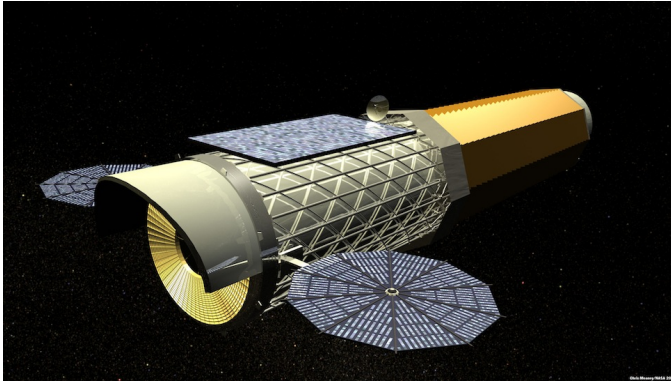


Figure 2.1: Artistic view of *IXO*, showing the large aperture optics in the front, the solar panels (to the left, right, and on top), as well as the extendable optical bench towards the back (NASA <http://ixo.gsfc.nasa.gov>).

document ([IXO-IWG 2009](#)), and papers submitted to the U.S. Astronomy 2010 decadal process.

In this early planning phase of *IXO*, the launch is scheduled for 2021. The requirements and the technical implementation of the instruments are certainly subject to changes as the mission evolves. The configuration presented here is therefore just a snapshot of the payload definition at the time of writing. An artistic view of the preliminary *IXO* design can be seen in Fig. 2.1.

2.1.1 Scientific Objectives

The scientific objectives of *IXO* can be summarized as the observation of the “hot” Universe in X-rays, where the evolution of small and large scale structures will be traced with yet unprecedented timing, spectroscopy and imaging capabilities. The science perspectives of *IXO* can roughly be grouped in 3 categories, enclosing a vast discovery space.

Evolution of large scale structures

With its high spectral and imaging capabilities, *IXO* can observe supermassive black holes (SMBH) which are believed to reside in the center of every galaxy and study the interaction between the host galaxy and the SMBH. The energy liberated by matter falling onto a black hole creates outflows in the form of radiation and jets, which influence the infall of gas in the region around the black hole. This feedback mechanism of the SMBHs eventually determines the shape and the mass

of the galaxy and fixes in addition, through a yet unknown process, the growth of the SMBH mass to a fraction of the galaxy bulge mass (Fabian et al. 2009). With the large collection area, *IXO* can trace the growth of galaxies at redshifts up to $z = 1-3$, where most of the mass accretion is believed to take place. With today's instruments, the study of the evolution of galaxy clusters is limited to $z \approx 0.5$, where the clusters have already been formed. *IXO* will allow observations up to redshifts of $z = 2$, where the growth of the low-mass cluster into today's massive clusters can be traced (Arnaud et al. 2009). Abundance measurements will allow to study the influence of SMBH feedback on the evolution of clusters of galaxies. Observations which measure the mass and space density of galaxy clusters against redshift, allow to put constraints on the equation of state of the dark energy.

High resolution gratings ($R \approx 3000$) in combination with the large effective area will allow *IXO* to measure the "cosmic web" in which more than half of the baryons in the local universe are believed to exist in form of hot diluted gaseous filaments. By measuring the absorption lines of ionized chemical elements along the line of sights to background AGNs, the baryons can be detected and their distribution can be mapped (Bregman et al. 2009). Figure 2.2 shows a compilation of expected results for sources with a redshift > 1 obtained from a simulated 1 Msec observation.

Life cycles of matter and energy

The heavy elements are produced inside stars and then dispersed through Supernova explosions. With *IXO* it will be possible to measure the gas velocities inside starburst galaxies and thus determine the effects of galactic winds on the metal enrichment of the IGM. Furthermore, the metal abundances within our Galaxy can be mapped through absorption line measurements of the interstellar medium (Bookbinder 2009). With the high spectral and spatial resolution of *IXO* it will also be possible to measure Doppler shifts and line widths in Supernova remnants (SNRs). This will allow to obtain information about the geometry of the explosion, from which conclusions about the underlying mechanism can be drawn and simulations of Supernova explosions can be tested.

Young Supernova remnants are believed to be the acceleration sites of Cosmic Rays for energies up to 10^{15} eV. In SNRs synchrotron radiation is produced by electrons in the shock front. The *IXO* energy range up to 40 keV allows the determination of the energy cut-off of the synchrotron radiation, which is linked to the maximum energy of the electrons in the shock. From these measurements, hints to the limiting process of Cosmic Ray acceleration in SNRs could be found (Fiore et al. 2008).

Matter under extreme conditions

Neutron stars and black holes are among the most extreme places that can be

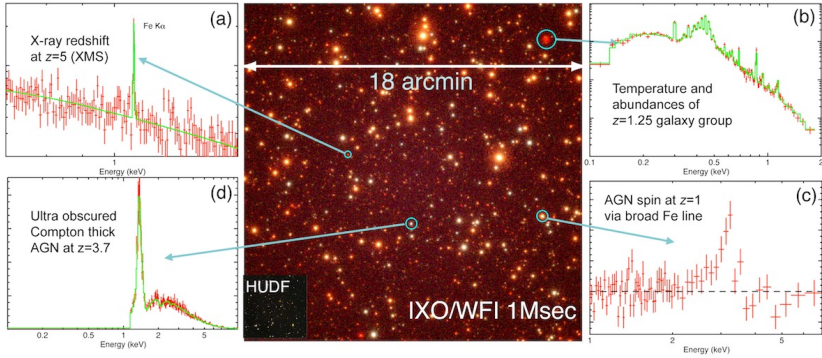


Figure 2.2: Simulated image of a 1 Msec *IXO* WFI observation, based on the *Chandra* Deep Field South. To illustrate the capabilities of *IXO*, four different simulated spectra are shown: a) highly resolved spectra allow to determine the redshift in X-rays; b) measurement of a galaxy group at $z = 1.25$ from which the temperatures and abundances can be determined; c) spin determination of an AGN at $z = 1$ from the iron line shape; d) measurement of Compton thick AGNs at high redshifts. The inset shows the field of view of the *Hubble* Ultra Deep Field (Bookbinder 2009).

found in the Universe. In neutron stars, magnetic fields can exceed 10^{12} Gauss¹ and the density in the core surpasses even the density of atomic nuclei, creating an environment that cannot be reproduced in the laboratory. Through fast timing measurements of, e.g., matter orbiting close to the compact object or timing analysis of X-ray bursts, the mass-radius relation of neutron stars can be determined, thus allowing to infer on the equation of state of these objects (Miller et al. 2009; Paerels et al. 2009).

Through observations of Galactic black holes and the central SMBHs in AGNs, General Relativity can be tested in the strong field limit. Around accreting rotating black holes where effects like gravitational light bending and frame dragging occur, the emitted radiation can only be measured in the X-ray range. The area close to black holes can be probed by, e.g., measurements of the relativistically broadened iron line which originates in the illuminated accretion disk and which is distorted by the gravitational field (gravitational redshift) and by the orbital motion around the black hole (Doppler shift, beaming) (Brenneman et al. 2009; Tomsick et al. 2009).

IXO will also allow to study the population of supermassive black holes at redshifts up to $z = 7-10$. The study of the SMBH growth is essential to explain

¹In magnetars even 10^{15} Gauss are possible

the presence of SMBHs with large masses of $M_{\odot} = 10^9$ at $z = 6$ (Nandra 2009). Different evolution models (growth through accretion and/or mergers) predict different spin distributions of the SMBHs, which can be tested by measuring the spin for a sample of AGNs. To detect and resolve these AGNs, a large field of view in combination with a large effective area and a good angular resolution is needed (Bookbinder 2009).

2.1.2 Mission Design

To fulfill the scientific goals, *IXO* needs a large collecting area (3 m^2 at 1 keV), which is a more than 20 times larger effective area than that of any current X-ray observatory, in combination with an energy range of 0.1–40 keV. To focus the X-ray photons on the focal plane, Wolter Type I mirrors are used (Wolter 1952). The Wolter X-ray telescope design is based on the grazing incidence and utilizes the effect of total reflection at the interface between an optically thick and an optically thin medium. The critical angle for total reflection has an energy dependence that scales with $\theta_c \sim 1/E$, this means that to focus X-rays with higher energies a larger focal length is required, i.e., 20–25 m for *IXO*. In order to avoid source confusion and to resolve the faint AGNs at high redshifts, an angular resolution of $5''$ HPD² is needed. A detailed account of the techniques and principles used for X-ray optics is given by, e.g., Aschenbach (1985) and Friedrich (2008).

Due to its considerable focal length of 20 m, *IXO* cannot be integrated in the rocket fairing in its final geometry and uses therefore an extendable optical bench to bring the optics in the flight mirror assembly and the focal plane in the correct distance. The mission will be designed for 5 years operation, but should hold consumables for at least 10 years.

The orbit of *IXO* will be at the Lagrangian point L2, one of the five liberation points in the Sun-Earth system. Here, a small body can be placed into a stationary orbit within the rotating Sun-Earth reference frame. At a distance of 1.5 million km from the Earth, the L2 exists in the direct prolongation of the line Sun-Earth, where the gravitational force of both objects is matched by the centrifugal force. This leads to a saddle point in the effective potential in which a satellite can be placed, revolving with the Earth around the Sun. Since this is an unstable equilibrium, the satellites cannot be placed directly at the L2, but need to follow a closed trajectory (halo or Lissajous orbit) in the vicinity of the L2. The Wilkinson Microwave Anisotropy Probe (WMAP) was the first satellite entering a Lissajous orbit in the L2 in 2001, the most recent ones were the ESA Missions *Herschel* and *Planck* in 2009. The main advantage of L2 is a stable radiation background and thermal

²Half-power diameter, the diameter in which half of the energy of the point spread function (PSF) is encircled.

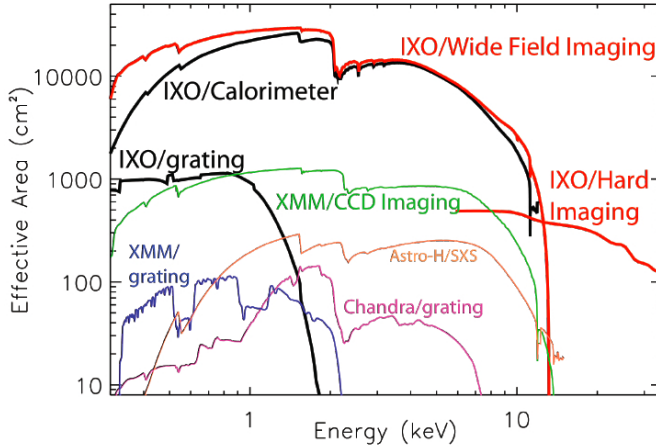


Figure 2.3: Effective areas of the different *IXO* instruments compared to the corresponding *XMM-Newton* and *Chandra* values (NASA <http://ixo.gsfc.nasa.gov>).

environment since the Sun and Earth are always in the same direction. These properties simplify the thermal and optical shielding of the satellite and offer good passive cooling capabilities. The rotation of the Earth around the Sun allows the observation of the complete sky during the duration of a year, eliminating the necessity to observe objects close to the Sun.

2.1.3 Optics

The X-ray mirrors are considered to be the main technological breakthrough of *IXO*. For the large effective areas of 3 m^2 at 1 keV, 0.65 m^2 at 6 keV, and 150 cm^2 at 30 keV (see Fig. 2.3) in combination with the $5''$ HPD angular resolution, new light weight optics have to be developed, since with currently used technology the mirror mass would exceed the lifting capabilities of the launcher. For *Chandra*'s $0''.5$ HPD Zerodur mirrors the weight is 18500 kg per m^2 of effective area at 1 keV. For the $14''$ HPD mirrors of *XMM-Newton*, produced with the nickel replication technique, the weight is 2300 kg per m^2 (Bavdaz et al. 2004).

Two different approaches are currently investigated for the production of the *IXO* mirrors, “slumped” glass and silicon pore optics, each with a weight of $200\text{--}300 \text{ kg per m}^2$. The challenge lies in the production of the segmented optics with the required angular resolution of $5''$ HPD.

For the slumped glass optics, mirror segments are produced by thermally deforming (slumping) 0.4 mm thick sheets of glass which is placed on a mandrel

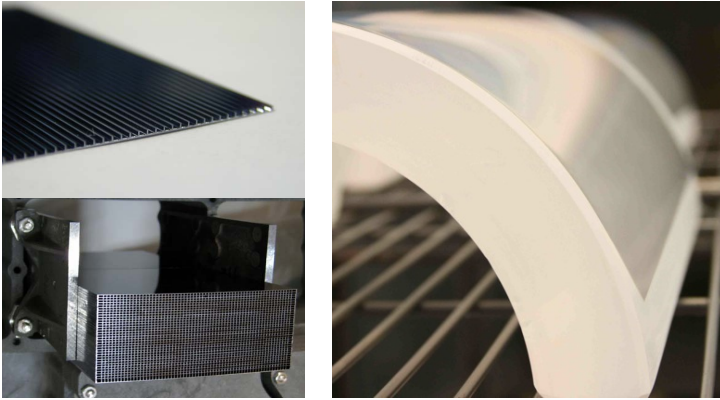


Figure 2.4: Left: One single plate of the silicon pore optics with the etched rib structure. Below, a module consisting of 35 stacked layers can be seen (ESA <http://www.esa.int>). Right: Production of a slumped glass sheet with the shape-giving mandrel (NASA <http://ixo.gsfc.nasa.gov>).

with the intended shape. A 15'' HPD has already been measured with prototypes of slumped glass optics (Zhang et al. 2008b). For the silicon pore optics, ribs are etched in silicon wafers on one side while the other side is coated with a reflective layer. The etched plates are then stacked on top of each other, resulting in a comb structure (see Fig. 2.4). A 4'' HPD has been reported from pencil beam tests (Collon et al. 2006), full illumination measurements of larger stacks resulted in 15'' HPD caused by particle contamination during the stacking process (Collon et al. 2008). Both technologies look promising but require substantial improvements in terms of angular resolution to meet the *IXO* requirements. To enhance the high energy response of the mirrors, the shells in the center of the telescopes can be realized with a multilayer coating of alternating layers of materials with low and high atomic number Z , e.g., carbon and platinum, increasing the X-ray reflectivity (Pareschi et al. 2008).

2.1.4 Focal Plane

A baseline set of five different instruments is the subject of detailed studies performed in Europe and the US until mid-2010, to ensure that the scientific requirements of *IXO* can be met. The following description is based on data published by the instrument working group (IXO-IWG 2009).

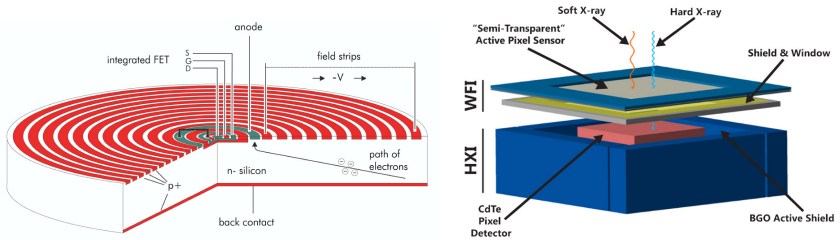


Figure 2.5: Left: Silicon drift detector, with the central amplifier and the drift-rings. The HTRS will consist of 37 SDD cells (Lutz et al. 2007b). Right: The stacked WFI and HXI, together with the anti-coincidence drawn in blue (NASA <http://ixo.gsfc.nasa.gov>).

- *Wide Field Imager (WFI)*

The silicon based Wide Field Imager is an imaging X-ray spectrometer based on the active pixel sensor concept and will operate in the energy range from 0.1–15 keV. In an active pixel sensor, each pixel has its own amplifying circuit, in this case realized as Depleted P-channel Field Effect Transistor (DePFET). Details of the DePFET will be discussed in Chapter 4. The WFI will have 1024×1024 pixel and cover a field of view of $18' \times 18'$, with a nearly Fano limited energy resolution of 130 eV at 6 keV and a frame time of ~ 2 ms (Lechner et al. 2006; Stefanescu et al. 2009).

- *Hard X-ray Imager (HXI)*

The Hard X-ray Imager will be based on the *Astro-H* HXI (Kokubun et al. 2008) and use the high mass absorption coefficient of CdTe to detect X-rays in the 10–40 keV band. The detector is realized as Double-sided Strip Cadmium-Telluride Detector with a thickness of 0.5 mm and a quantum efficiency close to 100% up to 40 keV. On top of the CdTe detector a Double-sided Silicon Strip Detector is mounted which is used together with the active anti-coincidence shield surrounding the HXI to suppress the particle background and which can in addition be used as X-ray detector in the energy band from 10–30 keV. The HXI will be located directly underneath the WFI and therefore both detectors count as one instrument (see Fig. 2.5).

- *X-ray Microcalorimeter Spectrometer (XMS)*

The X-ray Microcalorimeter Spectrometer is a non-dispersive imaging spectrometer with an energy resolution of 2.5 eV between 0.3 and 7 keV. The XMS is realized as transition edge sensor (TES) in which a superconducting sensor is operated at a temperature close to the normal conducting phase.

The photon interaction in the detector leads to phonon vibrations which cause a rise in the resistivity through the transition from the super-conducting to the normal conducting phase. The XMS consists of a central (core) region of 40×40 pixel covering a field of view of $2' \times 2'$. The core is surrounded by an array of 52×52 pixel of larger size with an energy resolution of 10 eV covering a field of view of $5' \times 5'$ (Kilbourne et al. 2008).

- *High Time Resolution Spectrometer (HTRS)*

The High Time Resolution Spectrometer is an array of silicon drift detectors with an integrated FET in the center as first amplifier stage of the pixel (Fig. 2.5). The HTRS has 37 hexagonal pixels with a 4 mm diameter. In order to measure count rates up to 10^6 cts s^{-1} , the detector is placed out-of-focus to distribute the incoming photons over all pixels. Details of the HTRS are given by Barret et al. (2008).

- *X-ray Grating Spectrometer (XGS)*

The X-ray Grating Spectrometer is a dispersive spectrometer with a resolving power of $E/\Delta E = 3000$ in the energy range from 0.3–1 keV. The gratings will be mounted behind the optics and disperse the X-ray photons on a CCD array (Fig. 2.6). McEntaffer et al. (2008) and Heilmann et al. (2008) give details of possible grating types.

- *X-ray Polarimeter (XPOL)*

The X-ray Polarimeter is designed to measure the energy, the position, and the polarization of an incoming photon. It uses a gas detector in which the photoelectron created by the X-ray interaction produces a track of ionized gas particles that can be measured. From the track, information about the direction of the primary photoelectron and from the distribution of the tracks the polarization of the X-ray photons can be determined (Costa et al. 2008; Bellazzini et al. 2006).

The instruments are mounted on a moveable platform and only one instrument can be operated at a time in the focal plane, with the exception of the XGS which is always on. The design of the gratings (transmission or reflection) and their position in the optical path is still an open issue. In Table 2.1, the key performance requirements and the related science topics are summarized. In Table 2.2, the main instrument parameters for the WFI/HXI and HTRS are listed since they form the core of the performance simulations shown in Chapter 6. For comparison reasons, the XMS parameters are additionally listed.

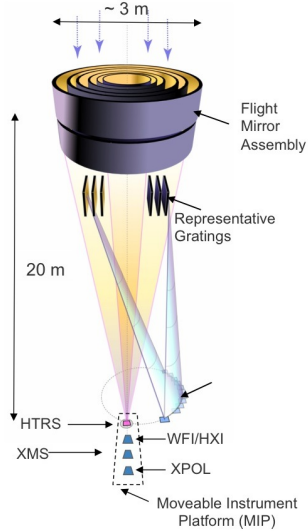


Figure 2.6: Outline of the *IXO* flight mirror assembly and the relative positions of the instruments. The gratings are located behind the mirrors and the corresponding CCDs are mounted off-axis (Bookbinder 2009).

Table 2.1: Key performance drivers of the *IXO* instrumentation. The data is compiled from the NASA website <http://ixo.gsfc.nasa.gov> and Bookbinder (2009).

Parameter	Value	Band	Science	Instrument
Effective Mirror Area	3 m^2	@ 1.25 keV	BH Evol., LSS [†]	
	0.65 m^2 (1 goal)	@ 6 keV	Strong Grav., EOS [‡]	
	150 cm^2 (350 goal)	@ 30 keV	Strong Grav.	
Spectral Resol.	$\Delta E = 2.5 \text{ eV}$ (2')	0.3–7 keV	Cluster Evol.	XMS
FWHM (FoV)	$\Delta E = 10 \text{ eV}$ (5')	0.3–10 keV	Cosmic Feedback	XMS
	$\Delta E = 150 \text{ eV}$ (18')	0.1–15 keV	BH Evol.	WFI/HXI
Angular Resol.	$E/\Delta E = 3000$ (ps [§])	0.3–1 keV	Cosmic Web	XGS
	5'' HPD	0.3–7 keV	Cosmic Feedback	XMS
	5'' HPD	0.1–15 keV	BH Evol.	WFI/HXI
Count Rate [cps]	30'' HPD (5'' goal)	7–40 keV	Strong Grav.	WFI/HXI
	equiv. 1 Crab		EOS	HTRS
	<10% dead time			

[†]Large Scale Structure

[‡]Equation of State

[§]Point Source

Table 2.2: IXO instrument requirements. Data are compiled from the XEUS proposal to ESAs Cosmic Vision 2015–2025 call (Turner & Hasinger 2007) and from the IXO Payload Definition document (IXO-IWG 2009).

Instrument	WFI	HXI	XMS	HTRS
Detector type	Active pixel sensor	CdTe + Si strip	TES	Silicon drift detector
Size [mm]	102.4 × 102.4	70 × 70	31.2 × 31.2	∅ 16.1 (hexagonal)
Pixel size [μm]	100 × 100	220 × 220	300 × 300; 600 × 600	∅ 4000
Pixel number in one dim.	1024	320 CdTe Strips	40 (+32)	37 (total)
Field of view [arcmin ²]	17.6	12	2 (5.4)	2.8
Energy range [keV]	0.1–15	10–40	0.3–10	0.3–20
Energy resolution FWHM	50 eV @ 0.3 keV 125 eV @ 6 keV	1 keV @ 40 keV	2.5 eV @ 6 keV	200 eV @ 6 keV
Est. background: [cts cm ⁻² s ⁻¹ keV ⁻¹]	5 · 10 ⁻³	5 · 10 ⁻⁴	5 · 10 ⁻³	Not relevant
Count rate capability [†] : cts pixel ⁻¹ s ⁻¹	100	20 000	75; 25	>100 000
cts source ⁻¹ s ⁻¹	6000	20 000	1500; 200	>2 000 000
Timing accuracy [μs]	Full frame 1000 Partial frame 16	10	10	10
Operating temperature [K]	210	233	50 · 10 ⁻³	253

[†] 10% pile-up and 5'' HPD

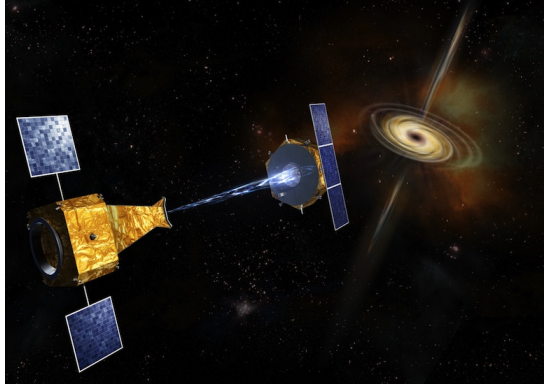


Figure 2.7: Artistic view of the *Simbol-X* satellites. On the left side the detector and in the center the mirror spacecraft are shown. The blue beam highlights the X-ray photon path along the optical axis (© CNES 2006).

2.2 *Simbol-X*

Simbol-X is a planned French-Italian satellite mission with German contribution to the focal plane instrumentation, whose launch is estimated to be around 2015. In this thesis, performance simulations of the Low Energy Detector (LED) have been undertaken to compare the capabilities of *Simbol-X* and *IXO* to observe bright Galactic sources. The simulation results are presented in Section 6.4, since they illustrate the complementing capabilities that *Simbol-X* would have with respect to *IXO*. Here only a very brief introduction to the *Simbol-X* mission will be given, focusing on the most essential aspects. A more detailed description is presented by, e.g., Ferrando et al. (2006, 2009) and Tenzer (2008). In March 2009 the mission was surprisingly suspended by the French Space Agency (CNES) due to budget reasons, shortly before the start of the industrial “phase B”.

2.2.1 Overview

In currently operating X-ray satellites the usage of X-ray focusing optics is limited to energies below 10–15 keV, mainly by the available focal length which limits the effective area of the mirror assembly at higher energies. For higher X-ray energies, coded masks and collimators are used to obtain spatial information of the sources like, e.g., on *INTEGRAL* (Winkler et al. 2003). To build a satellite with focusing optics in the energy range between 0.5–80 keV would mean to step from arcminute to arcsecond angular resolution and to increase the sensitivity by 2–3 orders of magnitude (Fiore et al. 2009).

The focal length of *Simbol-X* is 20 m, but instead of an extendable optical bench between the optics and the focal plane as for *IXO*, two independent satellites in formation flight configuration are foreseen. The mirror spacecraft (MSC) would be in its natural orbit, while the detector spacecraft (DSC) would be trailing behind on a non-Keplerian orbit. A high elliptical orbit is chosen for the formation flight, resulting in ~ 300 ks uninterrupted observation time outside the radiation belts (Ferrando et al. 2009).

The hard X-ray mirrors are planned to be produced in the nickel-reproduction technique, based on the heritage of *XMM-Newton*, and include a platinum/carbon multilayer to enhance their high energy response (Pareschi et al. 2008). For test mirror shells, an angular resolution of $18''$ HPD at 10 keV, and $25''$ HPD at 30 keV has been reported by Tagliaferri et al. (2009)³. These values are already close to the required $20''$ HPD angular resolution.

2.2.2 Scientific Objectives

One of the major science goals of *Simbol-X* is to resolve more than 50% of the Cosmic X-ray Background (CXB) above 10 keV. Below 10 keV, the CXB has been resolved into individual sources, mainly low luminosity AGNs. In the energy band around 30 keV where the CXB peaks, it is expected to consist of highly obscured, Compton-thick AGNs which could not be resolved with the current X-ray satellites (Gilli et al. 2007). Through these studies, evolution models of SMBHs can be tested and our knowledge about jets and accretion can be deepened. Furthermore, *Simbol-X* would be able to observe the dynamics of matter accreted onto a compact object with the advantage of a broad energy range, measuring the transition from thermal to non-thermal spectra. In addition, nucleosynthesis studies of young SNRs through the mapping of the ^{44}Ti line and the study of particle acceleration mechanisms is possible (Fiore et al. 2008, 2009).

2.2.3 Focal Plane

The focal plane consists of a silicon-based Low Energy Detector (LED), a CdTe-based High Energy Detector (HED), and an active anti-coincidence shield for background suppression. The LED and the HED are used in a stacked geometry such that high energy X-rays which could not be stopped in the LED will be detected with the HED located below (Laurent et al. 2008).

The Low Energy Detector, covering the energy range of 0.5–20 keV, is an active pixel sensor realized as a matrix of 128×128 DePFETs. Around the central DePFET, a series of concentric rings are implemented in order to drive the charge

³The origin of the HPD increase with energy is currently investigated and is supposed to be caused by the micro-roughness of the mirror surface which leads to diffuse X-ray scattering.

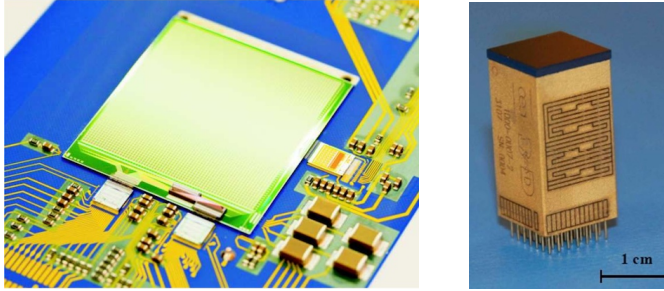


Figure 2.8: Left: The Low Energy Detector in a laboratory configuration with 64×64 pixel. On the left side the two SWITCHER chips, essential for the readout, and on the right side the front-end amplifier chip can be seen (Treis et al. 2009). Right: High Energy Detector prototype of a 64 pixel CALISTE module. The dark color on the top is the CdTe semiconductor detector, the golden block below is readout electronics (source: CEA; <http://irfu.cea.fr>).

generated in the fully depleted detector bulk towards the central readout node, similar to the case of the HTRS. The pixels would have a size of $625 \times 625 \mu\text{m}^2$, designed to match the $20''$ HPD of the mirrors. Laboratory devices have already been successfully tested and have shown an energy resolution of less than 130 eV FWHM at 6 keV (Lechner et al. 2008). A detailed description of the LED is given in Chapter 4. The planned frame time of $128 \mu\text{s}$ results in ~ 8000 frames per second. At the Institut für Astronomie und Astrophysik of the University of Tübingen, an onboard data processing electronics is being developed in order to filter scientifically relevant events from the raw data stream, and hence reduce the bandwidth the satellite bus system needs to handle (Schanz et al. 2009).

The Hard Energy Detector will be made of 2 mm thick CdTe or CdZnTe semiconductor material, covering the energy band of 8–80 keV with a high quantum efficiency ($>97\%$ at 80 keV). The detector, with 128×128 pixel of $625 \times 625 \mu\text{m}^2$ size is designed to match the dimensions of the LED. The HED will be segmented in 64 individual modules with 1 cm^2 size, called CALISTE. On the modules, the readout electrodes are realized such that a structure of 16×16 pixel is created. The current prototypes feature 8×8 pixel with dedicated readout channels, the corresponding electronics is located directly below the CdTe crystal (see Fig. 2.8). The readout of the detector is triggered if the output signal of at least one pixel exceeds the lower threshold. In case of triggering all pixels of the module are read out, in order to detected events where charge splitting between individual pixels occurred. For the 64 pixels CALISTE prototypes, Meuris et al. (2009) reported energy resolutions (FWHM) of 0.74 keV at 14 keV and 0.91 keV at 60 keV.

Semiconductor Detectors

“Any sufficiently advanced technology is indistinguishable from magic.”

[Arthur C. Clarke]

3.1 Introduction

Semiconductor detectors are the working horses of current and next generation X-ray satellites. Various types of CCDs are widely used, e.g., ACIS¹ on-board of *Chandra* (Weisskopf et al. 2002), the two different focal instruments on *XMM-Newton* (EPIC²-MOS, Turner et al. 2001, and EPIC-pn, Strüder et al. 2001), XRT³ on-board of *Swift* (Wells et al. 2004), and the XIS⁴ on-board of *Suzaku* (Koyama et al. 2007). On *Spectrum-RG*, eRosita will use frame-store CCDs, an improved version of the pn-CCD of *XMM-Newton* (Predehl et al. 2006). A new detector type, the DePFET, is planned to fly on-board the *BepiColombo* Mission to Mercury (Strüder & Moser 2007), and possibly on-board IXO as WFI (Turner & Hasinger 2007). It was also designated as LED on the called off *Simbol-X* mission (Ferrando et al. 2006).

The advantages offered by semiconductor based detectors over others used for X-rays detection are manifold. As the emphasis of this thesis lies on DePFET detectors, the focus is shifted towards silicon based semiconductor detector systems:

- Upon the detection of a photon or particle, signal carriers are produced. To generate a free electron as signal carrier on average only 3 eV are needed in

¹Advanced CCD Imaging Spectrometer

²European Imaging Camera

³X-ray Telescope

⁴X-ray Imaging Spectrometer

a semiconductor. This energy has to be compared to the 30 eV for gas-filled detectors like proportional counters, which is one order of magnitude larger. Therefore a larger number of charge carriers is produced, thus increasing the signal-to-noise ratio. Furthermore statistical fluctuations make up a relatively smaller fraction of the signal, as the number of charge carriers per detected event is increased.

- As semiconductors are solids, they have a high density, thus a higher absorption coefficient, leading to a larger stopping power than that of gas based detectors, allowing therefore the production of thin and lightweight, yet solid detectors.
- The charge collection time for a typical semiconductor detector is of the order of nanoseconds, due to the mobility of the charge carriers (see Table 3.1 for values). This high mobility opens up the usage in high count-rate environments, e.g., in collider experiments such as the Large Hadron Collider (LHC), where the readout speed is mostly only limited by the electronics.
- Through the usage of compound semiconductors (e.g., GaAs, CdZnTe), properties such as the energy range, energy resolution, and radiation hardness of the detector can be tailored in broad regions to match the desired application (Owens & Peacock 2004).
- Development of low-noise detectors is facilitated since the readout and amplification electronics can be located very close to or even on the detector itself.

More detailed overviews of the benefits of semiconductor detectors can be found in Lutz (1999), Knoll (2000), and Spieler (2006). A review of recent advancements of silicon based detector development is presented by Strüder & Meidinger (2008).

In this chapter the basic principles which are essential for the understanding of the later presented DePFET detectors will be explained. Section 3.1.1 builds up the basic theory of the interaction mechanisms of photons with matter. In Section 3.2 important properties of semiconductors are outlined, with a focus on implications for their usage as detector modules. The operation principle of a pn-junction will be elucidated and the charge collection process will be introduced. Then a short summary of the ionization statistics of semiconductors is presented. After that the principle of sideways depletion will be laid out, as it is needed in the description of the recent detector developments. The chapter ends with a description of transistor operation which is exemplified by the MOSFET in Section 3.3, since it is one of the basic constituents of a DePFET pixel.

3.1.1 Interaction of photons with matter

Before entering the deeper realms of semiconductors, a short review of photon-matter interaction is necessary. A photon can interact with matter mainly through three processes, *photoelectric effect*, *Compton scattering*, and *pair creation*. Which of these is the dominating effect depends on the energy of the impinging photon and the atomic number Z , as shown in Fig. 3.1. For silicon, Fig. 3.2 shows the proportion of each process to the total absorption coefficient. All three cases have in common that the photon is scattered or absorbed in a single event and the energy and momentum of the photon are, completely or partially, redistributed to the electrons of the material (Knoll 2000). Therefore the energy of one photon in a beam of photons is unchanged with penetration depth, only the intensity is attenuated. The *Beer-Lambert law* describes the degradation of the intensity I after traversing a length x of material,

$$I(x) = I_0 \cdot e^{-\mu x} \quad (3.1)$$

where I_0 is the incident intensity and where μ is the energy and material dependent absorption coefficient. The absorption coefficient μ is directly related to the sum of the individual cross sections of the three processes and to the density and molecular weight of the material (tabulated in, e.g., Thompson et al. 2001). This exponential absorption stands in contrast to charged particle interaction, whose energy deposition involves several elastic collisions, losing energy along the track, and can be described by the Bethe-Bloch formula (see Leo 1993). X-rays and gamma rays are more penetrating than charged particles, due to the smaller cross sections for photon interaction with respect to particle interaction in matter.

Photoelectric absorption

Below 50 keV, photoelectric absorption is the main interaction channel of photons with matter. In this reaction the photon is completely absorbed in the interaction with a bound electron of an atom. The kinetic energy E that is carried away by the ejected electron is

$$E = E_i - U_b \quad (3.2)$$

where E_i is the initial photon energy and U_b the binding energy of the electron.

Photoelectric absorption can only take place in a bound-free interaction, since the atomic nucleus is needed to compensate for the recoil in momentum conservation (a free electron is not able to conserve momentum in the absorption process of a photon). The vacancy in the shell can then be filled either by absorption of a free electron from the medium or by an electron from an outer shell. A fluorescence photon can be emitted in both cases, in the first case the photon energy is determined by the difference between the kinetic energy of the electron and the binding energy

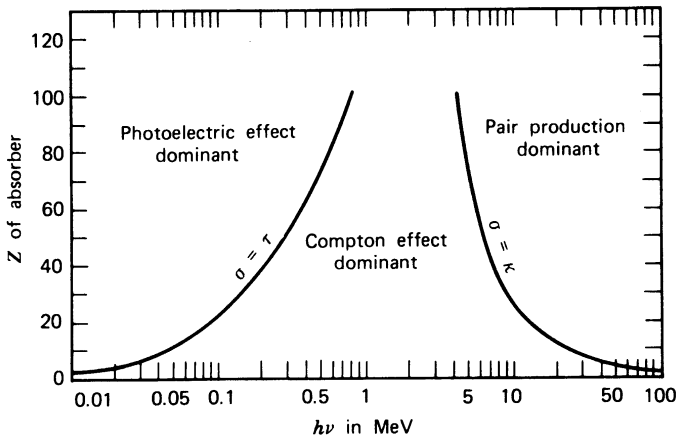


Figure 3.1: Regions of different photon interaction processes with matter. The lines indicate where for a given energy $h\nu$ and atomic number Z neighboring effects are equal. The linear attenuation coefficients of these reactions are denoted with τ , σ and κ (Evans 1955).

of the empty shell, in the latter one the characteristic wavelength of the photon depends on the energy difference between the initial and final shell. Instead of a fluorescence photon an Auger electron can be emitted. This happens when the vacant state is filled by an electron from an outer shell and the energy released in the transition is coupled to another outer shell electron, leaving behind an atom with 2 vacant states.

For photon energies above the K-shell energy of an atom, where the electrons have the highest binding energy, the cross section is very small. For lower photon energy the cross section rises, but shows steep drops at certain energies called *absorption edges* (see Fig. 3.2). They arise from the fact, that if the energy of the photon is less than what is needed to excite the electrons in a certain shell, this shell is not available for interaction anymore, thus the cross section for interaction with this atom is sharply reduced at this energy (Knoll 2000).

The fluorescence photon has a lower energy than the incident photon and thus a larger mean free path due to the drop in the cross section close to the absorption edge. If the detector or absorbing material is thin or absorption has occurred close to surface, the fluorescence photon may leave the material, carrying away energy which is missing in the reconstruction of the initial photon energy. A so called escape peak can then be detected in the spectrum.

For one atom the probability of photoelectric absorption σ , away from the

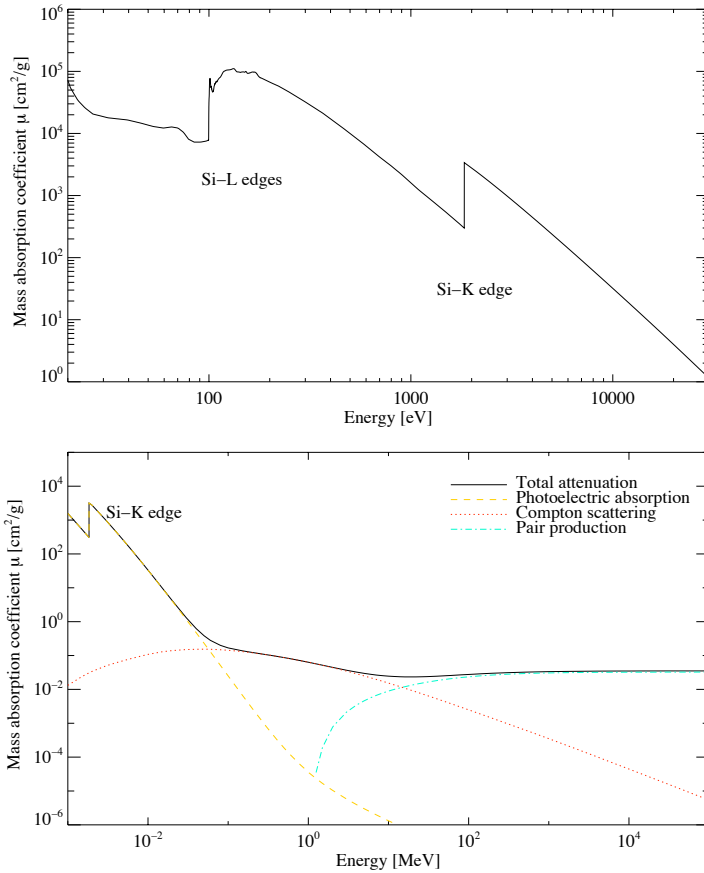


Figure 3.2: Mass absorption coefficient μ of silicon. Upper panel: photoelectric absorption between 10 eV–30 keV, drawn with data from [Henke et al. \(1993\)](#). Lower panel: total absorption coefficient between 1 keV– 10^5 MeV (Data: <http://physics.nist.gov>).

absorption edges, can be approximated by

$$\sigma = \text{constant} \cdot \frac{Z^n}{E_\gamma^{3.5}} \quad (3.3)$$

where Z is the atomic number of the absorbing material and E_γ is the incident photon energy ([Knoll 2000](#); [Leo 1993](#)). The exponent n of the atomic number Z varies between ~ 4 – 5 . Therefore when a detector for gamma-rays is designed a

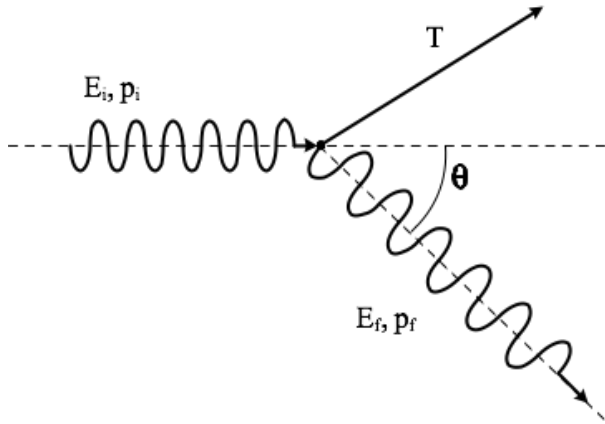


Figure 3.3: Compton scattering, E_i, p_i denotes the incoming, E_f, p_f the outgoing photon energy and momentum, T is the kinetic energy of the electron.

material with a high atomic number Z is preferred, as the interaction probability is strongly increased. The equation on the other hand shows, that energy dependence of the photoelectric absorption with $\propto E^{-3.5}$ leads to a higher interaction depth for X-rays in contrast to photons of visible light.

Compton effect

In the classical case of Compton scattering the incoming photon is assumed to interact with a stationary free electron. In the region between 60 keV and 10 MeV, where Compton scattering is the dominant effect, the binding energies of the electrons are small with respect to the X-ray photon energy and hence negligible. The photon energies before and after the scattering process are connected by

$$E_f = \frac{E_i}{1 + \frac{E_i}{m_e c^2} (1 - \cos \theta)}, \quad (3.4)$$

where E_i is the incoming photon energy, E_f the energy of the outgoing photon, $m_e c^2$ is the rest-mass energy of the electron (511 keV) and θ is the angle of the scattered photon with respect to the original direction (Fig. 3.3) (Knoll 2000).

The possible scattering angle θ of the photon allows energy transfers from the photon to the electron, which has a kinetic energy kT after the scattering, ranging from a nearly unchanged photon energy E_f for a small scattering angle, to the maximum energy transfer in the case of back scattering for $\theta = 180^\circ$. The

differential scattering cross section for the angular distribution of the scattered photons can be derived from the Klein-Nishina formula, which describes the quantum relativistic treatment of the Compton scattering and is presented by, e.g., Leo (1993).

Pair creation

In the pair creation process, which is the dominating effect at energies above 10 MeV for high Z elements (Fig. 3.1, 3.2), the photon is converted into an electron-positron pair. The lower threshold for the photon energy, at which the pair creation mechanism can occur, is given by the rest mass energy of an electron-positron pair: $E_{\text{ph}} \geq 2m_e c^2 = 1.022 \text{ MeV}$. For this reaction to take place an atomic nucleus is necessary as a catalyst to absorb part of the momentum, since it cannot be conserved in the creation mechanism itself. The surplus of photon energy above 1.022 MeV is transferred into kinetic energy of the electron-positron pair. The electron-positron pair itself can create further photons via bremsstrahlung processes and annihilation of the positron. This so called electron-photon shower can sustain itself until the photon energies drop below the pair-creation threshold and is found in, e.g., air showers caused by the interaction from cosmic rays with the atmosphere.

3.2 Semiconductor Detectors

In the periodic lattice of a crystalline material, the wavefunctions of individual electrons can start to overlap, depending on the lattice spacing. Therefore the discrete energy levels of single atoms smear out to bands of allowed and forbidden energy states. Semiconductors like silicon and germanium are situated in the 4th element group, having therefore 4 electrons in the outer shell available to create valence bonds with four neighboring atoms, forming a diamond type lattice. These valence bonds lead in the case of a semiconductor to a filled band, called the valence band. Here no net transfer of charge is possible, since for one electron moving in one direction another electron has to move into the opposite direction, filling up the empty space, they hence just exchange places. The charge carrier density $n(E)$ for an energy interval dE can be written as

$$n(E) = f(E)D(E)dE \quad (3.5)$$

where $D(E)$ is the density of available states and $f(E)$ is the occupation probability. The energy gap E_g located above the valence band is a forbidden region because no non-zero product of the density of available states $D(E)$ and occupation probability $f(E)$ exists here (see Fig. 3.4). The conduction band, where the electrons are free to move through the crystal, is energetically located above the band gap. Through

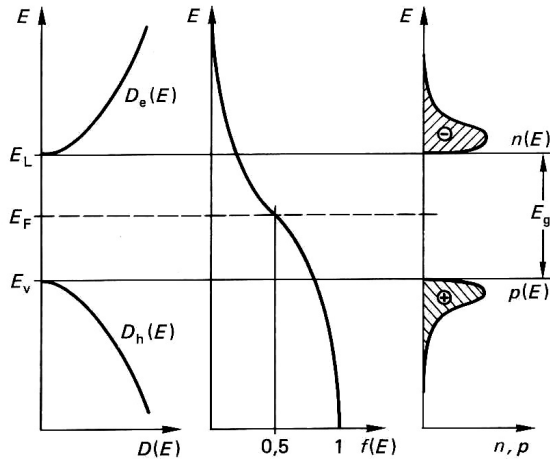


Figure 3.4: Energy dependency of the density of available states $D(E)$, the occupation probability $f(E)$, and the charge carrier density of electrons $n(E)$ and holes $p(E)$ for an intrinsic semiconductor (Hering et al. 2005).

thermal excitation electrons are able to migrate from the valence to the conduction band, leaving behind an empty state in the valence band, called a “hole”-state.

The probability of electrons to occupy a certain energy level is given by the Fermi distribution

$$f_e(E) = \frac{1}{e^{\frac{E-E_F}{kT}} + 1}, \quad (3.6)$$

where k is the Boltzmann constant, T is the temperature and E_F is the Fermi energy (Spieler 2006). Therefore the probability for a vacant state in the valence band, is given by

$$f_h(E) = 1 - f_e(E) \quad (3.7)$$

The electrons have a mobility μ_e and effective mass m_e^* in which the effect of the lattice onto the charge movement is included. Formally, holes can be treated as a net positive charge with corresponding mobility μ_h and effective mass m_h^* (Müller 1991).

The definition of an insulator is that the conduction band cannot be filled with electrons at any temperature through thermal excitation, whereas for a conductor even at low temperatures the conduction band is partly filled. As the occupation probability shows an exponential energy dependence, electrons can populate the conduction band of a semiconductor at a finite temperature. At room temperature

Table 3.1: Properties of semiconductors, compilation from Lutz (1999), Knoll (2000) and Owens & Peacock (2004) and references therein.

Substance	Si	Ge	Cd _{0.9} Zn _{0.1} Te
Atomic number*	14	32	49.1
Atomic mass	28.09	72.59	-
Density [g cm ⁻³]	2.33	5.32	5.78
Dielectric constant ϵ_r	12	16	10
Band gap (300 K) [eV]	1.12	0.665	1.57
Intrinsic carrier density [cm ⁻³]	$1.5 \cdot 10^{10}$	$2.4 \cdot 10^{13}$	-
Intrinsic resistivity [Ω cm]	$2.3 \cdot 10^5$	47	$3 \cdot 10^{10}$
Hole mobility [cm ² V ⁻¹ s ⁻¹]	480	1900	120
Electron mobility [cm ² V ⁻¹ s ⁻¹]	1350	3900	1000
Electron-hole pair energy w [eV]	3.63	2.96	4.64
Fano factor F	0.115	0.13	~ 0.1

* averaged in the case of CdZnTe

the thermal energy corresponds to $kT \approx 0.026$ eV. A semiconductor lies therefore in between the two extreme cases, conductor and insulator.

In an intrinsic semiconductor the amount of electrons and holes produced in thermal equilibrium is equal, therefore the Fermi energy E_F is located in the middle of the band gap E_g . The intrinsic charge carrier density of silicon is $n_i = 1.5 \times 10^{10}$ cm⁻³, corresponding to a resistance of 230 k Ω cm (Knoll 2000)⁵. As pointed out by Spieler (2006), a small band gap in semiconductor detectors leads to the generation of more signal carriers per unit energy of the incoming photon. Note, that the background signal, which is caused by thermal excitation of electron-hole pairs, rises exponentially as well.

The intrinsic charge carrier concentration is generally too low for most of the applications, but can be modified by artificially inserting atoms of neighboring element groups into the crystal lattice. This modification is called doping and can be done with different methods, for instance, with ion implantation or by diffusion. A compact description of processing techniques used in the production of semiconductor detectors is given by Lutz (1999). When atoms from the 5th element group, e.g., arsenic or phosphorus, are used for doping an additional energy level close to the conduction band is introduced due to the extra electron which cannot be incorporated in a valence bond within the diamond lattice configuration.

⁵In reality due to impurities the typical resistance is more of the order ≈ 10 k Ω cm

With thermal energy, this lightly bound electron can then easily be excited into the conduction band, causing the Fermi-energy to be shifted out of the middle of the band gap towards the conduction band, as the negative outweighs the positive charge carrier density. Due to the negative charge of the now dominating charge carriers, the material is called n-doped.

When atoms from the 3rd element group, e.g., gallium, aluminum, or boron are used, one valence electron of the semiconductor is unbound. Energetically this process inserts an energy level close to the valence band, which can be again filled by thermal excitation of an electron from the valence band into this empty lattice space. As a result a hole in the valence band is formed. These dopants are called acceptors and naming this processes p-doping. Like in the case of the n-doping this additional available energy levels cause the Fermi energy to be shifted again, but this time towards the valence band. Typical doping concentrations range from weakly doped material with 10^{12} cm^{-3} to strong doped materials with 10^{18} cm^{-3} impurity atoms (Kern 2002). In the further reading to distinguish different doping concentrations p^+ and n^+ indicate strong doping layers.

3.2.1 *pn-Junction*

When p- and n-doped semiconductor materials are brought together in thermal equilibrium, a large concentration difference of the majority charge carriers exists. The majority carriers, holes for the p-doped and electron for the n-doped areas, will diffuse into the other material, building up a diffusion current. The charge of acceptor and donor atoms left behind cannot be compensated anymore and an electric field emerges, which is oriented from the positive space charges of the donor to the negative space charges of the acceptor atoms. This electric field will cause a drift current in the opposite direction of the diffusion current. At a certain electric-field strength equilibrium is reached and the so called depletion region is formed, where basically no mobile charge carriers exist.

Assuming that for p-doped material $p \gg n_i$ the concentration of holes is much larger than the intrinsic charge carrier density, and vice versa for n-doped material $n \gg n_i$ the potential away from the inhomogeneity is given by

$$V(-\infty) = \frac{kT}{q} \ln\left(\frac{N_D}{n_i}\right) \quad (3.8)$$

$$-V(+\infty) = \frac{kT}{q} \ln\left(\frac{N_A}{n_i}\right) \quad (3.9)$$

leading to a potential difference between the p- and n-doped regions as

$$V_{BI} = \frac{kT}{q} \ln\left(\frac{N_A N_D}{n_i^2}\right) \quad (3.10)$$

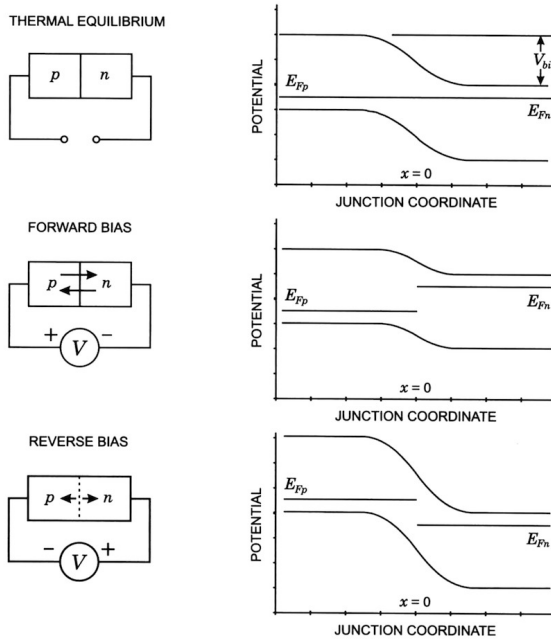


Figure 3.5: Band structure of a pn-junction under thermal equilibrium (top panel), forward biasing (middle), and reverse biasing condition (lower panel). The differences in the potential across the pn-junction can be seen on the right side of the display (Spieler 2006).

which is called diffusion or built-in voltage (Müller 1991). Here kT is again the thermal energy, q is the charge of one electron, n_i is the intrinsic charge carrier concentration, N_D is the donor and N_A the acceptor concentration. The diffusion voltage is a direct result of the different Fermi energies which have to be matched in thermal equilibrium, causing the band structure to be deformed across the pn-junction.

A photon disturbs the local equilibrium between minority and majority charge carriers, by creating electron-hole pairs. In the absence of an electric field the additional electron-hole pairs recombine, establishing the equilibrium in charge carrier concentration again. To measure the amount of charge created, and hence to determine the original photon energy, it is necessary to separate the electrons and holes with the help of an electric field and prevent their recombination.

The potential difference across the pn-junction can be altered by applying an

external voltage to the semiconductor material, as depicted in Fig. 3.5. Applying a positive voltage to the p-doped region with respect to the n-doped region lowers the potential difference over the junction. The diffusion current rises exponentially with the voltage. This is the forward biasing mode of a diode, the technical name of a pn-junction. When the polarity of the applied voltage is changed, the potential difference of the two adjacent regions is increased, the current through the junction is diminished. Reverse biasing of the diode enlarges the depletion region as the electric field strength is increased.

The depletion width in thermal equilibrium is strongly dependent on the doping concentrations and has a typical size in the order of micrometers. In order to make use of the electric field in the depletion region, which acts as an ionization chamber for photons, the depletion width must be enhanced. Lutz (1999) shows that the depleted width d for a reversed biased diode is given by

$$d = \sqrt{\frac{2\epsilon_r\epsilon_0(N_A + N_D)}{qN_A N_D}(V_{BI} + V)} \quad (3.11)$$

where ϵ_0 and ϵ_r are the dielectric constants of vacuum and the material, q the charge of one electron, V_{BI} is the built-in and V the bias voltage, and where N_A and N_D are the doping concentrations of acceptor and donor atoms. Since charge neutrality to the outside of the junction has to be maintained, the depletion width on the p- and n-side of the junction is then given with

$$N_A d_A = N_D d_D. \quad (3.12)$$

In the case of a strong difference in the doping concentrations the asymmetry in depletion extends deeper into the region of lower concentration. Under this condition Eq. 3.11 can be simplified to

$$d = \sqrt{\frac{2\epsilon_r\epsilon_0}{qN_D}(V_{BI} + V)}. \quad (3.13)$$

assuming here a p^+ -doping ($N_A \gg N_D$) and reverse biasing of the junction.

3.2.2 Charge collection

The electrons generated in photoelectric absorption process generate a concentration difference of charge carriers with respect to the surrounding area. With time the concentration difference will disperse and form a Gaussian shaped charge cloud. The variance σ of this Gaussian distribution is given by Spieler (2006) with

$$\sigma = \sqrt{Dt} \quad (3.14)$$

where D is the material dependent diffusion constant and t the time. The diffusion constant D is linked to the mobility μ of the charge carriers via the Einstein relation

$$\mu = \frac{q}{kT}D \quad (3.15)$$

In silicon at a temperature of 300 K the mobility of the electrons is $1350 \text{ cm}^2 \text{ V}^{-1} \text{ s}^{-1}$ and $480 \text{ cm}^2 \text{ V}^{-1} \text{ s}^{-1}$ for holes (Müller 1991). The transport equation of charge carriers in a semiconductor is given by

$$\vec{j} = qn\vec{v}_e + (-q)p\vec{v}_h \quad (3.16)$$

where \vec{j} is current density, q the charge, $\vec{v}_{e,h}$ are the according carrier velocities, and n/p the number density of electrons, respectively holes. The velocity achieved by charge carriers in a semiconductor scales with the mobility μ and electric field like

$$\vec{v}_{e/h} = \mu_{e/h}\vec{E}. \quad (3.17)$$

This relation is basically valid up to $\vec{E} < 10^5 \text{ V cm}^{-1}$, above this field strength the velocity attains a constant value, as an increase in the collisions of charge carriers with the lattice limits the mobility (Sze 1981).

When an electric field is superimposed to the diffusion of charge carriers, as it is present in a depletion region, it is possible to compute the final charge cloud size after the drift to the potential minimum. This is an important value for pixelated structures, since the charge cloud size has a distinctive influence on the position and energy resolution of a detector.

To determine the size of the charge cloud it is necessary to estimate the time the charge carriers need to drift to the potential minimum (here for example derived for electrons). In order to apply Eq. 3.17, information about the strength of the electric field at the interaction point in the distance x from the potential minimum is needed, which is given by

$$\vec{E}_x = -\left(\frac{V + V_{\text{dep}}}{d} - \frac{2xV_{\text{dep}}}{d^2}\right) \quad (3.18)$$

where V is the applied and V_{dep} the voltage needed for the depletion of a slab with thickness d (Lutz 1999). Since

$$\vec{v}_{e/h} = \frac{d}{dt}x = \mu_{e/h}\vec{E} \quad (3.19)$$

the time electrons need to drift to the potential minimum can be obtained by inserting Eq. 3.18 for the electrical field and integrating over dt

$$t_{\text{drift}} = \frac{d^2}{2\mu_e V_{\text{dep}}} \ln \left[\frac{V + V_{\text{dep}}}{V - V_{\text{dep}}} \left(1 - \frac{x}{d} \frac{2V_{\text{dep}}}{V + V_{\text{dep}}} \right) \right]. \quad (3.20)$$

Together with Eq. 3.14 and Eq. 3.15 the drift time t_{drift} can be used to calculate the resulting charge cloud size σ_{cc} . Typical reported sizes in silicon for a depletion width of $450\mu\text{m}$ are of the order of $\sigma_{\text{cc}} \approx 10\mu\text{m}$ (Strüder 2000).

In addition to the diffusion processes described above, the repelling Coulomb force between the electrons has to be taken into account when the exact charge cloud size needs to be calculated. A detailed analysis using a mesh experiment to determine the charge cloud size for different photon energies is presented by Kimmel et al. (2006a,b).

3.2.3 Ionization Statistics

The generation of electron-hole pairs in semiconductors is governed by statistical means. For photon energies comparable to the band gap an excitation of an electron from the valence band to the conduction band is possible if the correct wavevector is transferred from the photon momentum to the electron-hole pair. The wavevector at which the minimum potential of the conduction band is aligned with respect to the maximum of the valence band, distinguishes the direct (zero momentum) from indirect (offset by a certain wavevector) semiconductors. Silicon (Si) and germanium (Ge) are typical examples of indirect semiconductors, whereas gallium-arsenide (GaAs) is a direct one. In silicon a simultaneous transfer of energy and momentum is required in the excitation process, with the momentum going into lattice vibration (phonons) and therefore eventually ending up as thermal energy in the detector. A more detailed description can be found in Spieler (2006). X-ray and gamma-ray photons have a much higher energy than the band gap, they carry therefore also more momentum which has to be absorbed by the crystal lattice. As reported by Scholze et al. (1999), the energy needed to effectively generate an electron-hole pair in silicon is basically constant for photon energies between 10 eV–20 keV with a value of $w = 3.66\text{eV}$. Keeping the band gap of silicon with $E_{\text{g}} = 1.12\text{eV}$ in mind, this means that only 30% of the energy is needed for the ionization process, while 70% of the available energy is going into phonon excitation.

One would naively expect, that such a process can be described using Poisson statistics, which is a discrete probability distribution used in the case of large event numbers, where each individual event has only a rare chance to occur. For a Poisson distribution the standard deviation σ is given by the square root of the mean, resulting in

$$\sigma = \sqrt{N} = \sqrt{\frac{E_{\text{ph}}}{w}} \quad (3.21)$$

where N is the number of generated electron-hole pairs, E_{ph} is the photon energy, and w is the average energy for electron-hole production.

Measurements show that the energy resolution $\Delta E/E$ obtained with a semiconductor based detector can be better than what is estimated under the assumption that fluctuations are governed by pure Poisson statistics.

Because of conservation of energy, the incoming photon energy will lead to a number of ionizations N_{ion} and phonon excitations N_{vib} . For the photon energy follows

$$E_{\text{ph}} = E_{\text{ion}}N_{\text{ion}} + E_{\text{vib}}N_{\text{vib}} \quad (3.22)$$

where E_{ion} is the energy needed for a single electron to be excited into the conduction band and E_{vib} as the mean energy for phonon excitation, and under the assumption that $E_{\text{vib}} \ll E_{\text{ion}}$. Since there is only one fixed amount of energy available for the reaction, the average fluctuations in the distributions must compensate each other,

$$E_{\text{ion}}\Delta N_{\text{ion}} = E_{\text{vib}}\Delta N_{\text{vib}}. \quad (3.23)$$

Therefore the ionization and phonon excitation processes cannot be completely independent from each other, biasing the fluctuations and hence distorting the variance away from pure Poisson statistics. Equation 3.23 can be rewritten in terms of σ

$$\sigma_{\text{ion}} = \frac{E_{\text{vib}}}{E_{\text{ion}}} \sqrt{N_{\text{vib}}}. \quad (3.24)$$

As shown by Spieler (2006) this equation can be reformed in terms of the fixed photon energy E_{ph} and a result of the form

$$\sigma_N = \sqrt{FN} \quad (3.25)$$

is obtained, where N is the number of charge pairs created for a given energy and F is the Fano factor. This result was first shown by Fano (1947) for gas detectors, but holds also true for semiconductor detectors. The Fano factor can be thought of as the value by which these distributions differ.

From the variance of the generated electron-hole pairs σ_N the according energy variance σ_E can be calculated with

$$\sigma_E = \frac{\sigma_N}{N} \cdot E = \frac{E}{N} \sqrt{\frac{FE_{\text{ph}}}{w}} = \sqrt{wFE_{\text{ph}}}. \quad (3.26)$$

The Fano limited achievable energy resolution for a Gaussian distribution in terms of Full Width Half Maximum is then given by

$$\Delta E_{\text{FWHM}} = 2.35 \cdot \sigma_E. \quad (3.27)$$

For silicon as a semiconductor the ionization energy E_{ion} corresponds to the band gap energy $E_{\text{ion}} = 1.12$ eV. The average phonon energy is $E_{\text{vib}} = 0.0037$ eV,

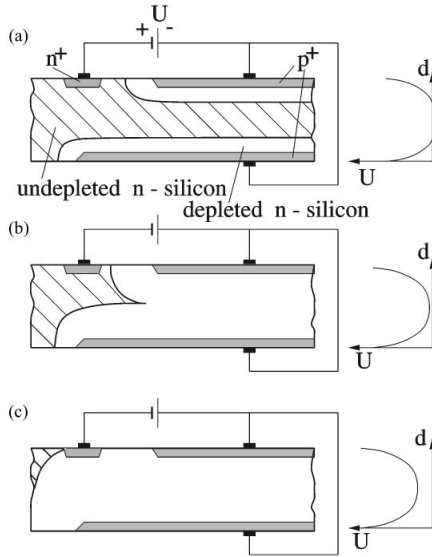


Figure 3.6: Sideways depletion in the case of a) no applied external voltage, b) the enlarged depletion zones with external voltage, and c) over depletion (Strüder 2000).

and the energy needed to create an electron-hole pair is $w = 3.66$ eV. Perotti & Fiorini (1999) measured the Fano factor for X-rays between 6–120 keV and a temperature of -35°C to a value of $F = 0.12$. With these values a 6 keV photon creates on average $\langle n \rangle = 1639$ electron-hole pairs in an interaction process. The best energy resolution one can expect to achieve at 6 keV in a silicon detector is about ≈ 120 eV.

3.2.4 Sideways Depletion Principle

The sideways depletion principle was introduced in a famous paper by Gatti & Rehak (1984) in which they proposed the silicon drift detector. Kemmer & Lutz (1987, 1988) presented various implementation possibilities of this novel concept, creating a new generation of silicon detectors.

Technically the principle is based upon the idea that a wafer can be depleted with just one small ohmic n⁺-contact that is located anywhere on the bulk and two rectifying junctions on either side of the wafer (see Fig. 3.6). The rectifying junctions are formed by a thin strongly p⁺-doped layer (boron with a concentration of $N_A = 10^{19}$ cm⁻³) located on both sides of a high resistivity n-type wafer of about $4\text{ k}\Omega$ cm, which corresponds to a donor concentration of $N_D = 10^{12}$ cm⁻³.

Applying now a negative voltage to both p^+ -layers with respect to the n^+ -contact, two reverse biased diodes are created, separated by the bulk material. The low doping concentration of the bulk will cause it to be predominantly depleted. When the reverse biasing voltages are increased the depletion regions will begin to merge, forming a potential minimum for electrons, pushing back the conductive region of the bulk towards the n^+ doped region, which serves as readout anode for the electrons (Lutz 1999).

A recent review of the broad application range is shown by Lutz (2006). The pn-CCD on *XMM-Newton* is based on this principle (Strüder 2000; Strüder et al. 2001), as well as the frame-store CCD (Meidinger et al. 2004), the DePFET (Lutz 2005; Treis et al. 2005a), including the macropixel concept (Zhang et al. 2006), and the silicon drift detector (Lechner et al. 2001).

The advantages offered by this principle are that the vertical position x of the potential minimum

$$x = \frac{d}{2} + \frac{\epsilon_r \epsilon_0}{qdN_D} (V_b - V_f) \quad (3.28)$$

can be influenced by the voltages applied to the front V_f and backside V_b under the assumption of a constant bulk doping concentration N_D . If the biasing voltages are not symmetric for front and backside, the potential minimum can be moved away from the center of the bulk to, e.g., the front side by making V_b more negative than V_f . The voltage needed to totally deplete the complete thickness of a silicon wafer ($d = 300 - 450 \mu\text{m}$) can be reduced using the principle of sideways depletion. As can be seen in Eq. 3.11 the depletion width scales as $d \propto \sqrt{V}$. By creating two depletion regions only a quarter of the voltage is needed in order to deplete the whole thickness of a wafer. In addition a layer of donors with a concentration of $\sim 10^{14} \text{ cm}^{-3}$ near the front side can be used to model the potential minimum to a even more suitable shape, as described by Wölfel (2007).

The sideways depletion principle allows the complete thickness of a wafer to be used as detector. This is essential for the detection of X-rays, as the cross section for photo absorption scales with the photon energy $\propto E^{-3}$ (see Sect. 3.1.1). The quantum efficiency (QE) is above 90% for the pn-CCD of *XMM-Newton* in the range of 0.6–10 keV (Strüder et al. 2001) which has as thickness of $270 \mu\text{m}$. The usage of $450 \mu\text{m}$ thick wafers of the current detector generation produced at the Max-Planck-Institut Halbleiterlabor (MPI HLL) led to an increase in the QE at higher energies, e.g., the frame-store CCDs used for *eRosita* show unprecedented efficiencies of 20% at 30 keV as reported by Strüder & Meidinger (2008). The same wafer thickness is planned to be used for the *XEUS* WFI (Turner & Hasinger 2007) and the *Simbol-X* LED (Ferrando et al. 2006).

Furthermore, with the sideways depletion principle, the size of the readout node can be handled independently from the charge collection area, since the electric

field in the depleted region transports the generated electrons to the anode. In order to maximize the output voltages of a detector element

$$U_{\text{out}} = \frac{Q_{\text{ph}}}{C_{\text{tot}}} \quad (3.29)$$

it is indispensable to minimize the readout capacitance C_{tot} for a fixed amount of charge Q_{ph} . This is the prerequisite to build low noise detectors. Readout capacities of 50 fF have been reported for silicon drift detectors by (Strüder 2000), resulting in a sensitivity of $3.2\mu\text{V}$ per electron created.

Besides the readout capacity the leakage current plays an important role in the performance of low noise detectors. Controlling and optimizing the production chain to obtain devices with low leakage current is inalienable, since signal and leakage current cannot be distinguished from each other. Leakage current in the bulk material originates mainly from the thermal generation of electron-hole pairs at metallic impurities and crystal defects. It increases with the depleted volume, but can be reduced by cooling the device (Knoll 2000). The current detector generation produced by the MPI HLL has extremely low leakage currents of 0.1 nA cm^{-2} for a bulk thickness of $500\mu\text{m}$ (Strüder & Moser 2007).

3.3 MOSFET

The Metal-Oxide-Semiconductor Field Effect Transistor (MOSFET) belongs to the family of technologically important Field Effect Transistors (FETs), together with the Junction FET. They form the group of the unipolar transistors, as only one type of charge carrier is needed in order to describe the functionality. This is different from the bipolar npn- / pnp-transistors where both, electrons and holes, are required in the functional description. The concept of the FET offers various advantages, such as power-less steering as no current can flow through the gate, leading to high input impedance. In integrated circuits MOSFETs are used due to low power consumption and easy size scalability, which makes small structures possible (Horowitz & Hill 1999).

In order to understand the processes taking place in a MOSFET a closer look at the effects in a metal-isolator-semiconductor (MIS) interface is helpful. In this case an insulator exists between the metallic contact and the doped semiconductor whose band structure is changed in the vicinity of the boundary. Depending on the semiconductor type and the voltage applied to the metal, four different working configurations can be obtained. They are explained below for a n-type MOS structure and depicted in Fig: 3.7 (for a p-type MOS, switch the signs of the voltages and charge carriers):

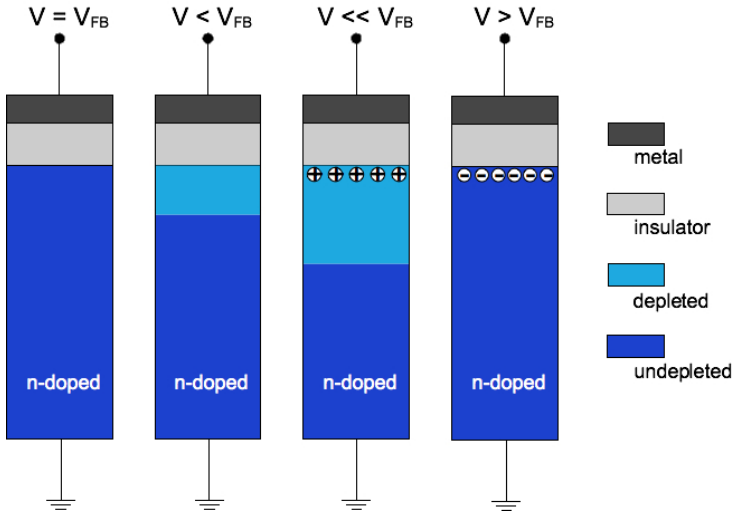


Figure 3.7: Metal-Insulator-Semiconductor interface of an n-type structure. From left to right are the conditions for *flatband*, *depletion*, *inversion*, and *accumulation*.

- flatband** V_{FB} - uniform charge carrier concentration in the semiconductor
 The voltage V_{FB} matches the difference between the Fermi energy E_F and the work function of the metal, the bands are flat in the semiconductor up to the insulator layer (no electric field at the boundary).
- depletion** $V < V_{FB}$ - insulating layer at the interface
 When a small negative voltage is applied to the metal, the electrons will be pushed away from the interface, leaving behind a positive space charge.
- inversion** $V \ll V_{FB}$ - minority carrier form a thin conducting layer
 When the negative voltage is further increased, thermally generated electron-hole pairs will be separated by the electric field in the depleted region, resulting in a layer of holes at the interface.
- accumulation** $V > V_{FB}$ - majority carriers form a conducting layer
 When a positive voltage is applied to the metal with respect to the semiconductor, electrons from the semiconductor will be drawn towards the insulation layer, forming a negatively charged layer at the interface between semiconductor and insulator.

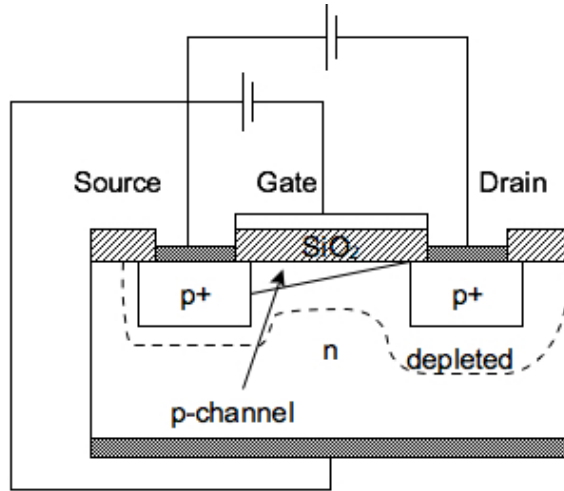


Figure 3.8: Cross section through a p-channel MOSFET.

A more mathematical description of the MIS interface, especially the bending of the semiconductor band structure in the vicinity of the metal-insulator layer is presented by [Lutz \(1999\)](#).

The basic operation of a MOSFET will be explained using a p-channel MOSFET (shown in Fig. 3.8), as it is used as the gate transistor in the DePFET detector. The bulk of a p-channel MOSFET is made out of n-doped silicon, the source⁶ and drain are regions with a p⁺-doping. An insulating layer is placed between the gate electrode (metal or polysilicon) and the semiconductor bulk, realized in the case of a MOSFET with silicon-dioxide (SiO₂). For the further description it is assumed that the source is short-circuited to the substrate and serves as a reference for the voltages. The influence of the substrate on the MOSFET, as well as other second order processes like the channel shortening, will be neglected (see [Tietze & Schenk \(2002\)](#) for details).

A negative voltage V_D applied to the drain operates this diode in reverse bias, therefore no current can flow between source and drain. When the gate voltage V_G surpassed the threshold voltage V_T a conducting channel starts to form and the

⁶the source is defined as the area of origin of the majority charge carriers, which flow through the channel to the drain area

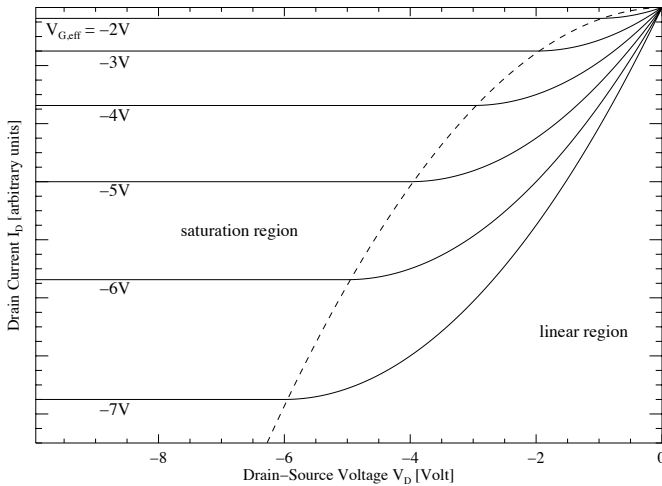


Figure 3.9: Current-voltage characteristics of a p-channel MOSFET. The dashed line indicates the saturation voltages $V_{D,\text{sat}}$ for an assumed threshold voltage of $V_T = -1$ V (after Tietze & Schenk 2002).

drain current I_D can start to flow from source to drain:

$$I_D = -\frac{W}{L}\mu_p C_{\text{ox}} \left[(V_{G,\text{eff}} - \frac{V_D}{2}) V_D \right]. \quad (3.30)$$

Here W is the width and L the length of the gate, μ_p is the hole mobility and C_{ox} is the capacity of the oxide per unit area and

$$V_{G,\text{eff}} = V_G - V_T \quad (3.31)$$

is the effective gate voltage (Lutz 1999).

One of the important parameters of a MOSFET is the transconductance g_m , quantifying the change of the drain current I_D with a change in the gate voltage V_G , while keeping the drain voltage V_D constant

$$g_m = \left. \frac{\partial I_{D,\text{sat}}}{\partial V_{G,\text{eff}}} \right|_{V_D=\text{const}}. \quad (3.32)$$

The equation 3.30 for the drain current I_D is valid as long as $V_D < V_{G,\text{eff}}$. Due to the negative voltage of the drain with respect to the source, the conducting channel is smaller at the drain end. If V_D is increased above $V_{G,\text{eff}}$, the depletion

region around the drain contact grows, the channel will be pinched off when the channel conductivity at the surface to the oxide reaches zero near the drain end. A change in the drain voltage V_D is not reflected by a change in the drain current I_D anymore. This is the saturation condition, for which $V_{D,sat} = V_{G,eff}$. The two different operation regimes, linear and saturation, of a MOSFET are displayed in Fig. 3.9.

Under saturation the transconductance $g_{m,sat}$ is constant and given by

$$g_{m,sat} = -\frac{W}{L}\mu_p C_{ox} V_{G,eff}. \quad (3.33)$$

Depending on the type of the conducting channel (p- or n-) two different types of MOSFETs can be built. Each of these can have two subtypes, called enhancement and depletion mode. The first one was explained above, in the case of the depletion mode an additional doped region is implanted under the gate. Therefore a conducting channel exists, causing a current I_D to flow even when the gate is not biased. This depletion mode is also referred to as *normal on*. To turn the transistor off, the gate has to be biased in a way that inversion occurs. This behavior does not influence the general characteristics of a MOSFET as derived above, only a shift in the threshold voltage V_T has to be accounted for.

The DePFET Detector

“... no one believes an hypothesis except its originator but everyone believes an experiment except the experimenter.”

[W. I. B. Beveridge]

In this chapter general considerations on the concept of DePFET detectors are presented. The fundamental principles of the DePFET are explained, followed by a short overview of the different existing detector variants in Sections 4.2–4.3. As next step, the DePFET matrix and the essential front-end electronics are introduced in Section 4.4. The second part of this chapter is dedicated to the data acquisition system, starting at Section 4.5, where the individual components of the laboratory setup are described.

4.1 General considerations

In X-ray astronomy spectral imaging is possible when the arrival time, position, and energy are recorded from each photon. A necessary constraint therefore is the design of detectors with fast readout and low-noise capabilities. Favored is hereby the fabrication of the detector and readout electronics on one single chip.

The *Depleted P-channel Field Effect Transistor Detector* (DePFET, see Fig. 4.1) is an Active Pixel Sensor (APS) which is developed and produced by the MPI HLL in Munich. It was first proposed by [Kemmer & Lutz \(1987\)](#) as new structure for a position sensitive semiconductor detector based on the sideways depletion principle introduced in Section 3.2.4. Experimental proof of the DePFET feasibility was given by [Kemmer et al. \(1990\)](#) soon afterwards.

For each DePFET pixel a MOSFET structure is placed on top of a depleted bulk, implementing the first amplification stage at the position of the charge generation. The free electrons generated by the photon interactions are stored close to the point

of origin in a potential minimum within the pixel. The DePFET detector combines photon detection and signal amplification at the position of the charge generation with a low output capacitance. The first results of measurements on a single pixel for the WFI have been reported by [Strüder et al. \(2004\)](#).

In contrast to X-ray sensitive CCDs used on, e.g., *XMM-Newton*, no charge needs to be transferred for the readout of the signal information, thus no *charge transfer inefficiency*¹ (CTI) degrades the signal. Furthermore through the omitting of the charge transfer no *out of time events*² can occur. A detailed description for both effects is presented by, e.g., [Ehle et al. \(2008\)](#).

Making the first amplification of the signal on site, reduces the detector sensitivity to noise induced by mechanical vibrations (microphony) and electrical interference ([Strüder & Moser 2007](#)). Bond wires between detector and the first amplifier become no longer necessary, reducing possible sources of stray capacitances. As already pointed out in Section 3.2.4 a small anode size usually leads to a small capacitance, which is a mandatory prerequisite for low-noise readout. The on-chip amplification in combination with the low capacitance of the *internal gate* allows fast readout speeds while still maintaining a good signal-to-noise ratio and an exceptional energy resolution as shown later on. Since the photon sensitive volume and the size of the readout node are decoupled, the photon sensitive volume can be increased with drift rings, as shown in Section 4.3, without degradation of the signal-to-noise ratio.

Because the damageable structured front side is self shielded through the bulk material, the DePFET is radiation hard as the device is usually irradiated on the homogenous p-doped backside. Radiation tests with X-ray doses of the order of ~ 1 MRad are reported by [Treis \(2005\)](#), resulting mainly in threshold voltage shifts due to the damaging of the MOS interface layer, an effect which can be compensated for.

¹The CTI, which describes the charge loss due to the multiple shiftings of the signal electrons in a CCD towards the readout anode, can be as low as 10^{-5} for one shift process of the frame store pn-CCD ([Meidinger et al. 2006](#)). The effect of the CTI, a lowered signal value for pixel with more shift processes, can be corrected, but an additional noise component is induced. As the charge transfer happens in a depth of about $\approx 10\mu\text{m}$, a degradation of the efficiency with time is expected, as radiation damage in orbit generates further trapping centers close to the surface of the CCD.

²*Out of time events* are events that are recorded during the charge transfer, when part of the image has already been transferred for readout and a photon hits the detector at the source position, but subsequently is recorded at a wrong pixel position ([Kendziorra et al. 1999](#)).

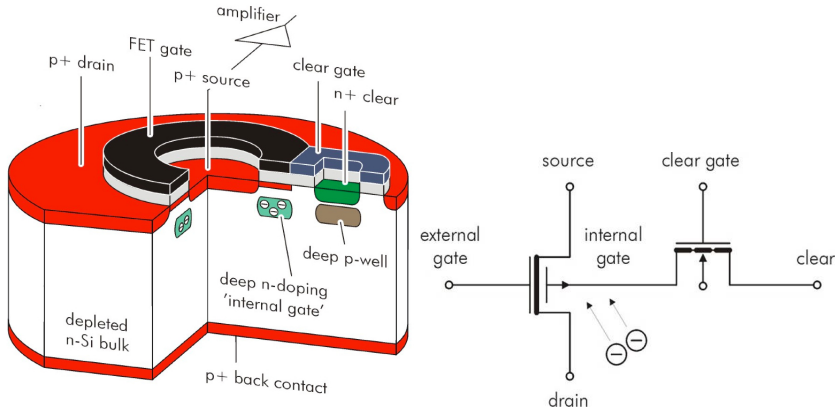


Figure 4.1: Model of a DePMOSFET pixel. The left panel shows the circular deep-n implant of the *internal gate* as well as the surface structure of the MOSFET, with the corresponding source, gate (black) and drain. Drawn in blue is the MOSFET for the *clear* operation with the *clear* and *clear gate* contacts shown above the shielding deep p-well. On the right-hand side, a representation of the DePFET equivalent circuit consisting of two transistor symbols is shown (Lechner et al. 2006).

4.2 The DePMOSFET

In a DePMOSFET pixel, as shown in Fig. 4.1, a p-channel MOS Field Effect Transistor (MOSFET) is integrated on the front side of a completely depleted bulk. The source and drain contacts are p^+ -doped regions in a n-doped bulk material. Under the circular shaped gate of the MOSFET, further referenced as external gate, an additional shallow p-doped region is implanted, making this configuration a depletion mode FET. In the further reading, if not denoted otherwise, the term DePFET refers to the DePMOSFET³.

The backside voltage is applied in a way that a potential minimum for electrons is created and shifted to the front side. A zone with a n^+ -doping is implanted in a depth of about $1\ \mu\text{m}$ under the channel of the external gate. This approach enhances the potential minimum, thus making it more attractive for electrons and helps to confine them in lateral direction under the external gate. Because of its resemblance to the functionality of a MOSFET gate this n-doped region is called the *internal gate*. Up to 10^5 electrons can be stored in the internal gate (Treis et al. 2005a).

³DePJFET pixels were an alternative studied earlier on (Klein et al. 1997), but discarded for technological reasons in the production of large scale detectors.

Electron-hole pairs created in the depleted bulk are separated by the electrical field. The electrons are collected in the potential minimum of the *internal gate* while the holes drift to the p^+ -doped backside. The conductivity of a MOSFET channel depends on the biasing voltages of the three contacts, source, gate and drain for a given FET geometry. Through the *internal gate* another element is added. The electrons accumulated in the *internal gate* influence mirror charges, i.e., holes, in the p-channel of the MOSFET, therefore changing the channel conductivity.

The charge transconductance g_q (modeled after the transconductance g_m of a MOSFET, explained in Section 3.3) can be written as

$$g_q = \frac{\delta i}{\delta q_{IG}} \quad (4.1)$$

and relates the presence of electron charges δq_{IG} in the *internal gate*, with the resulting current change δi in the MOSFET channel between source and drain. *Internal gate* sensitivities of $g_q \sim 200\text{--}300$ pA per electron have been reported by Treis et al. (2006b). The actual value for g_q depends on the exact geometric properties of the DePFET, e.g., the doping profiles or the size and shape of the external gate.

As the charge accumulated in a potential minimum is not measured directly, but through the channel conductivity, the charge is not influenced by the readout process, therefore an additional n^+ -doped *clear* contact is implanted, where a positive *clear* voltage can be applied to remove the electrons from the *internal gate*.

In order to prevent charge loss from electrons which are drifting from the *internal gate* to the n-doped *clear* region, a MOS structure on the front side of the pixel is added, which surrounds the *clear* contact and is called the *clear gate*. It can be thought of as an n-channel FET, with the *internal gate* as *source* and the *clear* contact as *drain*, hence explaining the given name. The *clear gate* is kept at a negative voltage during integration time, forming a potential barrier between the *clear* contact and the *internal gate*. Through this, a possible charge injection from the n^+ -doped *clear* contact to the *internal gate* can be suppressed. On the other side, by a proper biasing of the *clear gate* during the clear process a conducting n-channel between *clear* and *internal gate* can be established, allowing an easy removal of the electrons at a *clear* voltage lower than possible without the presence of the *clear gate* structure.

Precaution has to be taken that during integration no electrons will drift to the *clear* contact instead of drifting to the *internal gate*. For this purpose a depletion zone is created by a p^+ -volume underneath the n^+ -doped *clear* contact shielding it from the bulk and the *internal gate*. This depletion zone interferes with the charge removing process from the *internal gate* thus requiring a higher *clear* voltage.

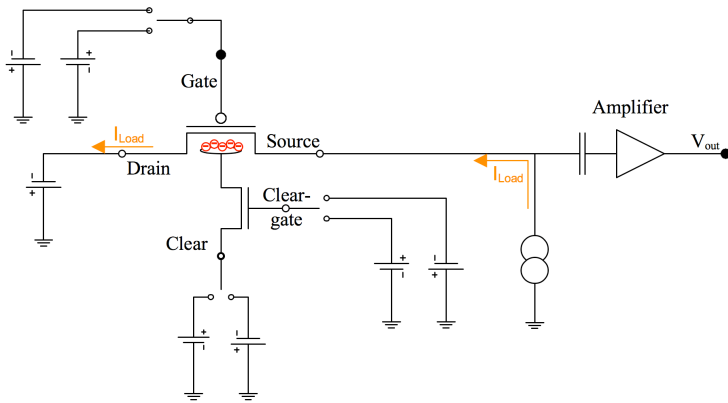


Figure 4.2: Connection scheme of a DEP-FET pixel for a source follower readout. The *gate*, *clear gate* and *clear* can be toggled between an on and off voltage. On the right side, the input stage of the voltage sensitive amplifier is shown, as well as the current source.

4.2.1 Operating principles

In order to determine the amount of electrons gathered in the *internal gate* and hence the incoming photon energy, the change in the channel conductivity of the DePFET must be measured. This can be achieved either with a measurement of the drain current or with a source follower configuration. Since the drain current readout method for the *IXO*- and *Simbol-X* matrices has been implemented only recently⁴, it will not be subject of further discussions in this thesis.

In the case of the source follower readout, shown in Fig. 4.2, a current source is used to apply a constant current I_{Load} through the source and drain contacts of the pixel. The drain voltage V_{Drain} is kept constant and when the external gate is turned on with V_{Gon} and after a settling time the voltage at the source contact adjusts itself to a value which depends on the channel conductivity. Measuring the source voltage before and after the clear process leads to a voltage difference which corresponds to the number of electrons collected in the *internal gate*. The amplitude of the voltage step v_s between signal and baseline voltage is derived by

⁴At the time the experimental setup was realized at IAAT, only single pixel devices and small 4×4 matrices were available for the drain current measurement method. Details on this subject are given by Wölfel (2007).

Treis et al. (2006b) in the small-signal case with

$$v_s = \frac{g_q}{g_m} \Delta Q_{\text{sig}}. \quad (4.2)$$

where ΔQ_{sig} is the amount of charge in the *internal gate*. The figure of merit for the source follower readout is the ratio between the transconductance g_m and charge transconductance g_q of the DePFET.

Even in the absence of radiation the *internal gate* will slowly fill up with time, through thermally generated electrons, finally reaching an equilibrium state where electrons are leaked to a more positive potential. To prevent such a charge leakage from the *internal gate*, which results in a sensitivity loss because additional charge cannot be stored, a cyclic removal of the electrons is necessary.

For a regular operation sequence of a DePFET, the voltages of the contacts for the *gate*, *clear gate*, and the *clear* have to be switched between the on- and off-states. Figure 4.3 shows the sequence of the applied voltages for one DePFET operation cycle. During the charge integration time the voltages V_{Goff} , V_{CGoff} , and V_{Coff} are applied to the DePFET. For the readout the DePFET is turned on with the V_{Gon} voltage. After the source voltage measurement, the positive *clear* voltage V_{Con} is applied to the *clear* contact. With the switching of the *clear gate* voltage to V_{CGon} , the conducting channel is established and the charge can be removed from the *internal gate*. First the *clear gate* voltage is returned to V_{CGoff} and afterwards the *clear* to V_{Coff} . With this sequence it is ensured that no electrons gathered under the *clear* contact during the *clear* process can drift back to the *internal gate* via the *clear gate*.

One of the advantages of the DePFET sensor is that the potential minimum of the *internal gate* exists independently of the status of the *external gate*. Therefore to save power the pixel can be turned off via the *external gate* voltage V_{Goff} during the integration time, while charge is still accumulated.

The *internal gate* is capacitively coupled to the *external gate* and its potential can therefore be influenced with V_{Goff} , enhancing or diminishing the charge handling capability. If V_{Coff} is chosen to be too negative, charge injection from the n^+ -doped *clear* into the *internal gate* is possible. Setting V_{CGoff} too positive, charge can leak out from the *internal gate* to the *clear* contact. If V_{Con} is not high enough a complete *clear* can not be achieved, as charge remains in the *internal gate*. Each of these voltages has direct influence on the operational properties of a DePFET pixel and depend on each other, thus making it necessary to fine tune the potentials inside the pixel.

One crucial step in the operation of a DePFET is the clearing of the *internal gate*. If the electrons are not completely removed, the measured baseline is shifted with respect to the true baseline and as result a smaller voltage difference is obtained,

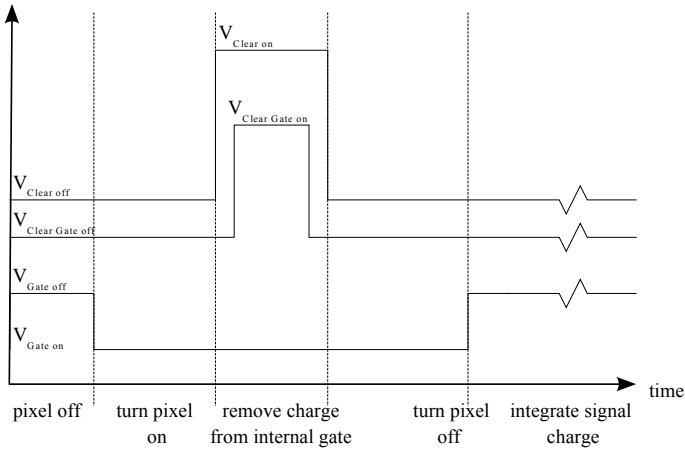


Figure 4.3: Timing sequence of the toggled DePFET voltages for the *gate*, *clear gate* and *clear*.

eventually leading to a measured photon energy which is too low. The remaining charge can be detected during the next readout as an event with low energy. This effect is called “clear correlation” and depends on the operating voltages and on geometrical parameters as shown later on in this chapter. Furthermore since the charge left behind in a pixel can be variable, an additional noise component, the reset noise, is added which worsens the excellent energy resolution. Treis et al. (2005a) show that in principle a complete clear with the current prototypes is possible.

During the clear process radiation cannot be detected, since the generated electrons drift directly into the *clear* contact instead of the *internal gate*, and hence are lost for detection. It is therefore absolutely necessary to minimize the time needed for the *clear* process, while maintaining a complete charge removal from the *internal gate*. As shown in Fig. 4.3, the time of the *clear* process is not given by the duration of the *clear* pulse, but by the time the conducting channel between *internal gate* and *clear* contact exists and hence by the length of the *clear gate* pulse. The effective duration of the *clear* process in our setup, which is presented in the next section, is typically ~ 300 ns, but as pointed out by Treis (2005) *clear* durations of 50 ns are expected to be achievable.

4.2.2 DePFET variants

In the search for the optimal DePFET, a multitude of different geometries and layouts has been investigated and some of them are still under study. In this work, only options relevant for the DePFETs used at the IAAT are mentioned briefly. The advantages and disadvantages of the different implementations are discussed in greater detail by Treis (2005).

The general design of the DePFETs used for astrophysical applications is based on a *circular* geometry, in contrast to the *linear* pixel design for the collider experiments (see Fischer et al. 2007; Lutz et al. 2007b, and references therein). The circular gate, as seen in Fig. 4.1 and 4.4, has a width of $5\mu\text{m}$ and a circumference of $47.5\mu\text{m}$ and is located on a wafer with a thickness of $450\mu\text{m}$. The matrix can be realized such that no insensitive gaps between adjacent pixels exist and a filling factor of 100% can be achieved.

Due to the electric field geometry an improved charge collection can be observed as compared to the linear design. The latter one allows a more compact pixel size, needed for high spatial resolution in Vertex detectors, whereas for astrophysical applications the combination of spectral and spatial resolution, matching the angular resolution of the optics, is important.

The location of the source within the DePFET is one crucial design parameter. In the *source center* (SC) design it is located inside the circular gate, as seen in Fig. 4.1, in the case of the *drain center* (DC) it is on the outside of the circular gate. As *source* and *drain* are symmetric for the operation and the readout of the DePFET, no operation difference exists in principle between the DC and SC case. But slight performance deviations between the two options are noticeable. The *source center* DePFETs of the first production generation (PXD04) showed charge loss (Treis et al. 2006a). The reason was thought to be the lack of a drift field under the *clear gate* during the charge integration. Therefore charge was accumulated under the *clear gate* and removed in the following *clear* cycle, without being first collected in the *internal gate*. This effect is not observed for the *drain center* pixel. The smaller source area for the SC variant decreases the capacity of the source, an important parameter for fast and low-noise readout.

The size and the alignment of the deep-p well used for shielding the clear contact from the depleted bulk is another design option. Two variants exist, the *P0* and the *P1* type, differing by the amount of overlap with the *clear gate*. For the *P0* type the deep-p has no overlap with the *clear gate* and ends with the edge of the n^+ of the *clear*. In the *P1* case the overlap of the deep-p is up to half the width of *clear gate*. For the *P0* option charge loss into the *clear* contact is possible if the lateral position of the deep-p is not exactly matched and leaves part of the *clear* contact uncovered. Additionally, charge injection into the *internal gate* by a too negative

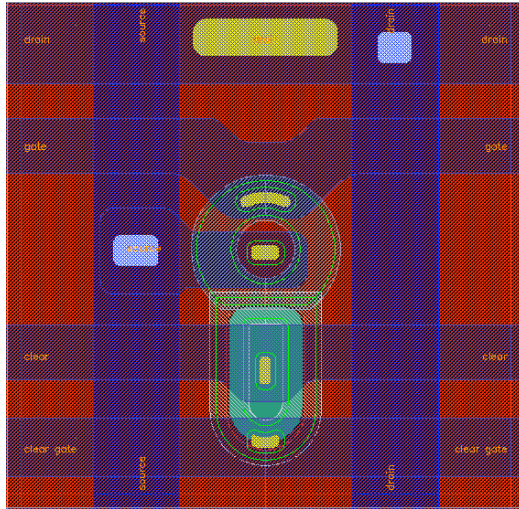


Figure 4.4: Layout of the PXD05-Vertex variant of the DePFET. Here, the *source* is in the center of the gate (green circle). The lilac vertical lines are the contact lines for *source* and *drain*, the 3 horizontal lines are from bottom to top the *clear gate*, *clear* and *gate* transfer lines. Drawn in yellow are the contact points between the lines and the corresponding DePFET element. The green outlines show the polysilicon layers forming the *external gate* of the transistor and the *clear* structure (Image courtesy of J. Treis).

V_{Coff} voltage becomes more easy. The disadvantage of the *PI* option is that the necessary voltage V_{Con} for a complete *clear* is increased to about $\sim 18\text{--}20\text{ V}$.

In Fig. 4.4 the pixel layout of the Hybrid 42, which is currently used at the IAAT, is depicted. This hybrid is a *source center*, cut gate, *P0* pixel matrix, where the cut gate option refers to the truncated *external gate* at the location of the *clear gate*. Hybrid 42 is a test matrix, for which the contact of the *clear gate* has been moved from the usual position on the left side close to the *gate*, downwards to the crest of the *clear gate* structure. This is done in order to eliminate a contraction of the *clear gate* by the contact hole close to the transfer region between *clear* and *internal gate*, and thus trying to eliminate the charge loss mechanism and to increase the charge collection efficiency for the *source center* pixels. For the PXD05 production run, 2 layers of aluminum are used for the column and row addressing, whereas 2 layers of polysilicon are used to form the *clear* structure and the transistor *gate* (Strüder & Moser 2007).

The spectroscopic and noise performance of various prototypes of DePFET matrices with circular layout are reported by Treis et al. (2004, 2005a, 2006b,a).

An overview of the broad application range of the various DePFET types is shown, e.g., by [Strüder & Moser \(2007\)](#), [Lutz et al. \(2007a\)](#).

One special type of DePFET should be mentioned here: the “Repetitive Non Destructive Readout” (RDNR) DePFET. As the charge collected in the *internal gate* is not destroyed during the readout, the DePFET concept opens up the possibility to perform multiple readouts and therefore decrease the readout noise. This can be technically done by introducing a second *gate* structure (*external* and *internal gate*) and transferring the charge between the two *internal gates* hereby measuring the same charge over and over again. A detailed insight into these unique devices is presented, e.g., by [Wölfel \(2007\)](#). The total readout noise σ_{tot} decreases with each read procedure with

$$\sigma_{\text{tot}} = \frac{\overline{\sigma_i}}{\sqrt{N}} \quad (4.3)$$

where $\overline{\sigma_i}$ is the mean noise of the N individual measurements. For $N = 360$ measurements a total readout noise in the sub electron regime of 0.25 ENC has been measured by [Wölfel et al. \(2006\)](#). This allows the detection of single optical photons, which produces only one signal electron in the detector. The drawback of this very low-noise detection method is that the multiple samplings take more time, in this case 10 ms, thus a low count rate environment has to be ensured.

4.3 Macropixel

When developing a detector system for an X-ray satellite, one of the design goals is a good matching of the pixel and detector sizes to the point spread function and angular resolution of the optics. As the X-ray focusing optics of, e.g., *Simbol-X* has an angular resolution of 20 arcsec HPD, a larger pixel size should be chosen to prevent a high data load and aliasing effects of oversampling by an unnecessary large number of pixels and also to minimize the readout time. The actual pixel size of a DePFET can be increased by adding additional drift rings, thus forming a silicon drift detector with a DePFET as readout node. Pixel sizes with an edge length up to 1 cm are possible ([Lechner et al. 2006](#)). For the *Simbol-X* mission detectors with 128×128 pixel, each with a size of $625 \mu\text{m} \times 625 \mu\text{m}$ are foreseen. This layout allows to cover the focal plane with the optimal number of pixels to sample the expected *Simbol-X* PSF, while still be able to maintain a fill factor of 100%, minimizing the detector dead area. The current macropixel matrices fabricated for test purposes, have pixel outlines of $500 \mu\text{m}$ and are shown in Fig. 4.5.

With the help of the drift rings a radial field component is introduced, by biasing them with an increasing negative voltage from the center to the outside. Electrons generated in the depleted silicon bulk therefore migrate to the potential

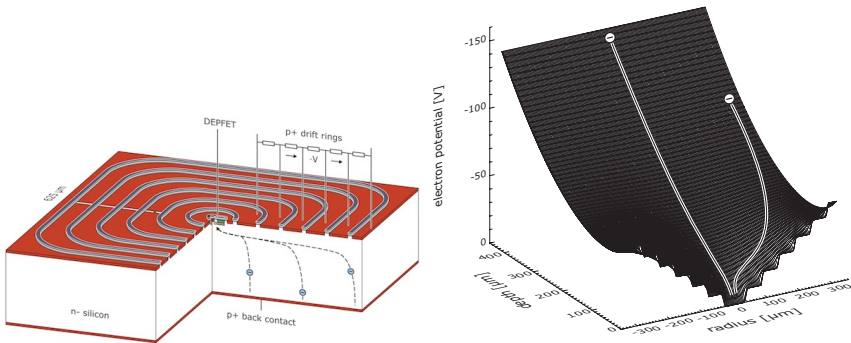


Figure 4.5: Left: Schematic of a macropixel cell, with the DePFET located in the center of the front side. The red areas correspond to the drift rings, the rounded corners facilitate gradual field changes. Right: Electron potential inside a macropixel with the minimum at the readout node (Lechner et al. 2008).

minimum of the *internal gate* (see Fig. 4.5). The field strength can be adjusted by changing the number of rings, their width, and the voltage applied to each drift ring. The drift rings can either be biased individually, or by specifying the inner and outermost voltage, and biasing the rings in between with a voltage divider. The operation principle for the DePFET, located in the center of the pixel, is the same as described in the previous Section. The readout as well as the front-end electronics of a macropixel matrix can be identical to the “simple” DePFET matrices shown in the next Section. First results on the performance of the X-type macropixel, featuring the DePFET design of the *IXO* mission are presented by Zhang et al. (2006, 2008a).

4.4 DePFET Matrices

For the usage of DePFETs as spectral imaging detectors it is necessary to build larger monolithic arrays of DePFETs. The system which is used at IAAT is built as a matrix of 64×64 pixel. Current setups at the MPI HLL and IAAT use these arrays as standard reference modules. The modular design of the control and front-end electronic ICs allows a straight forward approach to increase the array sizes. As outlined by Lechner et al. (2006) and Treis et al. (2006a), the MPI HLL is currently producing larger DePFET matrices with sizes of 128×512 and 256×256 pixel. In this Section, the connection schemes of the individual DePFETs to make up a functional detector array, including the readout procedures are presented.

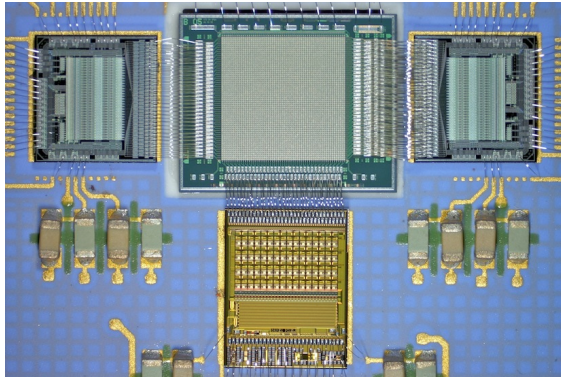


Figure 4.6: View of the hybrid. The matrix in the center has an actual outline of 4.8 mm square. The 64×64 pixel DEPMOSFET matrix is produced by the MPI HLL. Located at the center is the matrix, to the left and right are the SWITCHER II ICs (right side for *clear gate* and *gate*, left for the *clear*), below the CAMEX 64DP ASIC. All components are mounted on a ceramic carrier board (blue).

The individual front-end ASICs needed therefor are explained in greater detail in Sections 4.4.1.2 and 4.4.1.3.

4.4.1 Hybrid

In the laboratory setup the smallest exchangeable detector unit is called the Hybrid. It consists of two control ICs (SWITCHER II), the analog amplifier IC (CAMEX 64), and the DePFET matrix, which are glued on a ceramic board forming a single unit (Fig. 4.6). The ceramic board has a square hole at the center and the matrix is glued to it at the edges, such that the DePFETs can be irradiated from the front and the backside. The ceramic material is used as base due to its good thermal conductivity, as the temperature for detector operation can range from room temperature down to -120°C . The hybrid features 110 connector pins for I/O, as well as some RC-filtering circuits for the analog operation voltages.

4.4.1.1 Matrix

All of the pixels on the matrix are produced on a single die, sharing a common drain and backside contact. The unstructured backside provides a homogeneous entrance window for all pixels. For the operation of the matrix, the *external gates* of the transistors, as well as the contacts for *clear* and *clear gate* of the DePFETs are connected together row wise. The *source* contacts of each column are connected to-

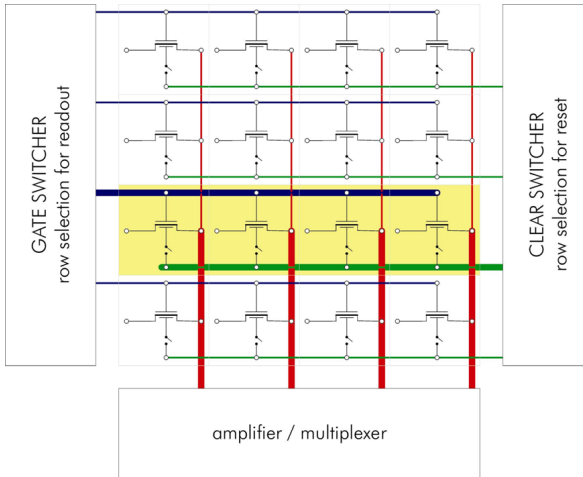


Figure 4.7: Pixel interconnection scheme for a 4×4 pixel matrix. Shown in blue and green are the row wise connection of the *gate* and *clear*, and the column wise connection of the source nodes with amplifier chip (Lutz 2005). The *clear gate* connections run parallel to the blue *gate* lines. They have been omitted for simplicity.

gether, as outlined in Fig. 4.7. For DePFET geometries where the *source* is located on the inside of the circular *external gate* the *source* contacts of individual pixels are separated by default. In the case of *drain center* matrices additional *channel separation* contact is needed to separate the *sources* of neighboring channels.

Each column has its own current source for the source follower readout, which is located in the CAMEX IC. The readout of the signal information of the matrix is done by biasing the gates of one row with V_{Gon} while leaving the other rows turned off via V_{Goff} . As only one row is turned on, the conducting channels of all other rows are closed. Therefore the measured potential of the *source* node for each column corresponds to the pixels of the active row. After applying the signals for the *clear gate* and *clear* to the pixels of this row, measuring the potential at the *source* node again gives the baseline for the signal under the premise of a complete removal of the charge from the *internal gate*. The information concerning the number of electrons accumulated in the *internal gate* is the difference between the two signal levels. After this process, the *external gate* is turned off and *gates* for the next row are turned on. The shortest possible integration time for the charge collection of a DePFET matrix is therefore determined by the number of rows and the time needed to read out one row.

4.4.1.2 CAMEX IC

A CAMEX 64 (Charge Amplifier MultipLEXer) is used as front-end IC for the analog amplification and signal shaping. It consists of a charge sensitive amplifier stage (CSA), a correlated double sampling stage (CDS), and a sample & hold stage (S&H) for each channel, which receives the pre-amplified signal via bond wires. As its name indicates it has 64 input channels which are operated in parallel.

The parallel processed signals of one row are serialized by a multiplexer stage before they are passed into the ADC. The CAMEX was originally developed in the context of particle detectors (Lutz et al. 1988), but has already been used in X-ray astronomy with great success, e.g., for the readout of the pn-CCD of *XMM-Newton* (Strüder et al. 1990, 2003).

The current source needed for the source follower readout is implemented as first stage in the CAMEX IC, in each of the 64 channels. The CAMEX 64G / 64DP are variants modified in order to meet the requirements needed for the DEPMOSFET matrix, e.g., the current source is in these cases realized as PMOSFET, operated in saturation mode.

The CAMEX is operated by a static and a shift register. With the static register the settings of the gain stage, or if available a bandwidth delimiter is controlled. The gain stage of the CAMEX 64DP consists of two gain switches $G1$ & $G2$ at the input and feedback lines of the first amplifier stage. This approach allows a broad input voltage range, as four different gain combinations can be set (see Fig. 4.11). The shift register, with a depth of 128-bit operates the dynamic switches of, e.g., the CDS-Stage and the reset switches. This register allows a flexible handling in the timing and, e.g., the number of CDS switches used. Figure 4.8 shows the different modules of one CAMEX 64DP channel.

At the beginning of a CAMEX measurement cycle the charge on the feedback capacitors of the amplifiers and the correlated double sampling (CDS) stage are reset (sequence is shown in Fig. 4.9). The voltage of the source node reflects the status of the selected DePFET pixel, with the accumulated charge in the *internal gate* since the last clear occurred. The input switch S_{in} is used to enable or disable the connection to the matrix. When the S_{in} switch is closed the voltage at the source is amplified and inverted at the first amplification stage by the ratio of C_{in}/C_{f1} . The signal sampling now takes place at the 8-fold CDS stage, for which the reset switch at the second operation amplifier $R2$ has to be in closed position. While the CDS switches $S1-S8$ are closed and opened sequentially, the switched capacitors $C1-C8$ are charged by the amplified signal voltage.

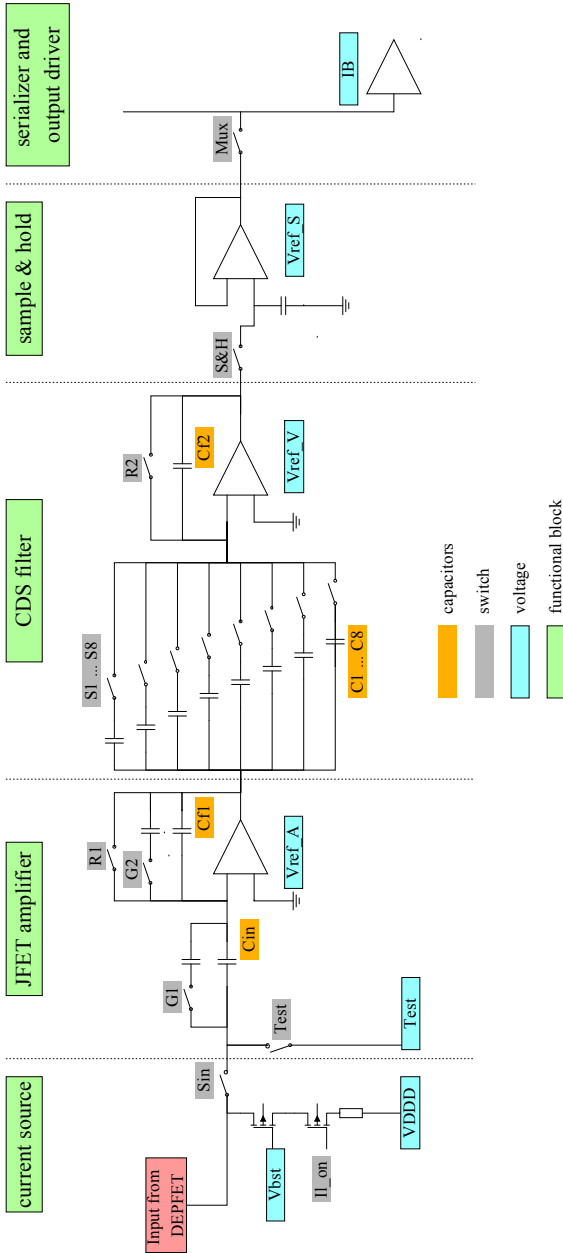


Figure 4.8: Different operation stages of one CAMEX 64DP channel. Note, the output driver drawn is the only element shared by all 64 channels. The blue voltages are input V_{DDDD} , Test, V_{Bst} , or reference voltages for the operation amplifiers. I_{L_on} is the power switch for the current source, S_{in} connects the DePFET column with the CAMEX channel, $G1$ and $G2$ are the two gain switches, $R1$ and $R2$ reset the feedback capacitors of the amplifier and filter stages, $S1 \dots S8$ are the individual CDS switches. The $S\&H$ switch stores the amplified signal in the capacitor, and MUX serializes the signal at the output driver stage.

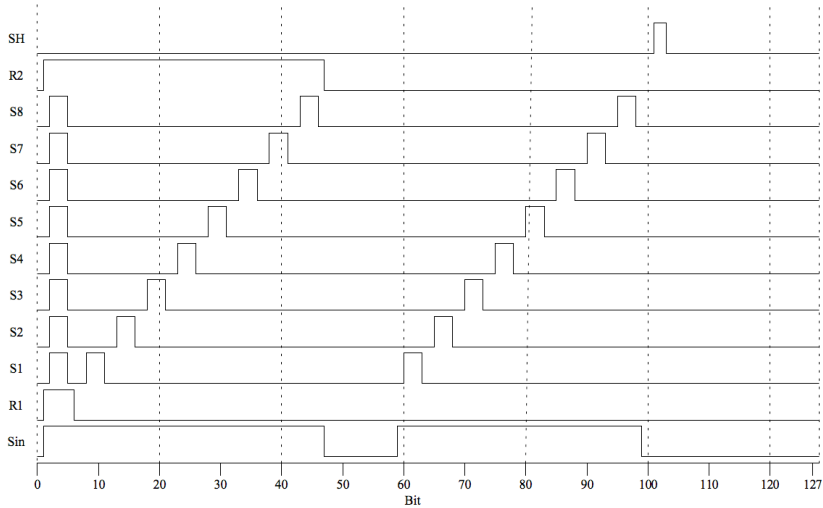


Figure 4.9: Example sequence of the CAMEX shift register content. High level: switch closed, low level: switch opened.

The *Sin* switch is then opened for the duration of the clear of the *internal gate* and closed afterwards again. Now the source voltage reflects the baseline signal of the pixel (see Fig. 4.10) with empty *internal gate*. The reset switch *R2* is now opened, the operation amplifier in the CDS stage acts therefore as an integrator. The baseline is then measured 8 times again, by closing and opening *S1–S8*. With each sampling the switched capacitors charge the feedback capacitor C_{f2} with the difference between the stored signal and the current baseline charge. As a result of the multiple samplings small fluctuations in the source voltage are averaged. Finally the voltage at the capacitor C_{f2} reflects the 8-fold averaged amplified difference between baseline and signal.

This voltage is then stored in a sample and hold stage (*S&H*) until the output multiplexer (*MUX*) serializes the signal of all 64 channels to the common output driver. For this purpose a logic “1” is written into the *MUX* shift register, and subsequently clocked through the 64 channels with the *MUXCLK*, hence selecting always one active channel to be connected to the output driver. The amplifiers are reset, and the next line can be processed. To increase the readout speed, the amplification and sampling of the DePFET row n and the readout of line $n - 1$ from the *S&H* stage are performed in parallel.

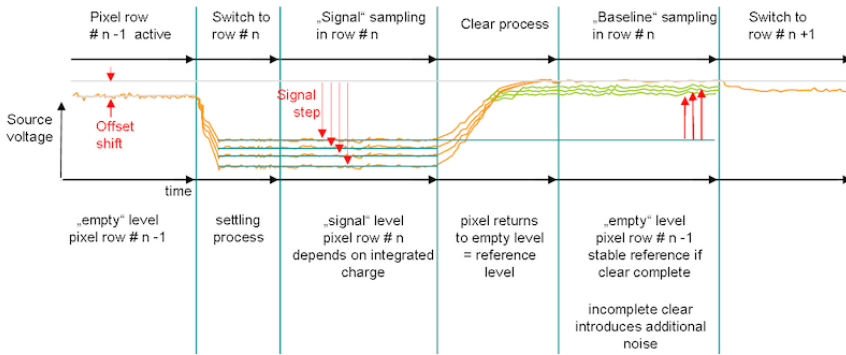


Figure 4.10: Voltage level of the source node during a CAMEX readout sequence. Starting with the turning on of the current row, followed by the signal sampling and the clear step. The baseline sampling concludes the readout of this row, before it is turned off, and the next row is turned on. The different yellow and green lines show possible signal- and baseline levels (Treis 2005).

Events occurring during the CAMEX readout process are measured with a wrong energy and are in general called “misfits”. Photons entering the detector during the signal sampling are recorded with a lower energy, as they will not see all 8 signal samplings. Photon hits during the clear process will be not recorded at all. The time between the finishing of the clear process of the *internal gate* and the beginning of baseline sampling has to be minimized because leakage current is accumulated during this period in the pixel and photon hits during this time will result in a baseline shift. The readout of the CAMEX and the pixel biasing with the SWITCHER II IC, presented in the next section, have thus to be tightly synchronized.

A *Test* input exists for each channel, such that arbitrary channels can be selected and biased with a test voltage. This allows the measurement of, e.g., the gain or the signal timing. The current source in the CAMEX can be turned on or off with the IL_{on} switch. The constant current flowing through the active pixel can be modified with the gate voltage V_{Bst} of the PMOS transistor, typical currents are in the range of $20\text{--}50\mu\text{A}$. It has to be kept in mind that the current of all 64 pixel in one row has to be provided in parallel, therefore the monitored total load current needs to be, e.g., $64 \cdot 30\mu\text{A} = 1.92\text{mA}$.

In the pn-CCDs, for which the CAMEX has been optimized in the past, the baseline sampling is made before the signal sampling. This is, as mentioned before, contrary to the operation of the DePFET devices, leading in the DePFET case to a positive signal polarity. One of the shortcomings of the CAMEX amplifiers

produced so far is that the nonlinearity of the amplification of the positive voltage branch is about one order of magnitude larger than for the negative one. Even for illumination with radioactive sources, these deviations cause distortions in the analysis of events where charge splitting has occurred, because in the current standard analysis (see Sect. 5.2.1) a linear signal amplification is assumed in the calculation of the gain, which results in an incorrect total energy value for the recombined event.

The gain and linearity curves can be measured in the laboratory. This is done with an arbitrary function generator (Agilent 33250A) which is connected to the test input of the CAMEX. A pulse function is chosen, with the pulse width adjusted such that the voltage step occurs between the signal and the baseline sampling. The current source in the CAMEX is turned off and the S_{in} switch is in a permanent open position. A symmetric scan, where the high level of the voltage pulse is varied between -310 mV to $+310$ mV is performed. The signal amplitude is reduced by a 30 dB attenuator before fed into the CAMEX. The output voltages CAMEX 64DP are then measured with an ADC (see Sect. 4.5.4 for details on the ADC). This is done for all 4 possible gain settings. Figure 4.11 shows the measured ADC values, averaged for all 64 CAMEX channels. In addition, for the measurement with the highest gain setting separate linear fits were performed for the positive and for the negative input voltage. In Fig. 4.11 the relative differences between the data and the fit are plotted. A clear difference in the residuals of the positive and the negative branch can be seen. The negative branch shows a flat course of the linearity error, which is smaller than 0.05% for input voltages less than 220 mV. The positive branch exhibits a parabolic deviation over the complete input range⁵.

In the current setup used at IAAT the time to process one line is $\approx 31 \mu\text{s}$, but achievable times down to $12 \mu\text{s}$ are reported by Treis et al. (2004). Even the $12 \mu\text{s}$ line processing time however, is above the $2 \mu\text{s}$ requirement for *Symbol-X* and *IXO*. Faster line processing times are expected with the development of the next generation of CAMEX chips, when the output buffer design is enhanced with respect to speed and bandwidth as well as an improvement of the gain linearity (Porro et al. 2006).

As a second option the development of a new analog front-end amplifier type with the name VELA (VLSI Electronics for Astronomy) is pursued by the Politecnico di Milano and the MPI HLL. The idea behind the new chip design is based on filtering theory considerations and on the fact that a direct drain current readout scheme of the DePFETs is intrinsically faster than the source follower configuration used with the CAMEX. The CDS filter approach is not the optimum solution in terms of noise performance and bandwidth for the DePFET detectors,

⁵It should be denoted that not one individual CAMEX stage is causing this non-linearity, but it is the sum of many small deviations (Hermann 2007, priv. comm.).

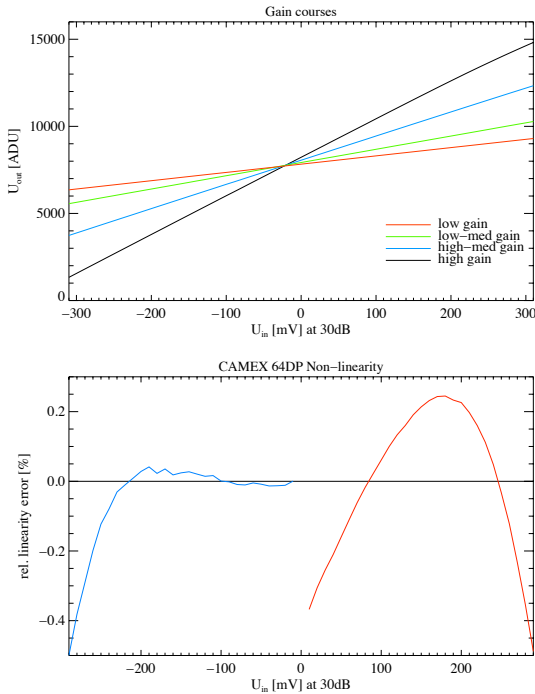


Figure 4.11: Top: Amplification of the 4 different gain settings for a CAMEX 64DP. Lower: Relative error of the highest gain setting. Drawn in blue is the negative branch (CCD) and in red the positive branch (DePFET).

as CDS works best if a triangular weighting function is approximated with the signal and baseline sampling (see Treis 2005, for a short summary). This triangular filtering stands in contrast to the DePFET operation scheme, as the clear process takes some time, thus inserting a flat top, forming a more trapezoidal shape. The VELA chip will therefore directly incorporate a trapezoidal weighting function, more details are presented by Treis et al. (2006a) and Bombelli et al. (2007). As reported by Lechner et al. (2008), the first 64 channel VELA prototypes indicate that the requirements in terms of energy and time resolution for *IXO* and *Simbol-X* are within reach. First measurements with a line processing time of $2\mu\text{s}$, result in a $\Delta E = 140\text{ eV}$ at 5.9 keV (Lechner 2009, priv. comm.).

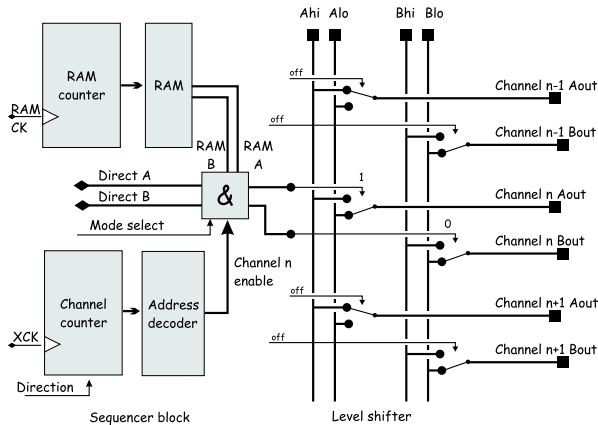


Figure 4.12: Functional drawing of the SWITCHER II IC (Treis et al. 2004). On the left side the sequencer block is shown, with the channel counter and the address decoder. With the direct pins the RAM block can be bypassed, allowing a direct selection of the active port. The level shifter connects the supply lines (A_{high} - A_{low} , B_{high} - B_{low}) with the selected active output channel, according to status of the direct pins.

4.4.1.3 Switcher II IC

For a matrix to be operated it is necessary that the voltages for the external gate, clear gate and clear are switched at the right time to the according voltage value required for the readout process. This is done by the SWITCHER II IC, which is capable of switching between two voltages with low noise and fast signal fall and rise times. The main functional parts are described below, in-depth presentations of the physical design parameters and considerations are given by Fischer et al. (2003) and Perić (2004).

A SWITCHER II IC provides 64 channels, where each channel has 2 output contacts called A_{out} & B_{out} and each contact is able to toggle between two voltages (*high* & *low*). The SWITCHERS allow a switched voltage difference up to 20 volts⁶. Such high voltages can be necessary during the clear process to ensure the removing of all charge in the *internal gate*, in order to get a reproducible baseline level. Two

⁶They are produced in the AMS high voltage CMOS technology as switching of such high voltage differences is not possible with standard CMOS technology.

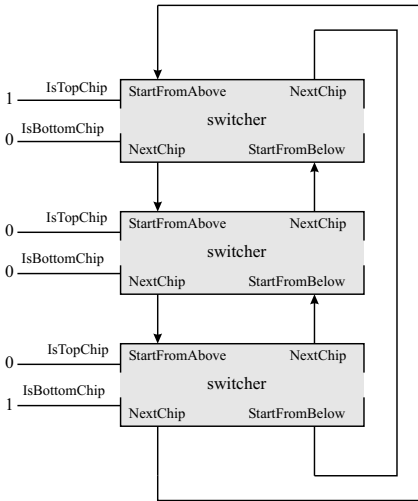


Figure 4.13: Connection scheme of a larger number of switchers (Perić 2004).

SWITCHER II IC are placed on opposing sides of the matrix, one for the *clear* voltages and one for the *gate* and *clear gate* voltages. Each SWITCHER output port is row wise connected to the corresponding bond pad on the matrix.

At the beginning of the SWITCHER II IC operation a reset signal is applied, bringing the SWITCHER II IC into the programmed startup state and the first channel is selected. An external sequencer generates the digital signals of the *gate*, *clear gate* and *clear* status, which are applied to the direct pins of the switching matrix, as shown in Fig. 4.12. The switching matrix connects the A_{high} or A_{low} voltage to the A_{out} port, and the B_{high} or B_{low} voltage to the B_{out} port. The high and low voltages of each port correspond to the on and off voltages for the *gate*, *clear gate* and *clear*. The state of the switching matrix, determining which voltage line is connected to the output port at a time, is assigned either by the content of the RAM of the SWITCHER or, as in the setup currently operated at the IAAT, by the state of the direct pins. After the readout of one row is completed, a clock signal (XCK) increments the channel counter and the next channel will be activated, as only one channel can be active at a time.

For parallel operation this state changes have to be synchronized between both SWITCHERs and the CAMEX as, e.g., the clear and clear gate signals are needed to start after the signal sampling is completed and have to be finished before the baseline sampling takes place.

The SWITCHER II ICs can be daisy chained in order to operate on larger detec-

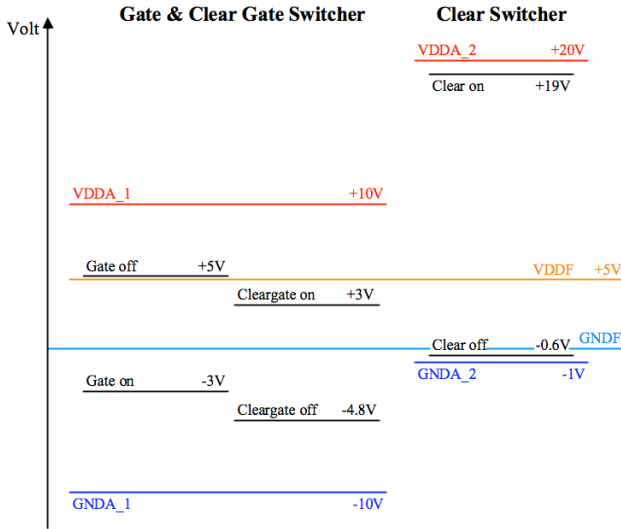


Figure 4.14: Voltage levels and switching ranges of a Switcher II IC, exemplified for Hybrid No. 42.

tors sizes than 64 rows, shown in Fig. 4.13. To ease the operation, the SWITCHER II IC generates a *NextChip* signal, after all channels have been switched. This signal can be fed into the next switcher as start signal. Depending on the shift direction (up or down) this can be connected to the *StartFromAbove* or the *StartFromBelow* pads. In case more than one SWITCHER is needed on each side of the detector, they can be configured as first chip (*IsTopChip*) or last chip (*IsBottomChip*) in the daisy chain, or in case none of the aforementioned is set, as middle chip. The setting of the shifting direction and the chip position determines the active channel directly after the startup. An alterable run direction is necessary as one chip has to be rotated by 180° as it is placed on the opposite site of the matrix, and hence has to be operated in the other direction for the selection of the same row. In the setup used, only one SWITCHER II IC on either side of the matrix exists, therefore the *NextChip* signal is fed into its own appropriate *StartFrom* pad, ensuring a cyclic, perpetual operation.

For the operation, the SWITCHER II IC needs rail voltages called VDDA and GNDA, which are the upper and lower limit of the switchable voltage range. The highest nominal voltage difference is 20 V, but a difference of 23 V was already

successfully tested (Treis 2008, priv. comm.). The switched voltages of both ports *A* & *B* must be kept within this range, under the additional constraint that the *low* voltage must be always lower than the *high* voltage of the same port (see Fig. 4.14). The supply voltage *VDDF* for the digital parts and the digital ground *GNDF* are common for both SWITCHER II ICs.

An outlook to the next SWITCHER IC generation is presented by Fischer et al. (2007), highlighting design goals and improvements over the current IC generation.

4.5 Data acquisition system

Part of the work done in the context of this thesis was the assembly and implementation of a data acquisition system at the IAAT for the operation of the above described DePFET matrices with 64×64 pixel. This was done in close collaboration with the MPI HLL, as the system presented here is based on a similar system used in the MPI HLL (Treis et al. 2004, 2005b). The purpose of this setup is to gain a deeper understanding of the underlying device physics, to study the readout procedure and the consequential requirements, in order to be able to build and test the *Simbol-X* Event-pre-processor and Sequencer at the IAAT. Furthermore pile-up and timing measurements are undertaken, necessary for the verification of the science performance simulations described in Section 6.

An overview of the components and important signal paths of the setup can be seen in Figs. 4.15 and 4.16, and details are explained in the next sections. The main building blocks of the setup are a vacuum vessel, a cooling system, a Windows PC for controlling, programming and data acquisition using two C++ applications, a cPCI-rack housing additional commercial interface cards and a set of circuit boards. The PC and the cPCI rack are coupled via an optical bridge (National Instruments MXI-4), in order to reduce electrical pickup of the system. For the same reason, the remaining components are either powered with an insulating transformer, or attached to the vacuum vessel in a non conducting way.

The detector itself is located in the vacuum vessel and is surrounded by a cooling mask which is thermally coupled to a helium cold head (Leybold 5/100T), allowing operation temperatures down to -140°C , thus making it possible to test the DePFET behavior in a broad temperature range. Inside the vacuum vessel the ceramic carrier of the detector is connected to the detector board, via a zero-insertion-force (ZIF) socket. The detector board, or “Innenplatine” provides further RC-filtering elements, an analog buffer for the outgoing detector data, and the electrical connectors to the vacuum flange. Two linear manipulators are integrated in the setup to accommodate radioactive X-ray sources, located such that the detector can be illuminated from the front and the back side. An optional third

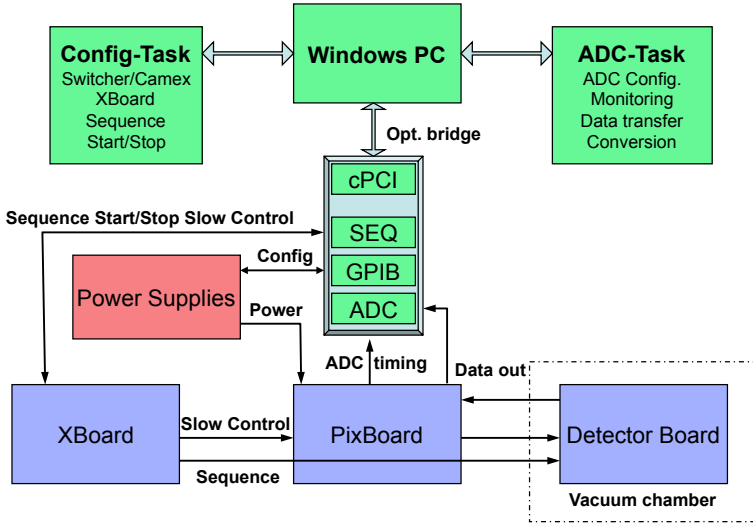


Figure 4.15: Flowchart showing the experimental setup and main data paths. Drawn in green are the control PC and the attached cPCI-rack with the interface cards. The main circuit boards are shown in blue.

manipulator allows a back illumination from a distance of either 89 mm or 199 mm and is large enough to house an ^{55}Fe and an ^{241}Am source. With these configuration possibilities the setup can be used for calibration purposes, e.g., to study effects of charge splitting for front and backside illumination, or to determine the influence of a high energy X-ray source like ^{241}Am during the calibration phase.

The vacuum vessel can be modified to host a chopper wheel in order to simulate a time variable X-ray source (see Section 4.5.6). Additional Pt100 resistors provide temperature information of the cold finger, the lower part of the cooling mask and the ceramic carrier. Pressure information is obtained with a dual vacuum gauge (Pirani and cold cathode manometers) covering the accessible pressure range from 10^3 – 10^{-8} mbar. Venting is done with a valve connected to a N_2 pressure vessel, thus ensuring a clean and dry venting of the chamber.

There is a close resemblance between the *Simbol-X* macropixels and the 64×64 pixel prototypes of the *IXO* WFI, which differ mainly in larger pixel sizes and the additional drift rings of the macropixel detector. The similar operation principle of both allows an easy knowledge transfer acquired in building process and the

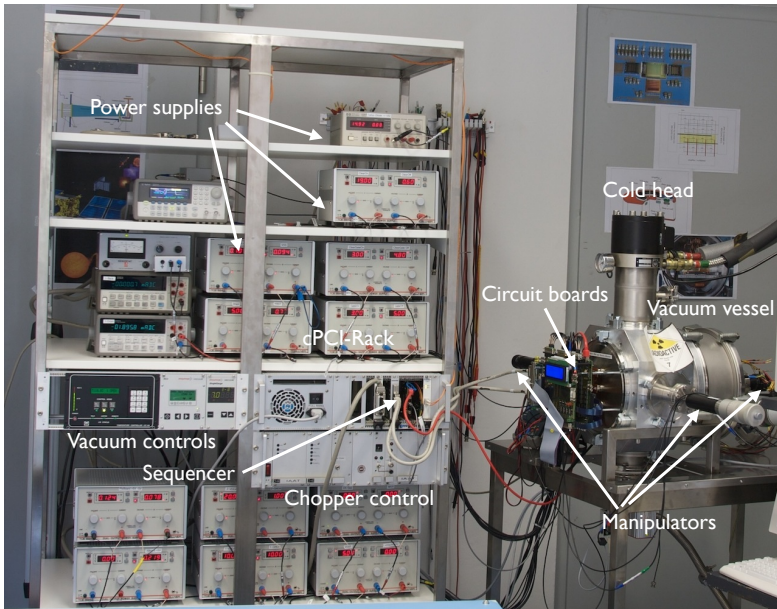


Figure 4.16: View of the laboratory setup, main elements are labeled.

operation of the current test setup. The modifications for the macropixels are mainly a different detector circuit board and cooling mask. In addition, an adaptor board is inserted between the current PixBoard and the flexlead connectors on the outside of the vacuum vessel to account for the larger number of electrical connectors and the additional supply voltages for the drift rings.

4.5.1 Sequencer

Part of the digital signals for the operation of the CAMEX and SWITCHER IC's are generated by a sequencer. These are mainly the fast clock signals and the direct port signal for the SWITCHERS. In this setup a commercial sequencer card (ADlink NuDAQ 7300) is used for pattern generation, which has 16 DO/16 DI ports available and can produce TTL patterns at a maximum speed of 20 MHz, with a limited number of lower optional frequencies.

The sequencer has also an interface based on the slow control protocol with 4 auxiliary digital input and 4 auxiliary digital output ports. This interface is used as supplementary way for command and control of the static signals, as well as for the programming of the front-end electronic IC registers. For the operation of

the matrix the patterns needed to process one line of the detector are written into one of the four 16k FIFOs. This sequence then runs in an endless loop, until the user stops the pattern generator. The pattern length should of course not exceed the 16k FIFO size. To prevent FIFO underflows, which cause artificial breaks of not clearly predictable length, two or more sequences can be linked together sequentially, under the premise that no time glitch is introduced.

A list containing the fast signals of the sequencer is given in Table 4.1.

Table 4.1: TTL output signals of the AdLink sequencer card. The “occur.” column indicates typical occurrence numbers of this signal during the readout of one line and not the length of the signal. The destination column denotes the final receiver of the signal.

Signal name	occur.	destination	purpose
ADC Gate	64	ADC	Storage of ADC value
Gate	1	Switcher 1	Direct input port signal
Clear gate	1	Switcher 1	— " —
Clear	1	Switcher 2	— " —
MUXIN	1	CAMEX	Enabling of the MUX switch
MUXCLK	64	CAMEX	Clock of MUX register
SCLK	128	CAMEX	Clock of shift register
XCK	1	Switchers	Counter Block Clock
RAMCK 1/2	-	Switchers	Clock of Switcher RAM (unused)
Line	1	ADC	Triggers line turn keyword
Hold	0	XBoard	Position of integration time in sequence
GPTrig	arb.	PixBoard	General purpose trigger for external devices

4.5.2 XBoard

The sequencer card is connected to the “Xilinx-Board” (XBoard), a digital interface card, housing a Xilinx Spartan II FPGA was developed by the HLL. The XBoard is necessary to overcome several limitations imposed by the sequencer on the operation of the DePFET-matrices. First of all the sequencer card has not enough output ports to generate all digital signals needed to address the detector directly. Furthermore, the limited number of usable operating speeds of the sequencer restricts the available readout speed of the detector. The FPGA on the XBoard allows a more flexible usage of the setup.

The XBoard determines the operation frequency of the DePFET matrix and the readout electronics. It can either be clocked with a programmable clock generator (Cypress PLL) or by an external input. Currently the PLL provides the 33 MHz base clock. A clock divider, which can be set from the standard user interface, allows the fast and easy change of the clock frequency, without reprogramming the PLL. The standard clock frequency used for the measurements presented in Chapter 5 was 16.6 MHz. This flexibility allows the XBoard to be operated at arbitrary frequencies under the restriction of maximum 20 MHz clock frequency imposed by the sequencer. The output pattern of the sequencer FIFO is stored on the XBoard in a FIFO, and both FIFOs communicate over a handshaked bus. The speed limit arises from the fact that when the XBoard FIFO is clocked faster than the maximum frequency of the sequencer FIFO unpredictable long breaks in the sequence are inserted during the refilling of the XBoard FIFO.

The readout scheme can be paused at an arbitrary position within the processing of a line, marked in the pattern sequence with “hold”. The duration of the hold can be set within the commanding routine with the “halt delay” of the order of \sim ns–ms, introducing an artificial integration time. Special readout options for diagnostic purposes, like single pixel or single line readout, are implemented in the FPGA and the commanding software, but have not been subject to detailed testing at the IAAT so far.

The FPGA has an interface implemented for the slow control protocol of the sequencer. The FPGA generates and addresses signals for the configuration of the matrix readout electronics and for the generation of static operation signals from the received slow control data. This includes the programming of the SWITCHER II IC configuration block from the slow control data, as well as the programming of both CAMEX registers, static and shift. Furthermore the ADC Gate and ADC clock signals are generated as well as the creation of the line trigger keyword, indicating the complete readout of one line to the ADC. These additionally generated signals are then resynchronized to the local XBoard clock with the pattern generated by the sequencer in the XBoard FIFO.

4.5.3 PixBoard

The purpose of the PixBoard is to collect all digital and analog signals, input and output, before they are transferred into and out from the vacuum vessel via flexlead connectors.

The digital signals coming out from XBoard are galvanically decoupled by a set of optocouplers on the PixBoard before being redistributed to the respective sockets of the flexleads.

The various voltages needed to operate the DEPMOSFET matrix are produced

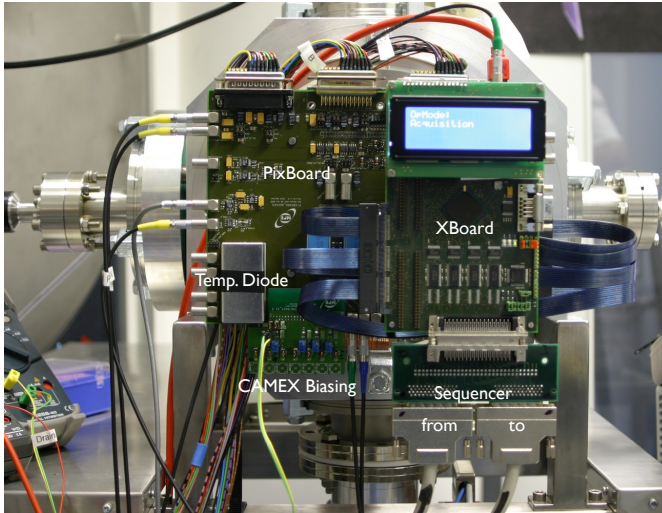


Figure 4.17: XBoard (right-hand side foreground) and PixBoard mounted on the front side of the vacuum vessel. The two SCSI cables connect the XBoard with the sequencer. On the left side the metallic enclosure of the control electronics of temperature diode can be seen, as well as the “biasing circuit board” which generates the CAMEX currents. On top of the PixBoard, the input of the operating voltages for the matrix can be seen.

by external power supplies and fed into the PixBoard. Here filter circuits are present and for selected signals, e.g. the SWITCHER voltages for V_{Gon} , V_{Goff} , V_{CGon} , V_{CGoff} , V_{Con} and V_{Coff} , or the CAMEX V_{Bst} , the polarity can be changed if necessary.

The PixBoard provides connectors for several monitoring signals, such that a correct operation of the detector can be ensured. Single ended and differential output buffers for the analog CAMEX output signal exist, allowing an instant monitoring of the DEPMOSFET output on an oscilloscope. In addition LVDS signals for the ADC operation (gate, clock, line, and frame) are generated from the digital XBoard data stream on the PixBoard.

The Op-Amp biasing currents for the different CAMEX stages (V_{refV} , V_{refS} , V_{refA} , I_B) and voltages (V_{DD}) can be either externally supplied or set via adjustable voltage dividers from the two main CAMEX voltages (V_{SS} , V_{DD}). This biasing is done on an additional circuit board clipped to the PixBoard, shown in Fig. 4.17.

A circuit for the current source needed for the temperature diode on the DePFET matrix die is present, as well as a protection circuit for the switcher power supply,

which ensures the correct operating range of the switched voltages within the VDDA and GNDA limits.

4.5.4 ADC

The ADC-Board Version 2 is located in the cPCI-Rack where it is mounted piggy back on a commercially available cPCI-carrier board (SIS1100-cCMC). The carrier board consists of a PCI bridge IC and of a Spartan II FPGA for data formatting and output control.

The analog to digital conversion is done by a 14-bit ADC (AD9245) which has a maximum digitalization speed of 80 mega samples per second. The effective resolution of the ADC is reduced, due to the piggy back mounting on the carrier board and was measured to be 11.7 bit (Treis et al. 2004). The operation speed of the ADC is limited by the fact that no memory for the storage of the converted data is available on the ADC card. It can therefore not be operated with a speed faster than the 33 MHz of the carrier board PCI bus connection.

The ADC-Card features two separate ADC pipelines, where only one is used at the moment, since the 64×64 Hybrids feature only one CAMEX readout node. The analog data originating from the detector are transferred via the PixBoard to one of the differential inputs of the ADC. In front of the ADC IC a DAC is implemented which gives the possibility to offset the detector signal, in order to make use of the ADC complete dynamic range. The usable input voltage range of the ADC is about 2 V, a mean noise of 1.8 ADU was measured in the setup.

For the correct signal sampling, timing information is transferred from the XBoard via the PixBoard to the ADC card as well. These signals are the ADC-clock, ADC gate, ADC-init and ADC-frame. The ADC-clock is then used as the ADC conversion clock, whose delay can be adjusted for an optimal sample timing. The ADC gate signal is used to acquire the ADC values from the continuous ADC data stream, when the pixel signal is digitized. In the FPGA, the ADC-init signal is used to insert formatted keywords for the line and frame to ensure the correct signal timing of the ADC output. These keywords are checked later on for consistency by the software which converts the raw data to the standardized frames format to identify corrupted frames. From the FPGA the data are then written with DMA (direct memory access) to the memory of the control PC.

For a detailed offline analysis all raw data information is stored on the hard disk of the control PC. As there is no built-in data reduction, the 32-bit data of each pixel amounts to a data rate of 32 Bit·4096 Pixel·500 fps \sim 490 Mbyte/min. This rate is well below the 132 MByte/sec transfer limit of the 32-Bit 33 MHz PCI-Bus system. As a result of this huge raw data rate the useful observation time is limited to a few minutes, as vast files (\sim Gbyte) are created.

4.5.5 Power supplies

Commercially available low-noise power supplies from Toellner are used to power the setup. They can be remotely controlled via a GPIB interface housed in the cPCI rack. A software application commands a power up sequence for the voltages to ensure a proper function of the ICs.

4.5.6 Chopper wheel

In addition to the standard measurement modes (full detector illumination from the front and the backside), it is possible to install a chopper wheel in the vacuum vessel, in order to simulate a time variable X-ray source. The mount housing the radioactive source, designed for an ^{55}Fe pellet with an active window diameter of 12 mm, is located at a distance of 35 mm from the DePFET surface. A slider which can be operated with a linear manipulator is used to shield the detector from the source and provides an illumination hole with a 6 mm diameter. In addition an aluminum block with 1, 2, and 3 mm diameter holes is screwed to the slider acting as a collimator. The distance between the lower end of the collimator and the detector is 5.5 mm. The chopper device consists of the engine, realized as a small multiphase motor from Clifton, and a spoked shutter wheel with holes on the outer rim screwed onto the driving axle of the motor. The chopper wheel is mounted onto the copper cooling mask with an thermal insulating adapter, and illuminates the homogenous backside of the detector as shown in Fig. 4.18.

An infrared photoelectric barrier is used to monitor the proper operation of the chopper wheel. It can therefore be used to measure the pulse period of the rotating wheel, or in the case of a halted wheel to check whether the radioactive source is covered by the wheel or in an open position with respect to the detector. The open position allows a constant back illumination of the detector even with the chopper wheel mounted. As the DePFET matrix has no optical shielding on the entrance window, it is sensitive to infrared photons, thus stray light from the light barrier saturates the pixels. During measurements the light barrier has therefore to be switched off.

The steering electronic box is located outside of the vacuum chamber in the laboratory rack. The electronic box issues voltage pulses to the multiphase motor. Each voltage pulse results in a 90° rotation of the drive axle. It is possible to manually issue the pulses, e.g., to set the wheel to a certain position as explained above. For the rotation speeds of the drive axle 9 different presets can be selected. Of these 9 presets not all result in a useful, constant rotation period. The settings of 1-3 are usually too slow to operate the chopper as the 90° steps of the axle are too rough to form a regular pulse period, which leads to large deviations from the expected period. In the settings 8-9 the voltage pulses which drive the step motor

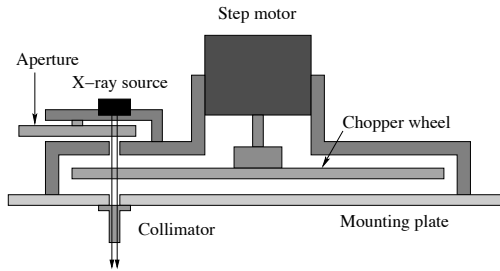
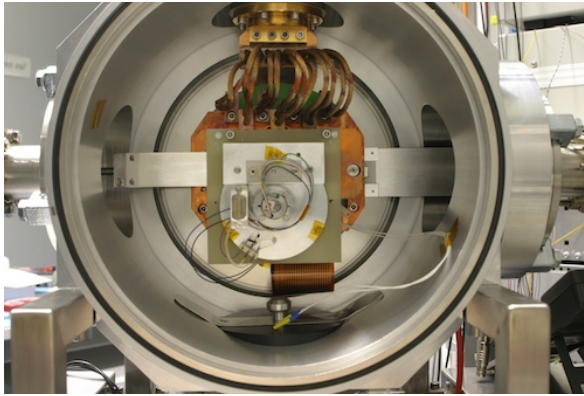


Figure 4.18: Top: The chopper wheel mounted onto the surface of the cooling mask. Also visible are the copper braids between the cold head and the cooling mask. The linear manipulator on the left side operates the slider for the chopper wheel source, the one on the right-hand side is for the coverage of the front illumination source. Bottom: Schematic view of the chopper wheel.

are too short to overcome the inertia of spoked wheel mounted to the driving axle during the gradual spin up at the start, resulting in no rotation at all.

To produce longer pulse periods a second multiphase motor with a transmission gear has been used. Through the usage of two different spoked wheels, in combination with both motors, periods from $640\mu\text{s}$ up to 911ms can be obtained (see Table 4.2). The first shutter wheel has 16 equally spaced holes each with diameter of 4 mm, centered at a radius of 25 mm, thus reaching a duty cycle of 33%. The second shutter wheel has 4 elongated holes at a radius of 25 mm with a width of 4 mm, covering an angle of 45° and thus reaching a duty cycle of 48%. Both shutter wheels are illustrated in Fig. 4.19.

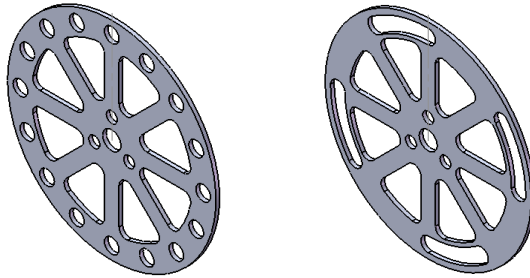


Figure 4.19: Shutter wheels with 16 and 4 holes. They are centered on a circle with a 25 mm radius. (Image courtesy of K. Lehmann)

Table 4.2: Possible chopper wheel configurations with the resulting period and deviations, obtained by measurements with the light barrier.

motor	wheel	setting	mean period [ms]	std. dev. [μ s]	rel. dev. [%]
large	4	5	911.45	4290.0	0.47
large	4	6	455.45	695.0	0.15
large	4	7	227.78	377.0	0.17
large	16	5	227.50	3300.0	1.45
large	16	6	113.86	395.0	0.35
large	16	7	56.96	225.0	0.40
small	4	4	20.47	62.0	0.30
small	4	5	10.24	20.5	0.20
small	4	6	5.12	8.0	0.16
small	4	7	2.56	2.9	0.11
small	16	3	10.25	156.7	1.53
small	16	4	5.12	21.2	0.41
small	16	5	2.56	5.72	0.22
small	16	6	1.28	2.75	0.21
small	16	7	0.640	1.44	0.23

CHAPTER 5

Measurements

“There are two possible outcomes: if the result confirms the hypothesis, then you’ve made a measurement. If the result is contrary to the hypothesis, then you’ve made a discovery.”

[Enrico Fermi]

In this Chapter, measurements taken at IAAT with the laboratory setup described in Section 4.5 are presented. The focus of the measurements is to get an idea of the actual detector performance. First, the principal operation parameters are given for the hybrid used in the laboratory setup. In Section 5.2, the data acquisition itself is explained and an introduction to the data reduction and analysis is given. Thereafter, results obtained with Hybrid 42 are discussed, with focus on energy resolution and charge splitting. In Section 5.2.5, temperature measurements of the detector noise and the temperature stability of the offset and gain are presented. This Chapter then finishes with some remarks to “clear-correlations”, a detector feature related to the clear process of the DePFET.

5.1 General remarks

All measurements presented in the following section were taken with Hybrid 42, a source-center cut-gate P0 double-metal matrix from the PXD05 production run (geometric details in Sect. 4.2.2). The measurements were usually taken at a temperature of $\sim -50^{\circ}\text{C}$, with the operating voltages and currents as listed in Table 5.1. Deviations from these values are stated explicitly in the description of the measurements.

The maximal possible XBoard clock frequency for the stable operation of the setup is 16.5 MHz, leading, together with the pattern length programmed into the Adlink sequencer, to a processing time for one line of $32.625\ \mu\text{s}$. During this

Table 5.1: Typical operation voltages and currents for Hybrid 42

Type	Value	Type	Value
V_{Gon}	-3.0 V	V_{back}	-140 V
V_{Goff}	+5.0 V	I_{back}	$0.3 \mu\text{A}$
V_{CGon}	+3.0 V	I_{load}	1.92 mA
V_{CGoff}	-4.8 V		
V_{Con}	+19.0 V		
V_{Coff}	-0.3 V		

period of time the CAMEX has to perform the signal and baseline sampling (see Sect. 4.4.1.2) and the charge collected in the pixels has to be removed between the two samplings. For the 64×64 pixel matrix this line processing time results in a frame time of 2.088 ms. The CAMEX was set up such that the CDS filter and the output multiplexer were operating in parallel, and the highest gain setting was chosen. The duration of the clear process, as given by the time the voltage V_{CGon} is applied, was $1.2 \mu\text{s}$ corresponding to 20 XBoard clock cycles.

5.2 Standard measurements

A standard measurement is usually started by taking “dark” frames, where the detector is not illuminated with photons from a radioactive source. These “dark” frames are needed for calibration purposes, e.g., calculation of the offset, estimation of the detector noise, and detection of defect or oddly behaving pixels. Typically 500–1000 dark frames are taken before the radioactive source is uncovered and the detector is illuminated. The raw data stream, i.e., the pulse height amplitude (PHA) of each pixel, originating from the ADC is saved to the hard disk. This raw data file is converted into a “Frames”-file, where data belonging to one readout cycle of the detector are grouped together. Hereby the frame consistency is checked with the line and frame turn keywords inserted by the ADC. After a successful verification the “Frames”-files are then further processed with the Halbleiterlabor Standard Analysis Software (HLLSAS) and custom made IDL-scripts used for special analysis tasks. The next section gives a brief summary of the essential analysis steps and follows hereby the different processing stages of the HLLSAS, necessary for the understanding and the interpretation of the collected data. A detailed description of the HLLSAS and the implemented algorithms can be found in the included documentation or in the review given by Treis (2005).

5.2.1 HLLSAS Analysis

As first step the offset is evaluated from the dark frames. The offset for an imaging detector is generally defined as the in average recorded digitalized detector output signal in the absence of photons on the detector. This offset value is usually the sum of different components, e.g., the integrated leakage current of each pixel and pedestals originating from the front-end and readout electronics. The offset is calculated as the mean value of each pixel from the dark frames and is stored in the offset map. As shown in Fig. 5.1 it is dominated by the column structure of the CAMEX IC. After subtracting the mean column offset, the residual offset distribution, the true pixel to pixel variation of the matrix, becomes visible. As can be seen in Fig. 5.1 Hybrid 42 shows a smooth and flat residual offset distribution.

The noise, defined as the standard deviation σ_N of the offset values, is then calculated in PHA units and stored in the noise map. With the help of the noise and offset map mask files are generated. In these mask files “noisy” or “bright” pixels are excluded from further analysis. A pixel is considered “noisy”, if its noise value σ_N is above a certain threshold, calculated as a multiple of the detector mean noise (e.g., $5\times$). A “bright” pixel is identified by searching the residual offset map for pixels with a large deviation from the mean detector value. In the mask file, an additional region-of interest (ROI) can be specified, in order to in- or exclude certain regions of the detector in the data analysis.

From each frame the offset map is subtracted and afterwards the mask file is applied to the frame. All pixels whose offset-corrected pulse height amplitudes now exceed the primary event threshold, are marked as “event”. The primary event threshold (PETH) is given as a multiple of the individual pixel noise value and is typically chosen in the range of 5 to $8\sigma_N$. As the charge cloud generated by a photon can be distributed over several pixels, it can create a split event. In order to identify low energy split partners in the surrounding pixels of a primary event, a lower secondary event threshold (SETH) is applied in the search. The secondary event threshold is also given in multiples of the noise value and is set to typically 2.5 to $3\sigma_N$. This event detecting method based on two different thresholds can easily be turned off by setting both thresholds to the same value.

After the events of one frame have been identified, a row-wise common mode correction is made. The common mode has its origin in small fluctuations of the CAMEX supply voltages. Because of the strong CAMEX amplification, these small voltage differences lead to variations of the output signal. As one row is processed in parallel by the CAMEX all pixels in this row are equally affected. The common mode is corrected by calculating the mean PHA value of all pixels in the current row which are not marked as an event. Alternatively the common mode can be calculated as the median PHA value of all pixels in the row, excluding the

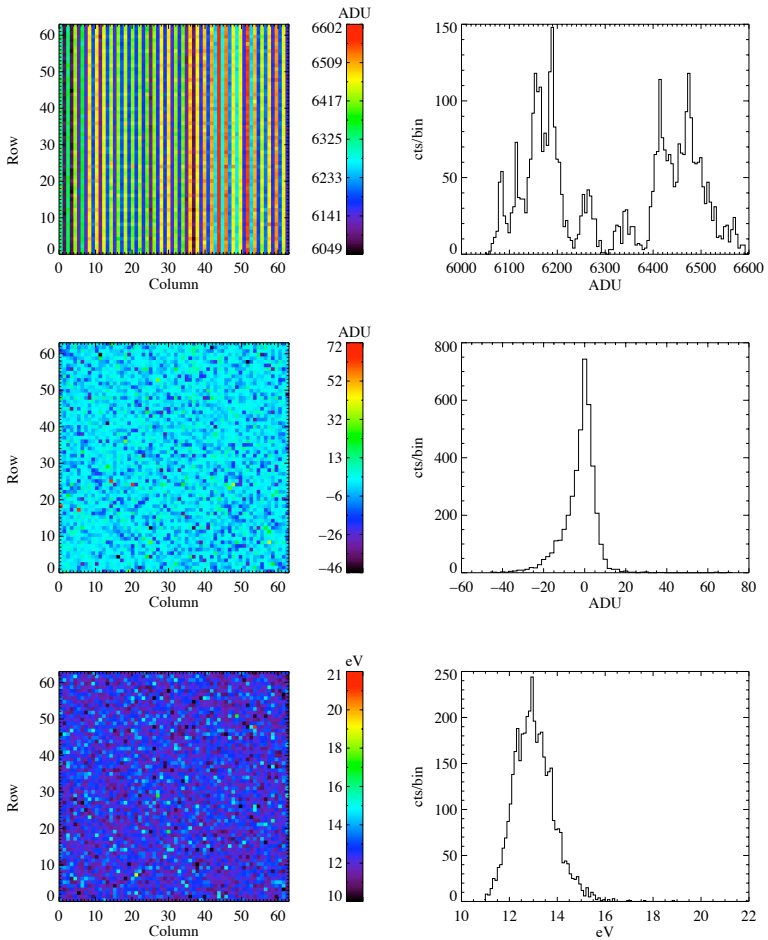


Figure 5.1: Top panel shows the CAMEX dominated offset map. Middle: residual offset map, showing the remaining offset distribution of the detector, after the CAMEX dominated mean offsets of the columns have been subtracted. Bottom: calibrated noise map of the detector, showing a mean noise of ~ 13.7 eV.

pixels flagged as “noisy” or “bright”. The common mode value is then subtracted from the events in that row, giving the common mode corrected PHA values of the events.

All recognized events are written into an event list, which is then further processed by the pattern recognition algorithm. In this algorithm the events of one frame are examined for events in adjacent pixels which form a pattern. These patterns, caused by split events or by per chance coincidences of individual photons, are classified by the number of pixels involved and whether a valid or invalid pattern was formed. For details on the classification and the valid types of pattern see Section 6. Depending on the number of pixels involved they are declared as single, double, triple, or quadruple event.

As next step, the energy response of the detector is calibrated. Therefore, a conversion factor between the recorded PHA channel and the corresponding photon energy has to be determined from the single events spectra. If the detector has been illuminated with a radioactive source, one or more lines are visible in the PHA spectra. By fitting a Gaussian profile to the recorded line and determining the center value of the fit, a conversion factor (PHA \rightarrow eV), also called gain value, can be estimated under the premise that the line energy is known. These gain values are calculated for each pixel and are stored in the gain map. With the gain value the energy for each event can be determined. For split events, the total energy can be calculated as the sum of the individual pixel energies. Note that this addition is not possible for the PHA channels, as the pixels can have different gain values.

The HLLSAS does only take single events into account for the gain calculations, since in this case the complete photon energy has been deposited into one pixel. For larger patterns the complete charge has to be reconstructed from different pixels within the pattern, each having a different offset, noise and gain value. Furthermore, uncertainties from the nonlinearity of the CAMEX can be minimized by not taking split events into account when the gain is calculated. It has therefore to be ensured that enough single events are recorded during the measurement in order to be able to perform the line fitting. If this is not possible, a gain map from a different measurement can be used for the energy calibration, under the prerequisite that the operating conditions were comparable, e.g., operating temperature, readout time, CAMEX operation mode, and DePFET biasing.

With the values of gain map, the noise map is then converted from PHA-channels to eV. The calibrated noise map shown in Fig. 5.1, with a mean noise value of 13.7 eV, was obtained with Hybrid 42 under the operating conditions stated in Sect. 5.1. With the energy spectra of the single events, line fitting is done in order to determine the energy resolution of the detector. The split ratios of the double distribution is plotted as diagnostic tool to search for asymmetries or position dependent charge loss (see Fig. 5.5).

The information gathered by the HLLSAS is stored in the “FITS” format. One of the main output files in which information of the analysis is gathered, is the “basic.fits” file. In this file several extensions to store data sets like, e.g., the

generated maps, and a complete event list of all recognized and corrected events, are implemented. The custom scripts make mainly use of the `basic.fits`, by extracting and processing the required information. In order to reconstruct the photon energy the individual energies of a split event have to be added up. The current version of the HLLSAS does not store the correct total energy value of a pattern in the `basic.fits` file. Therefore one of the first tasks of the custom scripts is to correct for this error, before any other analysis can be undertaken. To these individual tasks done by the custom analysis scripts, belong routines to make spectral plots of the different event types in free eligible energy bands, line fitting, the analysis of the split ratios, the search for clear correlations, and tools to inspect ROI in the data.

5.2.2 Front-/Back illumination measurements

In the laboratory setup, the detector can be illuminated from two sides. Illumination through the unstructured backside, where the homogenous p^+ -doping exists, is called back illumination, in contrast to the front illumination through the structured readout side. The front illumination measurements are needed for the evaluation of the devices and as a mean to obtain calibration data needed for the backside measurements¹. This is necessary as for the backside illumination not enough single events exist in a data set in order for the HLLSAS to perform the gain calibration. Therefore, for each parameter set studied under back illumination, usually a corresponding front illumination is made.

Most measurements are made with a radioactive ^{55}Fe source which emits X-ray photons. The source decays via electron capture



and can emit a Mn K_α line at 5.9 keV and a Mn K_β line at 6.49 keV. The depth² at which the intensity of a beam of 6 keV photons in silicon has dropped to $1/e$ is about $30\ \mu\text{m}$. This means for the DePFET detector with a thickness of $450\ \mu\text{m}$, that for the front illumination the interaction takes place close to the *internal gate*, whereas for the back illumination the charge cloud has to traverse nearly the complete detector thickness. The charge cloud disperses during the drift time due to diffusion and repulsive Coulomb force, as shown in Section 3.2.2. The increased charged cloud size of a back illumination causes more split events in the detector than in case of front illumination. The valid pattern distribution for an ^{55}Fe illumination as measured for the energy between 5–7 keV and with both thresholds, PETH and SETH, set to 5σ is given with:

¹ In space, only the backside illumination is possible, since the DePFET matrix will be used together with a high energy detector in a stacked geometry.

² calculated with data from http://henke.lbl.gov/optical_constants/atten2.html

Type	Singles	Doubles	Triples	Quadr.
Front Illum.	63%	27%	3%	7%
Back Illum.	12%	46%	18%	24%

The ratios are expressed in terms relative to the total number of valid events. For back illumination the number of single events is strongly decreased, which can also be seen in Fig. 5.3 for the energy range 0.1–8.0 keV. The actual pattern distribution depends on the chosen energy band and on the threshold levels during the analysis, since for smaller SETH values the number of detected split events increases.

To determine the energy resolution of the detector, the single event spectrum is evaluated. The HLLSAS uses 5 Gaussians for the fit, one for either Mn K_α and Mn K_β lines and one for their shoulders, plus one broad Gaussian to model the background under the lines. The custom IDL script makes use of the flexible fitting routine `mpfitfun.pro` provided by the `astrolib` package. The fitting of the K_α - and K_β line is done with 2 Gaussians as well, but none of the additional Gaussians is used. The typically achieved energy resolution obtained with the HLLSAS in terms of FWHM values of the Mn K_α -line are $\Delta E_{\text{FWHM}} \approx 127.6\text{eV}$ for the front and $\approx 132.8\text{eV}$ for the back illumination. Compared to the results of the custom fit routine ($\Delta E_{\text{FWHM}} \approx 128.2\text{eV}$ and $\approx 133.8\text{eV}$), no significant differences in terms of energy resolution between the two methods used can be observed. Figure 5.2 shows the single event spectra and the results of the line fitting.

The recorded energy resolution can be expressed in terms of equivalent noise charge, giving the number of electrons in the detector needed to obtain that resolution, after subtracting the theoretically achievable limit, the Fano noise. For this measurement this corresponds to a noise value of $5.6\text{e}^- \text{ENC}$ for the front illumination. Further measurements dealing in depth with the noise and spectroscopic performance is given by Treis et al. (2006b).

Figure 5.2 shows the single event spectrum for a typical measurement. Visible besides the two manganese lines are the noise peak on the left, low energy, side and the silicon escape peak at 4.17 keV. The escape peak can be fitted with a Gaussian+Offset, in order to determine the FWHM and the intensity. To cross check the model of the detector response used in the simulation of the laboratory setup, as presented in Section 6, the relative intensity of the Mn K_α : Mn K_β line is measured with $\sim 7.6 : 1$. For the backside measurement a 0.57% probability of Mn K_α photons to be detected in the silicon escape peak is found. The events in the “bathtub” between the noise and the Mn K_α line are background and partial events. Partial events are created if the photon interaction has taken place close to or in p^+ -doped regions on the front or the back side and therefore a part of the electron

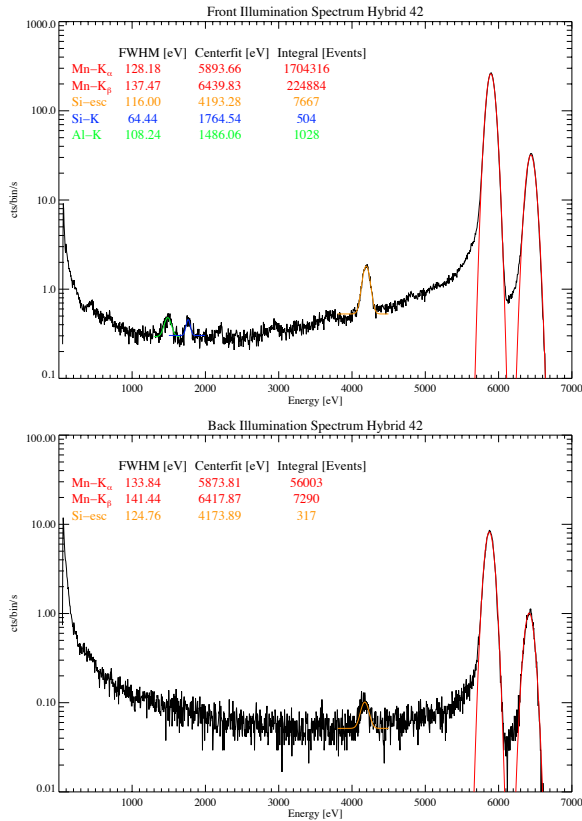


Figure 5.2: Spectrum from the single events for a front (top) and a back illumination (bottom), plotted with a binsize of 5 eV. The energy resolution of 128.2 eV and 133.8 eV FWHM was obtained at a temperature of -50°C . The integral value gives the number of events under the Gaussian shaped fit curve, resulting in a relative intensity of the Mn K lines of 7.6 : 1.

charge cloud recombines in the p-layer. In the front illumination measurement two additional lines in the “bathtub” can be identified. One is the Al K α line at 1.48 keV, having its origin in the aluminum layer of the connection interface, the second identifiable line is the Si K α line at 1.74 keV.

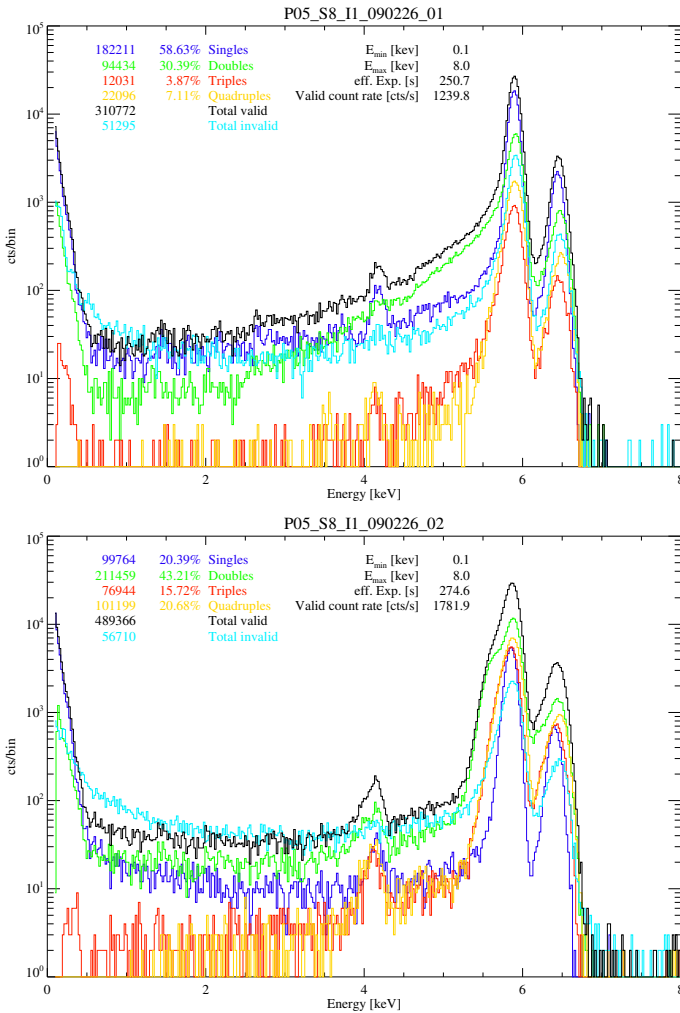


Figure 5.3: The plot shows the different pattern spectra for a front (top) and back illumination (bottom). The charge loss of the double events is clearly visible. Triple and quadruple events are affected by the charge loss as well, but due to their composition out of 3–4 split partners to a lesser extent than the double events.

5.2.3 Spectral analysis

As explained in Section 4.2.2 the source center matrices of the production run PXD04 had problems with the charge collection in the region of the clear gate. In order to minimize the charge loss it was tried with Hybrid 42 to modify the potentials underneath the clear and clear gate region by moving the contact hole of the clear gate to the crest of the structure.

The individual spectra of the different pattern distributions are shown in Fig. 5.3 for a front and a back illumination obtained with the operating voltages tabulated in Table 5.1. For all patterns the two Mn K lines are visible, as well as the silicon escape peak and on the left hand side of the figure the rise to the noise peak. The single event spectra exhibits normal behavior as seen in the previous section, but a closer inspection of the double event spectra (green lines) reveals distortions in the line shape. For the front illumination, charge loss in the double events is leading to a power-law shaped decrease of the count rate down to energies of 2 keV. For the back illumination, a strong shoulder component on Mn K lines is visible for the double events and to a lesser extent also in the triple and quadruple event spectra.

These distortions in the double event distribution indicate that charge loss is still an issue even with the modified geometry of the source center matrices. One explanation of the spectral shape of the Mn K lines could be the existence of a parasitic potential minimum underneath the clear gate area between the internal gate and the clear contact, created by the voltage V_{CGoff} . In this potential minimum, charge can be trapped thus not reaching the internal gate and is directly transferred into the clear contact during the clear process. This charge does not contribute to the signal and is missing in the measured line energy. To prevent the formation of this minimum or at least to minimize the charge loss, the correct biasing of the clear region during the integration time is essential.

As this minimum is formed during charge collection time, the two main voltages which influence the potential underneath the clear structure are the V_{Coff} and V_{CGoff} . The V_{Coff} was set as negative as possible in order to minimize the parasitic potential minimum under the clear gate contact. When V_{Coff} gets too negative, charge is injected into the internal gate and more and more invalid pixels are identified by the HLLSAS. For these pixels the offset shows larger deviations from the mean offset. Therefore the V_{Coff} was adjusted to a value close to but not above this threshold, typically to a value of -0.3 V.

When the clear gate voltage V_{CGoff} was lowered from -4.8 V down to -4 V and V_{Coff} was adjusted, the transformation of the shoulder into a second peak at 5.4 keV in the double event spectrum of the back illumination was observed. In the front illumination a steepening of the power-law in the double event distribution was observed. This indicates that the potential minimum is increased, since the V_{CGoff}

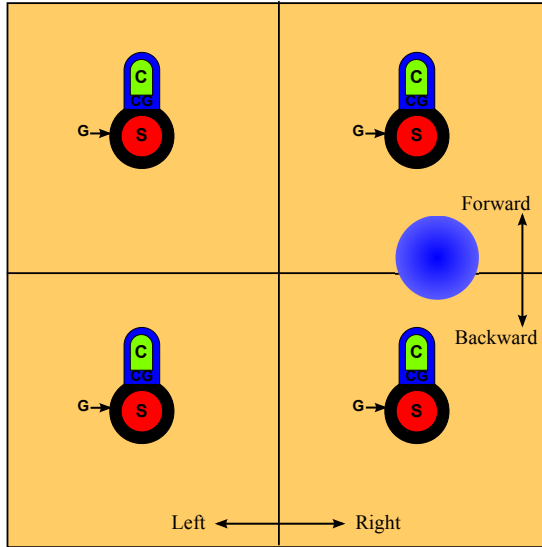


Figure 5.4: Approximate layout of a 2×2 matrix. The black circle represents the external gate of the DePFET, the blue-green region is the clear gate - clear structure. The blue circle represents the 1σ -diameter of a charge cloud.

cannot create a sufficient hole inversion layer under the clear gate.

If on the other hand V_{CGoff} was increased to values up to -5.4 V a rise of the backside current I_{Back} to $8\mu\text{A}$ was observed, which can be explained with an Ohmic connection between the gate channel and the deep-p well underneath the clear contact, caused by a too negative value of V_{CGoff} . The holes under the deep-p could then be dragged towards the negative biased p-doped backside, generating the I_{Back} current. Since the charge loss visible in the spectra did not improve, the voltage V_{CGoff} was chosen to be -4.8 V for the remaining measurements. This parasitic potential minimum for the source center geometry was studied in detail by Wölfel (2007).

The HLLSAS provides as a diagnostic tool the “gain linearity plot”, which allows to trace position-dependent charge loss. In this plot, the recombined total energy of the double events is plotted as a function of the split ratio. Since double events can only split either in the forward-backward (F-B) or in the left-right direction (L-R), the split ratio is defined as the function $F/(F+B)$ or $L/(L+R)$, where F , B , L , and R is the energy of the individual pixels. The orientation of the pixels can be seen in Fig. 5.4.

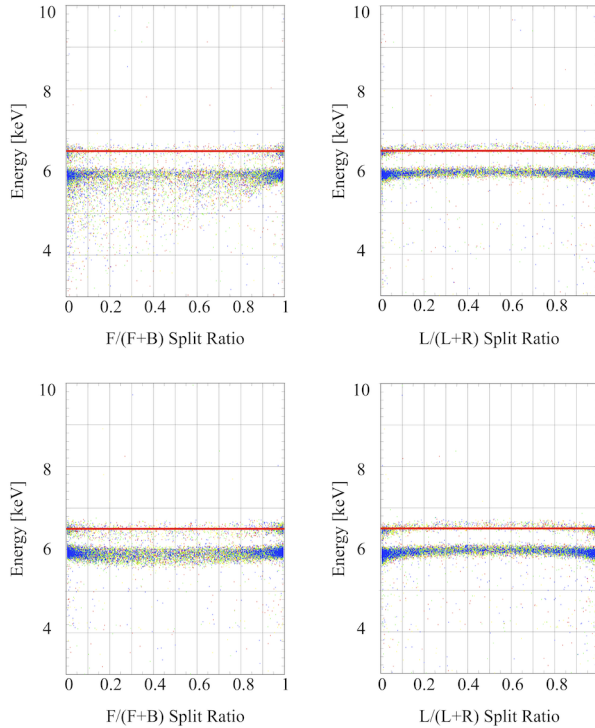


Figure 5.5: The plot shows the gain linearity of the double event distribution. The plot illustrates the dependence of the recombined pattern energy as function of the position of the split event. In the top panel the split ratios for the front illumination are shown, on the lower panel for the backside. On the right side are the L-R splits, which are unaffected by the charge loss, in contrast to the F-B splits shown in the left panels.

On the left side of Fig. 5.5 the forward-backward splits are plotted, the left-right splits are on the right-hand side of the figure. A clear difference between the two double orientations is visible. Where the L-R splits show the expected behavior, a concentration of the recombined pattern energy around 5.9 keV, the Mn K line energy, the F-B splits deviate from that straight line³. The forward-backward splits of the front illumination show the charge loss over a broad range, but with a concentration around the line energy for splits with the main component in the

³The slight upward bending of the L-R splits with a split ratio around 0.5 is again a direct result of the CAMEX non-linearity.

forward direction and only a marginal part into the backward direction. This can be explained with the asymmetric layout of the DePFET pixel, where the position of the clear structure gives the device a preferred direction. Electrons of splits in the backward direction have therefore to “pass” the clear gate structure on their way to the internal gate in contrast to the front splits. The effect is more pronounced for the front illumination as the distance travelled parallel to the surface is relatively larger with respect to perpendicular component, as compared to a back illumination. This means that the charge cloud for the front illumination spends more time in an area close to the front side where the lateral drift field is not as pronounced, resulting in more gradual charge trapping. The analysis of the F-B and the L-R splits supports therefore the assumption of a parasitic potential minimum under the clear structure as the cause of the charge loss.

5.2.4 Backside voltage scans

A set of measurements with different backside voltages was performed in order to determine its influence on the pattern distribution and on the charge loss of the double events. As shown in Eq. 3.20 the voltage applied to the backside contact determines the drift time of electrons to the potential minimum for a given detector parameter set and hence influences the resulting charge cloud size. Figure 5.6 shows the pattern distribution as a fraction of the total number of detected valid events. The fractions reflect the typical pattern distribution for a back illuminated detector, dominated by the double events. The measurement was obtained at an operating temperature of -41°C , a pixel current $I = 30\ \mu\text{A}$, and with voltages $V_{\text{CGoff}} = -4.8\ \text{V}$ and $V_{\text{Coff}} = -0.3\ \text{V}$. The analysis was performed over the complete spectral range from 0.2 to 15 keV with the secondary event threshold set to 2.5σ in order to be able to monitor small changes in the pattern distribution.

For voltages below $-140\ \text{V}$, the pattern distribution exhibits a nearly flat course with only a gradual change visible. The assumption that a smaller charge cloud size is the cause for the slight increase in the number of single events in the pattern distribution, is contradicted by an increase in the quadruples hinting for a larger charge cloud. The conclusion drawn from this behavior is that below $-140\ \text{V}$ we cannot measure a significant change of the charge cloud size with the actual measurements. Above $-140\ \text{V}$ the pattern distribution shows a significant change. The smaller patterns (singles and doubles) are declining in favor of the larger patterns (triples and quadruples), indicating a major change in the potentials within the DePFET pixel.

For further analysis the spectra of the double events were extracted from the backside voltage scan measurements. Figure 5.7 shows the extracted front and back illumination spectra. No charge loss is visible for backside voltages between

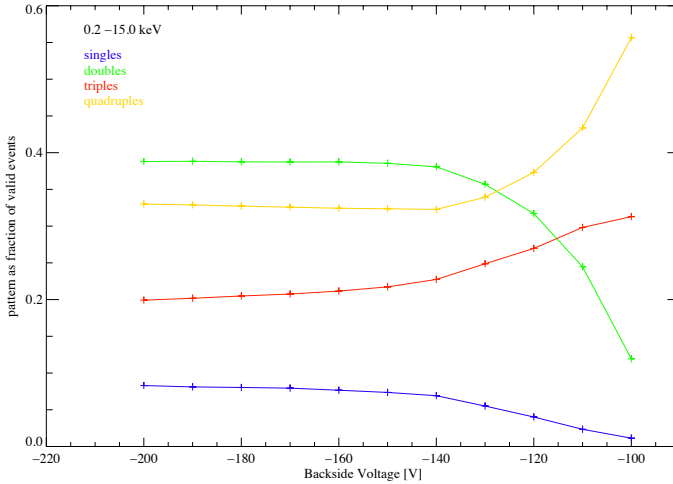


Figure 5.6: Plot of the change in the pattern distribution (back illumination) for different backside voltages. The chosen energy band is 0.2–15 keV and 5σ for the PETH and 2.5σ for the SETH. Up to -140 V only a small change in the pattern distribution is visible, below this value a significant change is observable.

-100 V and -120 V for the front and the back illumination. Starting at -130 V in the front illumination case, the charge loss is increasing gradually but seems to saturate for the higher backside voltages above -160 V. The explanation for this behavior, together with the change in the pattern distribution, could be the vertical position of potential minimum created by the backside voltage. For backside voltages from -100 V to -130 V the potential minimum might be shifted away from the front side into the bulk. The electrons created by the photon interaction still see the potential minimum of the internal gate, but due to the small resulting drift field, the charge cloud disperses more, creating therefore larger patterns. Under the clear structure charge cannot be trapped as the general potential minimum is not close enough to the front side such that the voltage V_{CGoff} has only little influence on the potential. Increasing the backside voltage to -140 V causes the potential minimum to shift closer to the front side, into a depth where V_{CGoff} starts to create the parasitic minimum under the clear structure in which charge can be trapped.

As a result of this analysis, the backside voltage was set to -140 V for all further measurements. Charge loss is already visible at this voltage, but the pattern distribution is still at a constant level compared to higher backside voltages. For

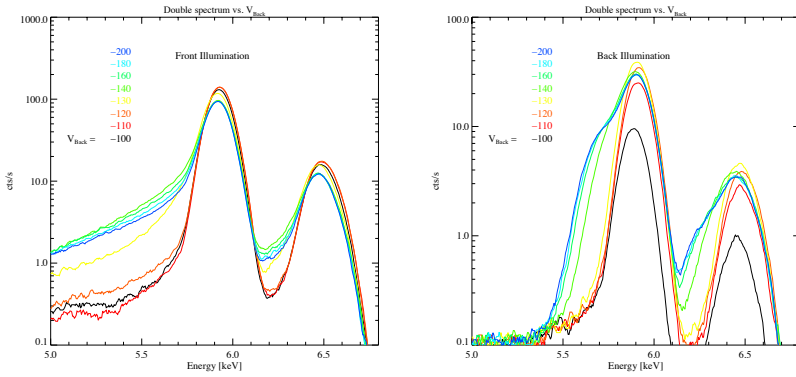


Figure 5.7: The plots show the shape of the double event spectra around the Mn K lines for backside voltages ranging from -100 to -200 V. The charge loss becomes visible for voltages below -130 V.

the verification of the simulation code, this constant pattern distribution has been preferred over the better energy resolution achieved with a backside voltage of -130 V. In the cases where the spectral shape of the double events is of concern, the analysis can be restricted to the L-R splits.

5.2.5 Temperature dependency of the offset

One of the important factors for the later operation of the DePFET matrix onboard a satellite is the temperature dependency of the offset. To characterize this, a temperature scan measurement was performed around a mean temperature of 226 K (-47°C), which is typical for the laboratory and within the range aimed for the satellite operation.

The temperature controller of the cold head, which regulates the temperature at the cold finger, where the copper braids of the cooling mask are attached, was programmed for a scan in 0.5 K steps, between 224 K to 228 K (-49 to -45°C). For each temperature, the detector was given one hour of thermalization time, after which several dark exposures and one longer front illumination measurement was performed. Throughout the measurements the DePFET matrix was continuously operated in order to maintain a stable power dissipation of the detector. The temperature values quoted in the text are the values measured with the built-in temperature diode of the DePFET matrix, located in the silicon bulk. In addition,

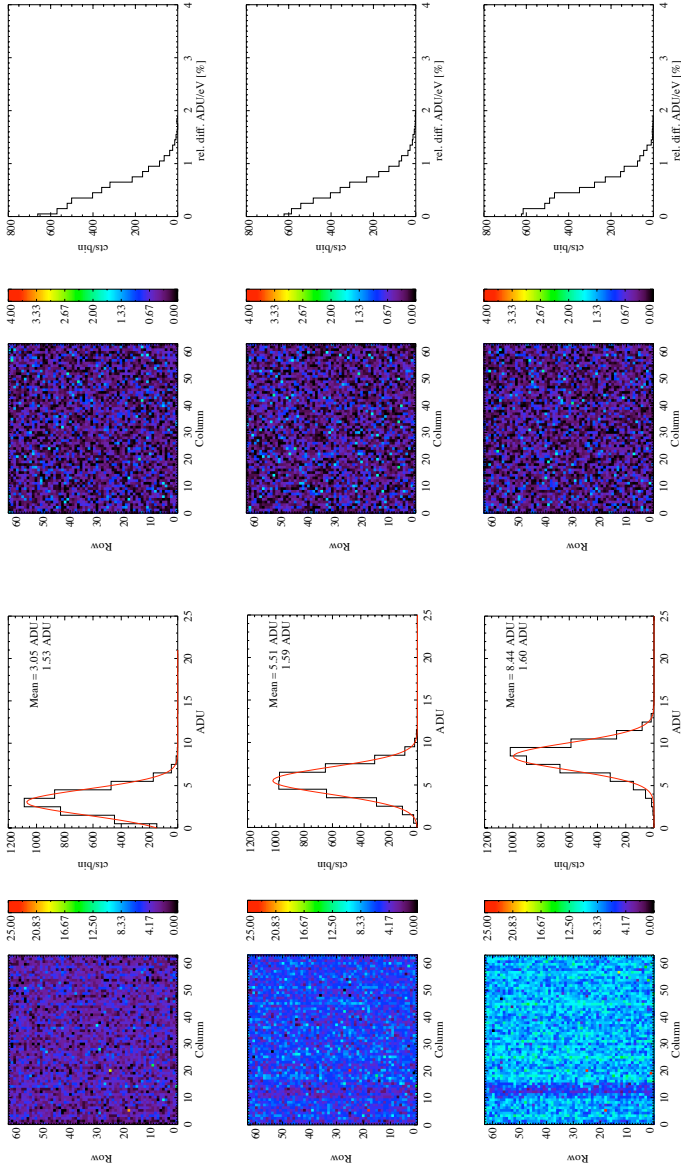


Figure 5.8: Variation of offset and gain, plotted from top to bottom for temperature differences of 0.5 K, 1.0 K, and 1.5 K, around a mean temperature of 226 K (-47°C). On the left-hand side are the offset plots, where a Gaussian distribution has been fitted to the data. The right side shows the relative differences of the gain map.

the temperature was monitored by a Pt100 resistor attached to the lower part of the cooling mask.

For the analysis, the offset values stored in the “basic.fits” are used. The offset values for the different temperatures are subtracted from each other and the absolute differences are mapped in a 2-d plot, to see if spatial correlations can be identified (Fig. 5.8). From the offset differences a histogram is calculated and a Gaussian is fitted through the obtained distribution. From the Gaussian fits an offset drift of $\approx 5\text{--}6$ ADU/K can be estimated. As expected, the σ of the Gaussian distribution is increasing with larger temperature differences, as the distribution tends to smear out. The source of this offset difference is believed not to be due to changes in the matrix itself, since measurements at IAAT and by Treis (2005) indicate that detector noise, which is dominated by the exponential behavior of the leakage current at temperatures below 253 K (-30°C), can be assumed constant throughout this temperature range of 224 K to 228 K (-49 to -45°C). The offset difference is more likely caused by a temperature dependent drift of the reference currents and voltage in the operation amplifiers within the several CAMEX stages.

The mean gain value of the matrix for these measurements is ≈ 1.05 ADU/eV. This implies that, for a space experiment in order to keep the offset variations at the 1 eV level, the temperature variance in the focal plane on the spacecraft should not exceed 0.2 K.

To check the temperature dependence of the gain values the “gn2.fits” files were evaluated, where the individual gain values for each pixel are stored. As can be seen in Fig. 5.8, no significant difference exists for the 3 plotted temperature differences of 0.5 K, 1.0 K, and 1.5 K. The gain variations are of the order of 1% of the absolute gain values for all three temperatures shown. This nearly constant width in the gain differences for all three temperatures is most likely an artifact, which could be due to small variations in the calculation of the pixel gain value in the HLLSAS. Here, for each pixel a conversion factor ADU/eV is calculated from the recorded single events in the pixels, which can result in systematic deviations, e.g, depending on the goodness of the fit (see. Sect. 5.2.1).

Small temperature changes ≤ 1.5 K, which can occur if in the laboratory the matrix has not been fully thermalized between two measurements, are not of major concern, since the offsets are calculated out of the dark-frames for each measurement individually and data are taken only for typically 5 minutes. For the gain-map of a back illumination, which is acquired from a front illumination with comparable operating parameter, temperature differences smaller than 1.5 K are thought to be within the standard precision achievable with the HLLSAS.

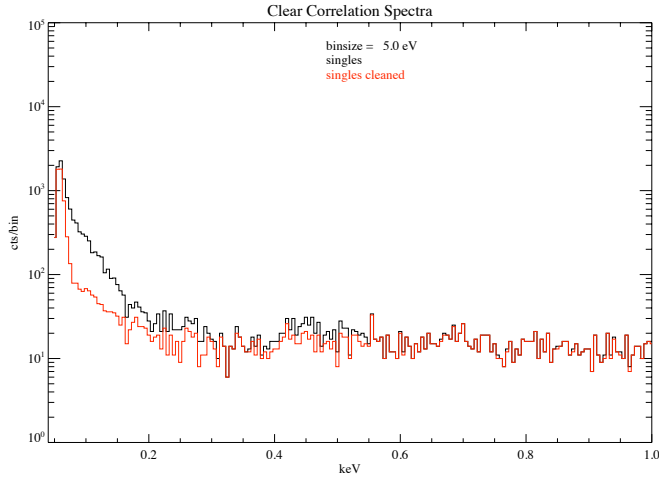


Figure 5.9: The plot shows the effect of the clear correlations, a broader rise towards the noise peak caused by low energy events. In black, all valid detected singles are plotted, drawn in red are the single events for which the detected clear correlations have been removed.

5.2.6 Incomplete Clear

One effect that has to be mentioned in the context of measurements with DePFET pixels are the so called clear-correlations. In this section a brief introduction into this topic is given, since the clear-correlations influence the low energy part of the measured spectrum and in Chapter 6 the simulation is verified relative to the laboratory measurements.

When the accumulated charge of one pixel is not completely removed during the clear process and the remaining charge can be measured in the subsequent frame this is called a clear-correlation. In order to identify these clear-correlations in valid events the “basic.fits” file is analyzed. Each pixel is searched for events with a lower energy than the event in the previous frame. If such an event is found it is marked as a clear-correlation, with a number which indicates the number of frames, i.e., the number clear processes since the initial primary event. This number defines the correlation length, which helps to identify incomplete clear processes extending over several frames. Figure 5.9 shows a front illumination spectrum between 50–1000 eV, where in black the spectrum of all valid single events is plotted and in red the same spectrum, after having removed the events caused by a clear-correlation. It can be seen, that in the red spectrum below 500 eV the rise

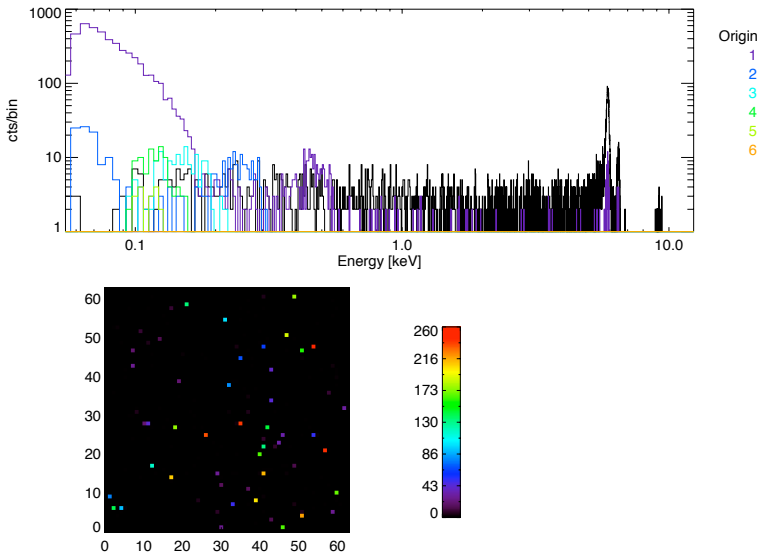


Figure 5.10: The upper panel shows the spectral distribution of the primary events (black) which lead to the clear-correlation (colored lines), plotted with a binsize of 5 eV. The color of the spectra indicates the correlation length. The lower panel illustrates the spatial distribution of the pixels with at least one clear-correlation found. The color indicates the number of detected correlations in the pixel for a data set with 230 000 frames.

towards the noise peak is more pronounced and that the main distortion of the low energy response is caused by the clear-correlations. When in the measurements all entries in the event list, holding the individual pattern components, are counted, about $\approx 1\%$ of all recorded entries are caused by the clear-correlations.

In Figure 5.10, the spectral distribution of the clear-correlation in dependence of the correlation length is shown. The majority of the clear-correlations has a correlation length of one, where the pixel is completely cleared after one additional frame by the second clear process. In the lower part of Fig. 5.10 the spatial distribution of the clear-correlations can be seen. They are isotropically distributed over the detector, but are caused by only a few pixels (4%), which also do not exhibit special behavior in terms of offset and noise. Since our interest was in a qualitative understanding of the clear-correlations, no temperature or voltage scans have been performed at the IAAT to characterize them in detail, but results have been reported by Treis (2005) and Treis et al. (2005b). The given explanation is,

that small potential barriers inside the internal gate exist, which are caused by the lithography process during the manufacturing of the devices. These small barriers delay or restrict the removal of the electrons from the internal gate, causing some residual charge to remain in the pixel after the clear process. The pixels showing clear-correlations therefore need higher clear voltages or a longer clear time as compared to the average matrix pixels, for a complete clear to take place.

CHAPTER 6

Simulations

“What we observe is not nature itself, but nature exposed to our method of questioning.”

[Werner Heisenberg]

In this Chapter the results obtained with the detector simulation code are presented. First, a general introduction into the topic of pile-up is given, with a focus on pile-up in imaging detectors. After the introduction, the simulation package itself is described in Section 6.2 where the input parameters as well as the detector geometry used are presented. In Section 6.3, the results of the simulations are compared to measured data from the laboratory setup presented in Chapter 4. The simulation package is then used in Section 6.4 to estimate the levels at which pile-up affects the different instruments of the *IXO* and the *Simbol-X* missions. The Chapter is concluded with a presentation of simulation results for some bright astrophysical X-ray sources in Section 6.5. The focus of the astrophysical simulations lies on high time resolution spectroscopy which requires a focal plane instrumentation with high count rate capability in order to achieve the science goals stated in Sections 2.1.1 and 2.2.2.

6.1 Pile-up in imaging detectors

Pile-up for imaging detectors, e.g., CCDs or DePFET arrays, is defined as the absorption of two or more photons in the same pixel and/or adjacent pixels during one readout cycle. Due to the finite spatial and temporal resolution inherent to any detector concept, the contributions of the different photons cannot be disentangled. Pile-up has therefore many consequences. First, since the charges created by the individual photons are summed up, the detected event is recorded with a higher energy. As a result, pile-up tends to harden spectra by shifting low energy events

towards higher energies. Since two or more photons are combined to one single event the total detected count rate is decreased. Whereas the net count rate for lower energies is decreased, an increase of the net count rate at higher energies may be observed. The loss of detected photons thus not only distorts the spectral shape and the PSF, but also influences the fractional root mean square variability (rms) of a time variable X-ray source.

The effects of pile-up for the *Chandra* ACIS and HETG (High Energy Transmission Grating) has been described by Davis (2001, 2002). For the MOS-CCD and the pn-CCD of *XMM-Newton*, Lumb (2000) discussed the impact of pile-up on the spectral analysis and Ballet (1999) on the detected fluxes.

With the instruments currently available for spectral imaging on-board *XMM-Newton* and *Chandra*, pile-up is already an issue for sources brighter than, e.g. 6 mCrab (Full Frame) and 100 mCrab (Small Window) observed with the EPIC pn-CCD¹. For future missions, increasing the effective area and improving the angular resolution of the mirrors in order to be able to detect and resolve weak X-ray sources, further increases the pile-up, since the sharper PSF tends to focus more photons into a smaller detector area. For *IXO*, with a planned 20 m focal length and a pixel size of 100 μm resulting in $\sim 1 \text{ arcsec}^2$ per pixel, the PSF with a 5'' HPD is oversampled by a factor 5. As a comparison, *XMM-Newton* pn-CCD² has with 14'' HPD and 4.1 arcsec^2 per pixel an oversampling rate of ~ 3.4 .

Increasing the number of pixels under the PSF in order to minimize the pile-up within each pixel, results in more pixels which have to be read out and analyzed. On the other hand, a faster read out and processing time usually increases the system noise and thus worsens the achievable energy resolution. Therefore a compromise between the pixel size, the PSF, and the readout time has to be found.

Options for observation strategies to mitigate pile-up, e.g., off axis observations, out-of focus operation, with their advantages and disadvantages are discussed by Davis (2001). One option offered in the current instrument baseline are the "window" modes in which, for the *IXO* WFI and the *Simbol-X* LED, only a small ROI is read out. This approach results in a much shorter achievable frame time as compared to the full frame mode, at the expense of a reduced FOV, where only one point source may be observed. Another option is to remove the pile-up area in the source center after the observation and restrict the data analysis to the outer wings of the PSF.

¹The values at which pile-up deteriorates the response depends strongly on the operation mode. In the timing mode the pile-up limit is shifted up to 800 mCrab at the price of the loss of spatial information in one dimension [details see Ehle et al. (2008)].

²*Chandra* ACIS is a different case in this context, as the PSF with a 0.5'' HPD is under sampled by a pixel size of 0.49 arcsec^2 per pixel.

6.1.1 Energy pile-up

The type of pile-up described above, i.e., when more than one photon hits the same pixel during one frame, is also called energy pile-up. The count rate at which energy pile-up starts can be estimated analytically. If the incident photons follow a Poisson distribution, the time intervals between subsequent photons have an exponential distribution, as derived in Sect. 6.2.

6.1.2 Pattern pile-up

An event where the charge created by the incident photon in the detector is distributed over several pixels, is called a split event. The photon energy can be reconstructed as the sum of the individual charges deposited in the neighboring pixels during one frame. This reconstruction is only possible if the count rate is sufficiently low such that isolated patterns³ can exist. Figure 6.2 illustrates the valid pattern types. When the event rate is higher, the probability of having photon hits in adjacent pixels rises and pattern pile-up becomes a problem, because the created charge clouds can partly overlap and shift the pattern types towards larger patterns. Since the charge distribution of pile-up events cannot be distinguished from that created by a single photon, the analysis software erroneously presumes the events to be caused by a charge split and reconstructs a too high photon energy. In the case of pattern pile-up the measured count rate information is consequently incorrect, since photons arriving in neighboring pixels will not be correctly counted and the shape of the measured spectrum is distorted, like in the case of energy pile-up. In addition, pattern pile-up can cause the creation of patterns which are inconsistent with those of photon events. This pattern migration towards invalid patterns causes an additional reduction in the count rate, since these events are excluded by the analysis software (either on-board the satellite, or in the offline analysis). In extreme cases of pile-up, a hole in the center of the PSF is created, where no valid events can be detected. This effect is illustrated in Fig. 6.19 as one result of the pile-up simulation. In the case of *IXO*, where the smaller pixel size causes more split events than compared to the pn-CCD of *XMM-Newton*, this effect is even more pronounced.

The probability of two photons to hit neighboring pixels, or to create adjacent split events, is much higher than the probability of two photons to hit the exact same pixel. In detectors where pattern pile-up is possible, it already becomes a problem at significant lower count rates than energy pile-up alone. The typically used Poisson estimates for energy pile-up cannot be used to calculate the expected pile-up fraction in detectors where pattern pile-up is possible. As pattern and energy pile-up can occur in any combination depending on the exact position of

³“Pattern” is the *XMM-Newton* term of *Chandra*’s “grade”.

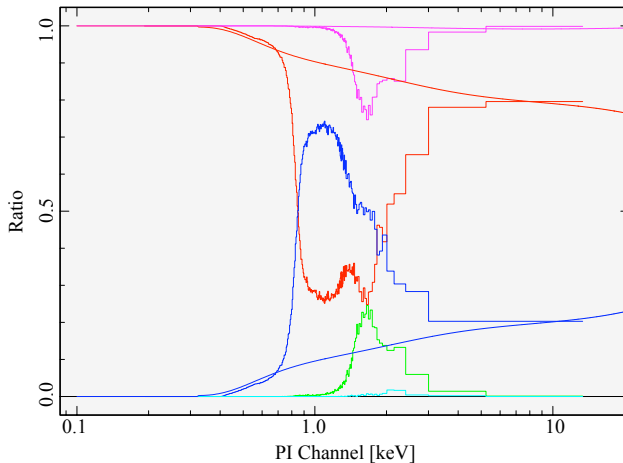


Figure 6.1: Result from `epatplot` for an observation of RS Ophiuchi, which suffers from high pile-up. The smooth lines show the expected, the histogram the measured pattern distribution at different energies. The red line represent the single, blue the double, green the triple, and light blue the quadruple events. The sum of single and double events is plotted in magenta (Image courtesy of M. Hanke).

the photon interaction, and thus cannot be separated apart in a unique way, they are referred to only as pile-up in the following.

One way to identify if pattern pile-up is influencing a measurement, is to look at the fraction of single, double and higher clustered events. If the measured fractions differ from the fractions of a low count rate source, pile-up has occurred. This is done, e.g., by the `epatplot`-routine of the XMM SAS. It is then up to the user to decide what to do with the obtained data, and whether the science goals can still be reached. Figure 6.1 shows the `epatplot` of the heavily piled-up measurement of the cataclysmic variable RS Ophiuchi during a nova outburst with a visual magnitude of 4.5 in 2006, as seen by *XMM-Newton* in the timing mode.

In principal it is possible to correct for the effects of pile-up to a certain extent, as described by Davis (2001) for the *Chandra* ACIS. But since pile-up is a nonlinear problem and no correction mechanism is perfect, it is preferred to build instrument configurations and develop readout strategies which minimize the occurrence of pile-up.

6.2 The simulation package

The Monte-Carlo based simulation code described below was developed to study various aspects of semiconductor based detectors. The code simulates the actual readout cycle handling of the detectors, i.e., the row-by-row readout in multiple directions. Detector dead time is included as well as the correct handling of pile-up and split events. With the current code package DePFET-based detectors, e.g., the *IXO* WFI including its window modes, and the *Symbol-X* LED and its window mode can be simulated. In addition, a simplified model of the *IXO* HTRS is implemented. The code allows a realistic simulation of source spectra based on the available detector response matrices and allows to handle time variable sources, while also taking the proper Poisson statistics into account.

6.2.1 Simulation Code

The simulation code is written in IDL⁴ since it allows a fast and flexible use of large data arrays together with an easy data visualization. Together with the available routines in the `astrolib` and `aitlib`, the FITS-based results can be interpreted with the standard `ftools` and `XSPEC` (Arnaud 1996). Three main inputs are needed for a realistic simulation: a light curve, an input spectrum, and information about the telescope and the detector.

In order to be able to generate random events (photons) which follow a Poisson random process in the Monte-Carlo approach of the code, the time distribution between two successive events has to be known. Therefore the probability of an event occurring in the time interval dt after a time t has passed since the last event at time $t = 0$ must be calculated. As shown in Knoll (2000), the probability of an event taking place within the next time bin dt after a time t can be written

$$I_1(t) dt = P(0) \cdot r dt \quad (6.1)$$

where $P(0)$ is the probability that no event has taken place in the time from 0 to t . The product $r dt$ is the probability of an event to occur during the time interval dt , with r as the average rate in the corresponding time bin.

Taking the distribution P to be Poissonian, the probability that no event occurred up to time t is given by

$$P(0) = \frac{(rt)^0 e^{-rt}}{0!} = e^{-rt} \quad (6.2)$$

Inserting this into Eq. 6.1 leads to an exponentially distributed probability for the occurrence of the next photon as

$$I_1(t) dt = r e^{-rt} dt \quad (6.3)$$

⁴Interactive Data Language from ITT Visual Information Solutions (<http://www.itervis.com/>)

In the simulation code arrays containing the time and average rate r within each time bin are created from the light curve. Assuming the Poisson distribution to be a valid description of the source photons, the average rate r within each time bin is taken as basis for the generation of the exponentially distributed photon arrival time as shown by Eq. 6.3. Any light curve can be taken as basis of the photon generation. Some basic light curves (e.g., flat, sinusoidal) are provided within the code as well as more advanced light curves based, e.g., on the Crab pulse profile.

As a caveat, the implementation of the photon generation using the above described method works perfectly only for large count rates. The limit of the code is reached for low count rates and fast changes in the pulse profile, when the average rate causes the average time between the individual events to be of the same order as the time bin size. In this case a photon generation can be delayed to the next time bin, where the count rate already changed, causing a too low photon generation for this time bin. For the count rates of typical X-ray sources shown later on, e.g., the Crab pulsar, neutron star eclipses, or X-ray bursts this effect is not an issue.

The input spectrum is created with XSPEC. A model, describing the source to be simulated is defined. These spectra can be, e.g., line spectra for the laboratory setup, a model describing an astrophysical source (“The Crab”), or any other artificial spectrum. The model is then folded with the response matrix of the respective instrument and a spectrum is obtained by the `fakeit` command without choosing the Poisson error statistic option. The response matrix usually contains information about the effective mirror area and the quantum efficiency of the detector for each energy bin. Also included in the response is the redistribution matrix file (RMF), which gives the probability to detect a photon with energy E in the channel $I(E)$. Since the detection probability of a photon is included in the created spectrum, all photons generated by the simulation code can be detected. The simulation code converts the provided input spectrum, given in PHA channels, into a cumulative probability distribution. The PHA values of the incident photons are then drawn from this distribution.

Finally the spatial position of the interaction on the focal plane has to be calculated. In order to calculate the illumination of the detector several options exist. A homogenous illumination is implemented, used either for the simulation of the laboratory model, or to model the out-of-focus operation of the focal plane detector. The second option utilizes a Gaussian approximation of the point spread function (PSF) of the telescope. In the case of *XMM-Newton* a King profile⁵ is

⁵The King profile given by $A \left(1 + \left(\frac{r}{r_c}\right)^2\right)^{-\alpha}$, where r is the radial distance to the center of the PSF, has the advantage that the core (with radius r_c) and the wings of the PSF (dominated by the slope α) can be modeled independently.

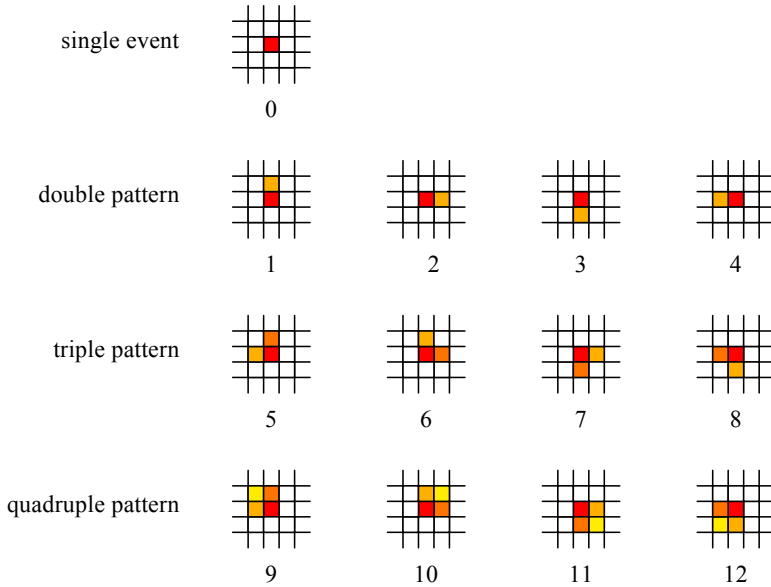


Figure 6.2: The 13 valid pattern types which can be produced by a single photon. In this plot, a darker color indicates higher energy. The nomenclature shown here follows the convention used for the pn-CCD on-board of *XMM-Newton*, which is also used by the simulation code presented. The HLLSAS identifies the same valid patterns, but uses a different labeling scheme.

used to model the PSF (Ehle et al. 2008). Since in this early planning phase of the simulated missions the PSF is known only with large uncertainties, a Gaussian shape for the PSF is a reasonable assumption. The standard deviation σ_{PSF} of a Gaussian shaped PSF is calculated from the focal length and the HPD of the telescope with

$$\sigma_{\text{PSF}} [\text{m}] = \frac{\text{HPD} ['']}{2.35 \cdot \arctan\left(\frac{\text{pixelsize} [\text{m}]}{\text{focallength} [\text{m}]}\right) \cdot \frac{360}{2\pi} \cdot 3600 \cdot \text{pixelsize} [\text{m}]} \quad (6.4)$$

The center position of the PSF can be chosen to be anywhere on the detector plane.

From the spatial position of the incident photon on the detector calculated in μm , the column and row of the interaction are computed, since the pixel sizes are

known. In the simulation setup it can be specified whether split events are possible in the detector or should be neglected. If split events are considered, the distances from the interaction point to the surrounding pixel edges are computed. The created charge cloud is assumed to be Gaussian shaped with a standard deviation of σ_{cc} . The value of σ_{cc} is set to $11 \mu\text{m}$, but different values can be specified by the user. In the current version of the code a constant, energy independent, charge cloud size is assumed. The fraction of the charge cloud which is split into the adjacent pixels, as shown in Fig. 5.4, is calculated with the `idl gaussint` function. The diameter of the charge cloud is restricted to $6\sigma_{cc}$, which accounts for 99.7% of the charge. From the charge fraction the PHA value within each pixel is calculated. In the detectors produced by the HLL, i.e., the DePFET and CCDs, only splits with up to 4 constituents can be produced by one single photon. The number of constituents and the pattern type formed depend on the distances relative to the pixel edges. Only 13 valid pattern types exist (Fig. 6.2) which can be unambiguously related to a photon hit and the photon energy can later be reconstructed.

For each of the events created within a split, including the primary event, the code now checks whether this event can be detected or has to be discarded because it occurs during the clear process of the actual row or falls outside of the active detector region. If the event can be recorded, the code checks if in this pixel an event has already been recorded since the last readout. If this is the case, the PHA values are added. With this method we can account in a natural way for energy and pattern pile-up as well as for the dead time of the detector.

The readout scheme of a DePFET matrix row consists of the signal sampling, the clearing of the pixel and the baseline sampling. As already explained in Section 4.4.1.2 photons entering the detector during the signal sampling are recorded with a lower energy, since they miss part of the signal sampling process. Photons entering the detector during the baseline sampling modify the recorded signal in two ways. If a photon in this pixel has already been subject to the signal sampling, its energy will be recorded with a lower PHA value which can be in extreme cases even below the noise peak, and will therefore be discarded by the analysis. The second photon is then subsequently recorded in the next frame, as the clear process already has taken place. Since these effects are strongly dependent on the chosen CAMEX timing, the code uses a simplified readout procedure as shown in Fig. 6.3. The clear process, with a duration t_{clearrow} takes place at the beginning of the row readout $t_{\text{readoutrow}}$. In the simulation, the row which is currently read out is considered to be insensitive for photons during the clear period. These photons are not recorded, but charge spilled over from split events into adjacent rows is still detected and included in the simulation. Photons detected in this row during the remaining time of the readout phase do not influence previously recorded photons and are read out in the next frame.

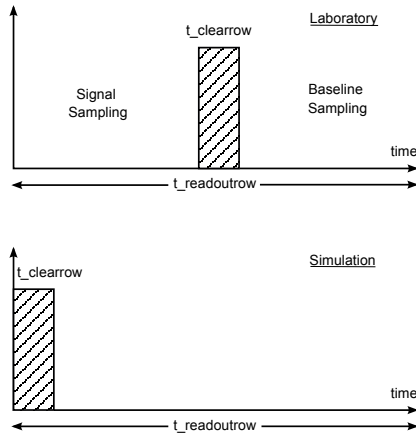


Figure 6.3: Comparison of the clear pulse position between the laboratory setup and the code implementation. In the simulation the duration of the baseline sampling is twice as long as for the measurements.

All events which could be detected are written into an event list, sorted by the readout time. After all photons have been simulated a lower energy threshold (LTH) is applied to the event list. Events with PHA values below the LTH are discarded and not included in the pattern recombination.

The remaining entries in the event are fed into the pattern-recognition algorithm. All events belonging to one frame are grouped together. They are scanned for clustered events with a recursive search function. These clusters are then analyzed if they form one of the valid pattern types shown in Fig. 6.2. As additional criteria, besides the shape of the cluster, the code verifies that for a triple event in order to be registered as valid event, the pixel with the highest energy has to be located in the corner of the pattern. For a quadruple, the event with the highest and the lowest energy have to be located diagonally. All other patterns are marked as invalid since they cannot be caused by a single photon. The pattern energy, as mentioned earlier, can therefore not be directly related to the photon energy in a unique way. Patterns larger than quadruples cannot be created by one photon and are therefore always marked as invalid. From the events which form a valid pattern, the energy is summed up and stored in the pixel with the highest energy fraction. In addition, events at the detector border are flagged, since part of the charge could be splitted outside of the pixelized area. A flow chart summarizing the simulation in- and outputs and providing a simplified version of the photon handling in the detector simulator is presented in Fig. 6.4.

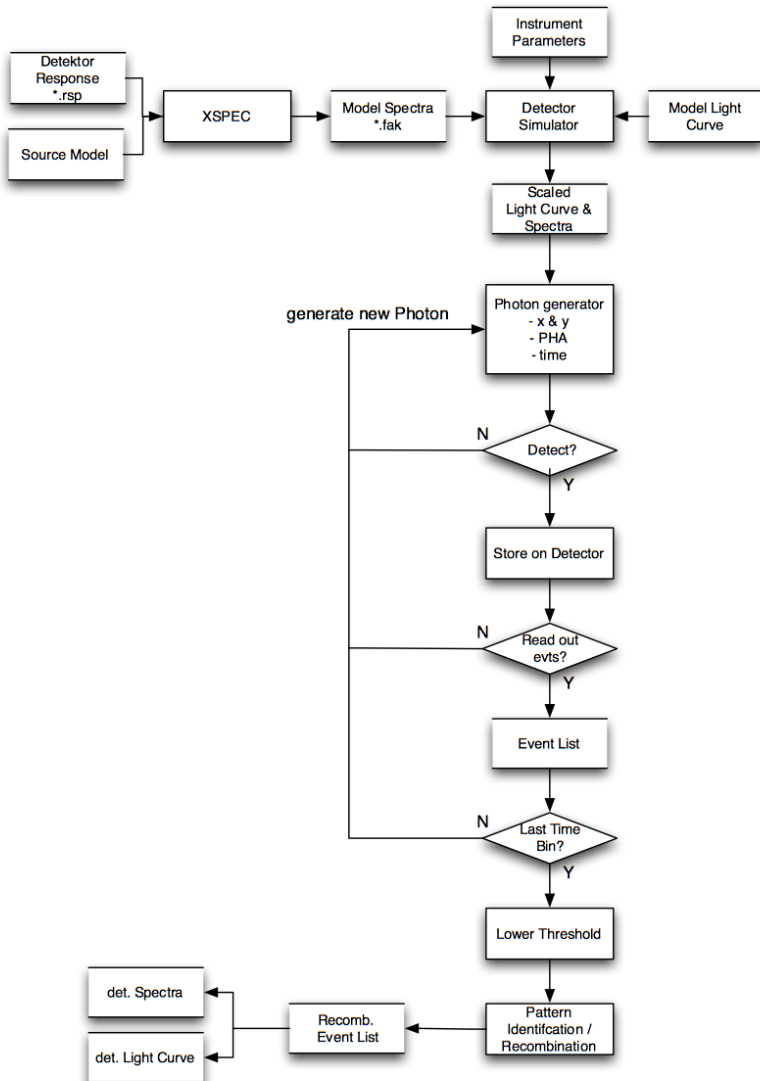


Figure 6.4: The flow chart shows the main input parameters of the simulation at the top. The photons are generated and traced through the detection and readout process. At the bottom of the figure, the post processing is illustrated.

6.2.2 Input Parameters

For the simulation code most input parameters can be chosen freely within reasonable range, but several predefined instrument sets exist to ease the operation. In the following the main parameter sets are listed.

IXO Wide Field Imager

For the calculation of the Gaussian shaped PSF an *IXO* focal length of 20 m, as well as a HPD of $5''$ is considered, which leads to a standard deviation of $\sigma_{\text{PSF}} = 206 \mu\text{m}$. A detector size of 1024×1024 pixel is planned, each with a size of $100 \times 100 \mu\text{m}^2$ which corresponds to 1.03 arcsec^2 per pixel. About 99% of the PSF will thus be covered by a subset of $\sim 12 \times 12$ pixel. The DePFET detector features two readout directions. Reading one row takes $t_{\text{readoutrow}} = 2 \mu\text{s}$ and the clear duration is assumed to be as short as $t_{\text{clearrow}} = 200 \text{ ns}$. These values are taken from the ESA Cosmic Vision Proposal (Turner & Hasinger 2007) and are updated to match the latest *IXO* payload description (IXO-IWG 2009).

For the **full frame mode** of the WFI, thereafter only WFI, all 1024×1024 pixel are assumed to be readout in two directions, which results in a frame time of $512 \times 2 \mu\text{s} \sim 1 \text{ ms}$. The simulated point source is typically placed at the center of the detector, such that an equal amount of photons is read out in either direction.

The **window mode** is implemented as a 16×16 pixel subset located in the center of the WFI. A bidirectional readout is assumed in the simulation. With the window mode, sources with higher fluxes can be observed, since the smaller active area allows a faster frame time ($8 \times 2 \mu\text{s} \sim 0.016 \text{ ms}$). With the current assumptions for the *IXO* focal length and angular resolution, the active detector size of the window mode is large enough to enclose the complete Gaussian PSF. Even for the previously considered pixel size of $75 \mu\text{m}$ of the *XEUS* mission, only 0.5% of the photons fall outside this area.

IXO High Time Resolution Spectrometer

For the HTRS simulation the baseline instrument parameters as presented in IXO-IWG (2009) are used. In this configuration 37 hexagonal shaped Silicon Drift Detectors are foreseen, each pixel with a radius of $r = 2.3 \text{ mm}$. Since, in order to distribute the incident photons over as many pixels as possible the HTRS will be operated out-of focus, the Gaussian shaped PSF cannot be used. Calculations by Oosterbroek (2009) show that the resulting illumination is not completely homogenous but varies for the individual pixel between 1.0% for the corners and 3.5% for the most exposed pixels in the concentric inner ring. In these calculations 99.5% of the flux falls onto the HTRS. In the simulation code, this

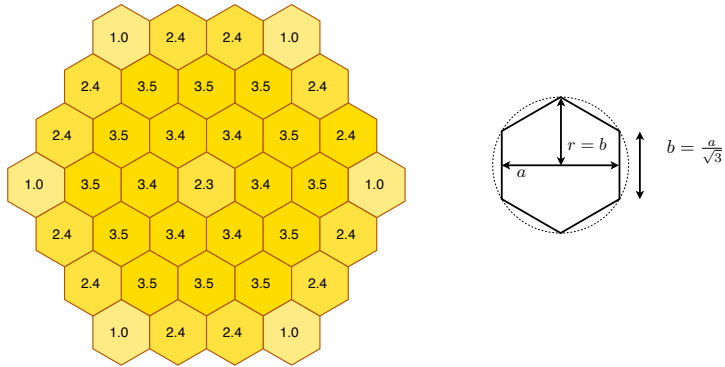


Figure 6.5: Relative illumination of the 37 hexagonal SDD elements of the *IXO* HTRS (after T. Oosterbroeck). On the right side, the geometry of one pixel cell is drawn. With a radius $r = 2.3$ mm, each pixel has an area of 5 mm^2 .

relative illumination coefficient is used to distribute the photons onto the SDD array (see Fig. 6.5). Since the quoted shaping time is expected to be as short as 75 ns, a dead time of 300 ns is assumed during which incoming photons are discarded.

***Simbol-X* Low Energy Detector**

The parameter set for the *Simbol-X* LED is based on the values published by Ferrando et al. (2009) and Lechner et al. (2008). The *Simbol-X* focal length was assumed to be 20 m. The published required angular resolution is $20''$ (HPD) with a goal of $15''$. For the simulation runs, the reference value used in the *Simbol-X* response of HPD = $18''$ was chosen. The detector has 128×128 pixel, each with a size of $625 \times 625 \mu\text{m}^2$. The Gaussian PSF is calculated with the above mentioned values and results in $\sigma_{\text{PSF}} = 743 \mu\text{m}$. In the current planning phase the readout technology of *IXO* and *Simbol-X* is identical, the readout time of one row $t_{\text{readoutrow}} = 2 \mu\text{s}$ and the clear duration $t_{\text{clearrow}} = 200 \text{ ns}$ is the same as for the *IXO* simulations. Besides the clear duration no other dead time contribution is assumed. Since the focus of the simulation lies in the bright source capabilities of the instruments, the anti-coincidence is supposed to be turned off, and does therefore not contribute to the dead time. Due to the smaller number of pixels, the frame time of the **full frame mode** is $64 \times 2 \mu\text{s} \sim 128 \mu\text{s}$ with 2 readout directions.

The **window mode** with 2 readout directions and only 32×128 pixel will result

in a frame time as short as $16 \times 2 \mu\text{s} \sim 32 \mu\text{s}$.

Laboratory DePFET matrix

For the simulation of the laboratory measurement, a homogeneously illuminated detector array with 64×64 pixel was implemented. Each pixel has a size of $75 \times 75 \mu\text{m}^2$ and the laboratory matrix has only one readout direction. The measured values of $t_{\text{readoutrow}} = 32.625 \mu\text{s}$ and of $t_{\text{clearrow}} = 1.2 \mu\text{s}$ result in a frame time of 2.088 ms.

6.2.3 Response Files

In the generation of the input spectra the latest response files which were available have been utilized. Since the mirror modules for neither of the two missions have been produced so far, the response files should always be considered as preliminary.

IXO

For IXO, the WFI and HTRS response files (`IXO_CDF_wfi_default.rsp`, `IXO_CDF_htrs_default_081117.rsp`) have been downloaded from the official NASA website⁶. The baseline mirror module has an effective area of 3 m^2 at 1.25 keV, 0.65 m^2 at 6 keV, and 150 cm^2 at 3 keV. We assume that the mirrors are produced with the silicon pore optic technology, as currently investigated by ESA, and have an Iridium and Carbon overcoating (Collon et al. 2008). Another mirror option pursued by NASA uses slumped glass as the base material (Zhang et al. 2008b), but since the required effective area is the same for both, no significantly different results are expected. In the case of the HTRS response, the loss in effective area due to the gratings has been modeled and was taken into account. The exact implementation of the gratings is yet unknown, but for the simulation of the detector performance this is of minor concern, since the difference in the count rates of the response matrices for the HTRS and the WFI is $< 0.6\%$.

Simbol-X

For the low energy detector (LED) of Simbol-X the response files (`MPD_Ref2.arf`, `MPD_TB_200_OA0.arf`) distributed by CNES in Dec. 2008 were used. They are based on an effective area of 1000 cm^2 at 2 keV, 600 cm^2 at 8 keV, and 300 cm^2 at 30 keV as reported by Ferrando et al. (2009). In the response file, the transmission of an additional optical filter on the detector entrance window is included as well as the quantum efficiency ($450 \mu\text{m}$ thick silicon). The energy is redistributed with a

⁶<http://ixo.gsfc.nasa.gov/>

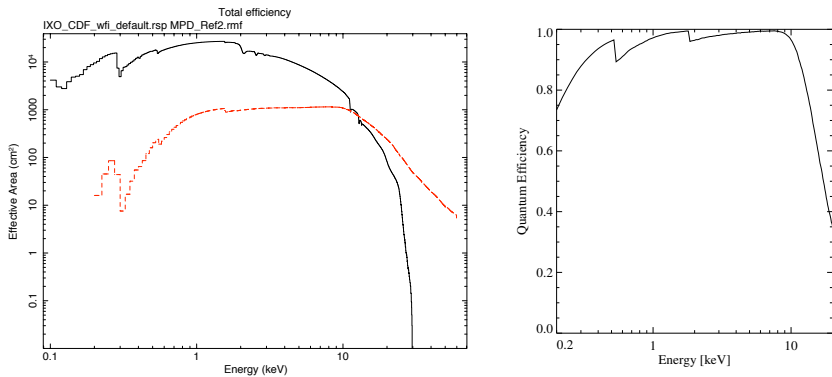


Figure 6.6: Left panel: Comparison of the total efficiency of the *IXO* WFI (black) and *Simbol-X* LED (dashed red) response matrices. In the total efficiency, the effective area and the quantum efficiency are included. As can be clearly seen, the *IXO* mirrors have a larger effective area, and extend to lower energies. Above 10 keV *Simbol-X* has the higher total efficiency due to the high energy extension of mirror area. Note, these are the low energy detectors of both missions. Right panel: The quantum efficiency of silicon with a thickness of $450\mu\text{m}$, including an EPIC-pn type thin filter (Strüder 2008, priv. comm.).

Gaussian shape with an energy dependence of the standard deviation proportional to \sqrt{E} , with an energy resolution of 150 eV FWHM at 6.5 keV.

Laboratory

In order to generate a response matrix for the laboratory setup, an effective detector area and a redistribution matrix are needed. Since the setup contains no mirror, only the detector area given with $4096 \times 75\mu\text{m} \times 75\mu\text{m} = 0.23\text{cm}^2$ needs to be taken into account. The detector area is assumed to be energy independent and is scaled with the quantum efficiency in order to obtain the appropriate interaction probability. The values used for the quantum efficiency correspond to a $450\mu\text{m}$ thick silicon detector without any filters. For the energies above 1 keV observed in the laboratory, the differences of the quantum efficiency to the values shown in Fig. 6.6 are negligible.

A redistribution matrix file (rmf) is created for the energy between 0.1 and 20 keV, containing 4096 channels. The energy spacing of each channel is therefore $(20 - 0.1)/4096 \approx 4.85\text{eV}$. For each input energy bin E_i , the probability to be detected in channel I is calculated. The energy dependent detector resolution is assumed to follow a Gaussian distribution, where the standard deviation σ_E is

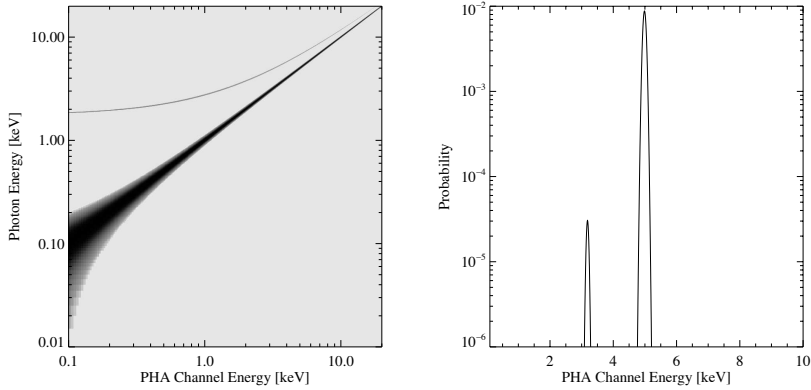


Figure 6.7: Left side: The image of the created redistribution matrix for the laboratory setup. The main detection probability is clearly visible, as well as the escape peak. Right side: Cut through the matrix for a photon energy of 5 keV, showing the Gaussian shaped redistribution peaks.

scaled with the energy of the input bin. The expression for σ_E was derived in Sect 3.2.3. To Eq. 3.26, an additional term to account for the system noise is added:

$$\sigma_E = \sqrt{(\text{ENC} \cdot w)^2 + (w \cdot F \cdot E)} \quad (6.5)$$

Values of $w = 3.66\text{eV}$ for the electron-hole pair energy and $F = 0.12$ for the Fano factor were used (Perotti & Fiorini 1999). From the measurements presented in Sect. 5.2.2, a system noise of $\sim 6\text{ENC}$ was derived. These values lead to a 131 eV FWHM for an input energy of 6 keV.

An escape peak, having its origin in the $E_{K_\alpha} = 1.75\text{keV}$ binding energy of the silicon K-shell electrons (see Sect. 3.1.1), was also included in the redistribution matrix. Kang et al. (2002) used an X-ray fluorescence experiment to measure the energies and intensities of the escape peak of a Si(Li) detector, under illumination with X-ray photons of different energies. For a first test, we use the reported escape peak probability of 0.25%, obtained for an illumination with ^{55}Fe . We assign this probability to all input energies exceeding 1.75 keV. The standard deviation of the escape peak is modeled with

$$\sigma_{\text{esc}} = \sqrt{(w \cdot F \cdot (E - E_{K_\alpha}))} \quad (6.6)$$

An optional Compton component is basically implemented, but has not been subject to detailed testing. The Compton shoulder has its origin in inelastic scat-

tering processes of the incoming X-ray photons with the outer shell electrons of the detector material. These scatterings lead to an energy loss of the X-ray photon, thus broadening the Gaussian line shape at the lower energy wing.

The created response matrix is plotted on the left side of Fig. 6.7. On the y -axis, the incident photon energy E and on the x -axis the detected channel I , given in units of keV, are plotted. A darker color indicates a higher probability for a given input energy E to end up in the corresponding channel. The main distribution line can clearly be seen. For energies above the Si K-shell, the escape peak becomes visible. To illustrate the Gaussian line shape, a horizontal cut through the *rmf* is performed at an input energy of 5 keV and shown in the right panel of Fig. 6.7. The higher peak is related to the main interaction probability, the lower peak represents the probability of the photon to end in the escape peak. The integral under both peaks is proportional to the total interaction probability, here given by the effective detector area.

6.3 Verification of the code

In order to evaluate the performance and to estimate the accuracy of the simulation code, results from the simulation are compared to actual measured values obtained with the DePFET laboratory setup at the IAAT. In the following sections the timing performance is checked and the charge splitting behavior is compared. Thereafter the quality of the pile-up modeling is discussed, followed by a comparison of the spectral properties.

The input spectrum for the simulations was created in *xspec* with two lines at 5.9 keV and 6.4 keV and with a normalization of 7:1 in order to reflect the relative intensities of the Mn K_α and Mn K_β lines. The line width was specified to be 0.1 eV, the energy resolution is therefore completely determined by the custom created response matrix and by readout effects. A constant photon rate is assumed in the simulation, except in the case of the timing performance check.

6.3.1 Timing performance

The timing performance of the code is verified through comparison with measurements of time variable X-ray source. For these measurements a radioactive ^{55}Fe source is mounted in the housing of the chopper wheel (see Sect. 4.5.6) which illuminates the detector from the backside. Through the rotating wheel the source intensity is modulated. The pulse period, as given in Table 4.2, depends on the chosen motor speed, the pulse shape on the geometry of the chopper wheel.

For the two chopper wheels, shown in Fig. 4.19, pulse profiles have been calculated. In the case of the chopper wheel with the 4 elongated holes, the source

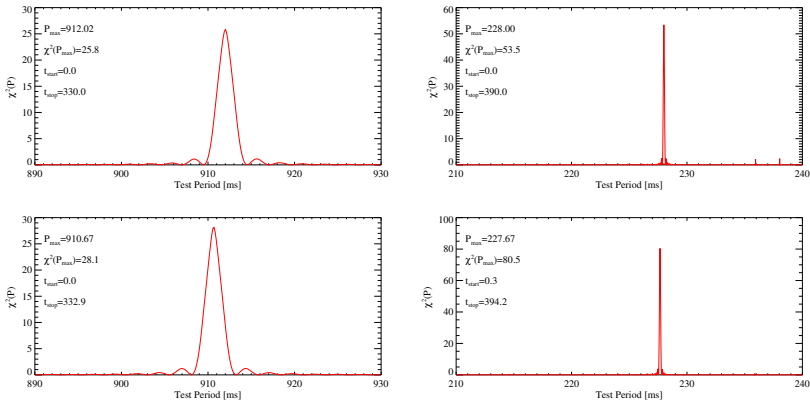


Figure 6.8: Pulse periods found by `epfold`. The top panels show simulations, the bottom panels the laboratory pulse periods. On the left side, the 912 ms periodograms for the 4-hole chopper wheel are plotted, on the right side the 228 ms ones for the chopper wheel with 16 holes.

is assumed to be open for the complete length of the arc, excluding the circular shaped ends. These ends, which determine the rising and falling edges of the pulse profile, are linearly approximated. In the case of the 16-hole wheel, the holes are circular with a 4 mm diameter, the same diameter as the cover of the radioactive source in the mount. The pulse profile was therefore calculated from the temporally changing overlap of the two disks (in principle the same as for, e.g., a solar eclipse). With these pulse profiles, light curves are produced as simulation input. From the obtained data, laboratory measurements and simulations, the valid events were extracted for the analysis.

The pulse periods were then calculated with the epoch folding routine `epfold` (Leahy et al. 1983), based on the valid event list. In this method an array of test periods are folded through the data to create pulse profiles. For these arrays of pulse profiles a χ^2 -test is performed, where they are compared to a light curve with a constant count rate. The calculated χ^2 should thus exhibit a maximum at the actual period, since for this period the deviation from a constant count rate is the largest. Aliasing effects and beat maxima, which can be introduced by gaps in the observation, can bias the period search process. These effects can be neglected in the current analysis, since the period searched for is known and the light curve is continuous for the short observation time. A more detailed introduction to epoch folding is given, e.g., by Fritz (2004).

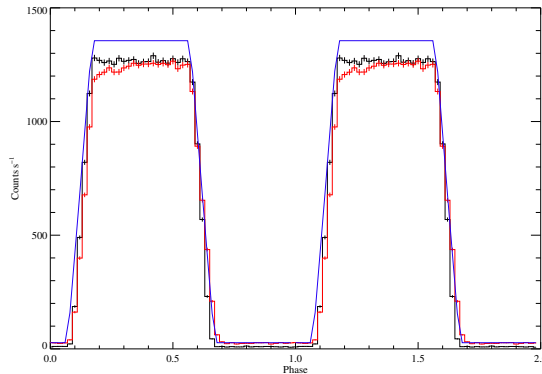


Figure 6.9: The pulse profiles of the 912 ms, 4-hole chopper wheel setting. Plotted in black is the pulse profile based on the laboratory data and plotted in red is the result of the simulation. Over-plotted in blue is the simulation input profile. The count rate deficit of the simulation output with respect to the input is due to border events.

In Fig. 6.8, two examples of the `epfold` results are shown. The width of the bell shaped curve for the different χ^2 -values of the test periods can be used to estimate the size of the period error according to

$$\Delta P = \frac{P^2}{T} \quad (6.7)$$

where P is the period and T is the observation time. Since T is limited in the laboratory measurements to $\sim 6\text{--}7$ min due to the data size, the width ΔP is obviously larger for the 912 ms period. As pointed out by Fritz (2004) and Benlloch et al. (2001), the value of ΔP has no significance but serves as a check for the consistency of the period found.

As examples, for the setup with the 4 elongated holes, the pulse period has been measured to $911.5 \pm 4.3\text{ms}$ with the light barrier. The analysis of the measurement results in pulse period of 910.7 ms ($\Delta P = 2.5$ ms), the simulation gives 912 ms ($\Delta P = 2.5$ ms). In the case of the 16-hole setup, a period of 227.5 ± 3.3 ms is measured with the light barrier, 227.7 ms ($\Delta P = 131.5\mu\text{s}$) result from the measurement, and 228 ms ($\Delta P = 133.2\mu\text{s}$) from the simulation.

In Fig. 6.9, one example of a pulse profile is shown. To obtain this pulse profile the data were folded by the `pfold` routine with the best period. The measured pulse profile (black) is plotted together with the simulation result (red) and the input pulse profile (blue). As can be seen, the pulse periods and the pulse profiles are

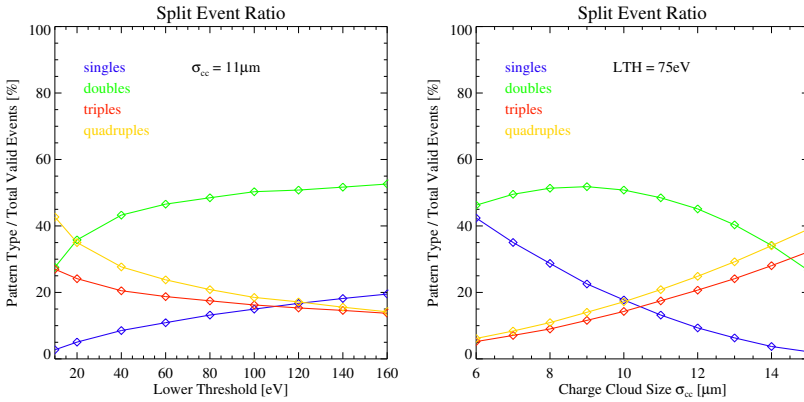


Figure 6.10: Left panel: Pattern distribution for different low energy thresholds (LTH) and a fixed charge cloud size $\sigma_{cc} = 11 \mu\text{m}$. The pattern fractions are given relative to all valid detected events. With increasing LTH lower pattern types are created by removing minimal charge spills from the triple and quadruple events. Right panel: Pattern distribution for different σ_{cc} and a constant 75 eV LTH, illustrating the trend towards higher pattern types with increasing charge cloud sizes.

well modeled by the simulation. The count rate difference between the simulation input and output is caused by border events present in all homogenous detector illuminations. A detailed explanation for this effect is given in Section 6.3.3. The fact that the simulated pulse profiles do not return completely to 0 cts s^{-1} during the off-phase is intentional, since otherwise the low count rate limit of the simulation, described in Section 6.2, would be reached. A small residual of this effect can be seen in the slight downward bending of the red curve at the beginning of the on-phase.

6.3.2 Charge Splitting

One crucial input parameter in the simulation is the size of the charge cloud, which is here specified in terms of σ_{cc} . The size of the charge cloud directly governs the fractions of the pattern distribution. The larger the charge cloud or the smaller the pixel size, the more split events are produced. Another factor which has a direct influence on the detected pattern distribution is the lower energy threshold (LTH). The LTH value for an instrument is typically chosen such that low energy events close to the noise peak are rejected in order to reduce the data load of the later processing electronics stages. If, on the other hand, the LTH is set to a too high

value, an artificial reduction of the energy resolution is introduced. This worsening occurs since the low energy split partner, where only a marginal amount of charge has spilled into the adjacent pixel, will be discarded and the split energy is missing in the reconstruction. Furthermore the detected pattern type changes, e.g., from a triple event to a double event. Figure 6.10 illustrates the effect of the charge cloud size and the LTH on the detected pattern fractions.

To verify the split event generation mechanism and the pattern recombination algorithm, the shift in the pattern distribution for different count rates is investigated. The number of available X-ray sources at IAAT is limited and only three different source-detector distances are easily realizable with the laboratory setup. Therefore a different scheme was used to access a larger number of count rates, which benefits from the halt delay signal of the sequencer, introduced in Sect. 4.5.2. One halt point was set in the readout sequence in order to introduce an additional integration time of length t_{HD} . The programmable sequencer governs the readout process of one single row, therefore t_{HD} is executed for each row of the frame. This line “integration time” concept is contrary to the integration time used in CCD’s where the readout process is without a break. The halt delay was positioned at the end of the row sequence, after the CAMEX sampling has been performed and the signal has been transferred to the “Sample & Hold” register, in order not to perturb the readout and amplification of the detector signal. With the halt delay, the photon flux of the source cannot be changed, but the number of photons per frame can be increased, mimicking a brighter source.

The comparison measurements were performed at a temperature of $T \approx -80^\circ\text{C}$ with the operation voltages and parameters set as described in Sect. 5.1. The duration of the halt delay t_{HD} was adjusted such that frame times of 4, 8, 16, 32, 62 ms were achieved. Since more leakage current is accumulated in the pixel, the determined noise value σ_{N} rises for the measurements with longer frame time from 13.9 eV (2 ms) to 18.9 eV (62 ms), resulting in an increase of the LTH which is specified in terms of σ_{N} .

For the four X-ray sources (1.6, 25, 146, 173 MBq) and 2 distances (89, 199 mm) used, 8 different photon fluxes are possible. For the different settings the detected count rates for the 2 ms frame time vary between 28 and 6600 cts s^{-1} . The measured data were analyzed with the HLLSAS (see Sect.5.2.1), with the primary and secondary event thresholds (PEVTH / SEVTH) set to an identical value of 5σ , since in the simulation code only one LTH is realized. In order to cross check the simulation results with respect to the LTH value, the data sets were additionally analyzed with an 8σ PEVTH / SEVTH.

In the simulation, the time for the row readout $t_{\text{readoutrow}}$ was programmed such that the frame times of the measurements were matched and the LTHs were set to the respective noise values. The simulation input count rate was derived from the

detected count rate for each of the 8 possible settings in a way which is presented in the next section.

For the calculation of the pattern ratios, the energy band was restricted to the range between 5.0–7.0 keV around the Mn K lines. In Fig. 6.11, the “weak” source (1.6 MBq, 199 mm) is plotted which has a homogeneously distributed count rate over all 4096 pixels of $\approx 26 \text{ cts s}^{-1}$. For a frame time of 62 ms this count rate corresponds to $1.6 \text{ cts frame}^{-1}$, a rate which does not cause pile-up. The change of the pattern fractions at the low count rate measurements is thus due to the shift of the LTH, caused by the increased detector noise. As shown in the lower panel of Fig. 6.11, setting the LTH to 8σ shifts the pattern distribution away from the triples and quadruples towards single and doubles events. Both LTH values are equally well modeled by the simulation.

The comparison plots for the stronger X-ray sources are shown in Fig. 6.12. In the case of the 173 MBq source at a distance of 199 mm, the detected count rate is $\approx 1570 \text{ cts s}^{-1}$, resulting in $3.1 \text{ cts frame}^{-1}$ (2 ms) and $97.3 \text{ cts frame}^{-1}$ (62 ms). Comparing the upper panels of Figures 6.11 and 6.12, a shift of the pattern distribution exceeding the LTH shift can be observed for this source-distance configuration. The detected event rates of the 173 MBq source at the shorter distance of 89 mm is $\approx 6660 \text{ cts s}^{-1}$, which leads to $13.3 \text{ cts frame}^{-1}$ and $412.9 \text{ cts frame}^{-1}$ for frame times of 2 ms and 62 ms, respectively. At a count rate of $412.9 \text{ cts frame}^{-1}$ the detector is definitely in pile-up and as shown in the lower panel Fig 6.12 a clear shift in the pattern distribution can be observed, in excess of what can be caused by the effect of LTH.

The systematic offset of the double events between simulation and measurement is caused by an asymmetry in the charge splitting in the used detector matrix. Due to the orientation of the clear-gate/clear structure (Fig. 5.4), the potential within a pixel is not symmetric, thus resulting in a preferred split direction. In the measurements, this effect can best be seen at the double event distribution where instead of a uniform distribution between all 4 possible split directions (see Fig. 6.2), the horizontal split events, i.e., perpendicular to the clear-gate structure account for 56% of the double events compared to 44% for the splits in the clear-gate direction. This asymmetry is present in all types of split events and distorts the pattern distribution.

By modifying the charge cloud size in the simulation, this effect can be modeled to a certain extent, but eventually fails since a symmetric Gaussian shape is assumed in the model. If this asymmetry should still be present in later layouts of the DePFET matrices, it could be modeled in the simulation with an asymmetric Gaussian having two independent σ_{cc} values for each direction.

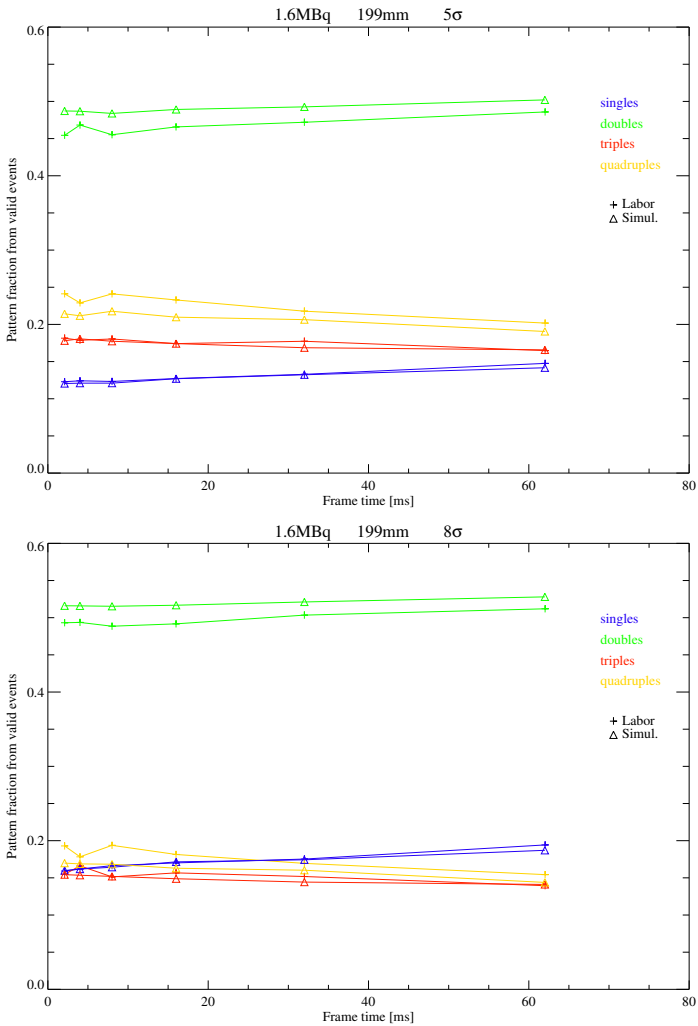


Figure 6.11: Pattern distribution for different frame times of the 1.6 MBq source in a distance of 199 mm with a detected count rate of 26 cts s^{-1} . The pattern fraction is given relative to all valid detected events. In the upper panel, the pattern distribution for the 5σ LTH (75–95 eV) is plotted, in the lower panel for the 8σ LTH (120–152 eV). The observable shift in the pattern distribution is caused by the rise of the LTH.

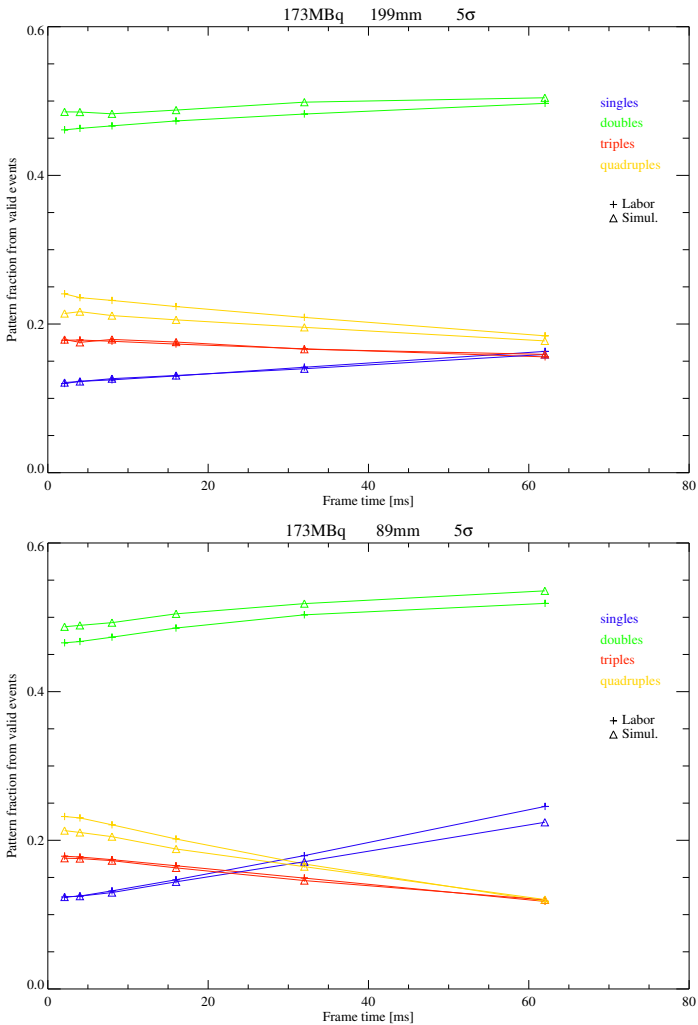


Figure 6.12: Pattern distribution for two configurations with a high count rate. In the upper panel the source (173 MBq, 199 mm, 1570 cts s⁻¹) begins to show pile-up. In the lower panel the split ratio is shown for the same source at a distance of 99 mm (6660 cts s⁻¹), pile-up can clearly be seen. For both panels the LTH was set to 5σ.

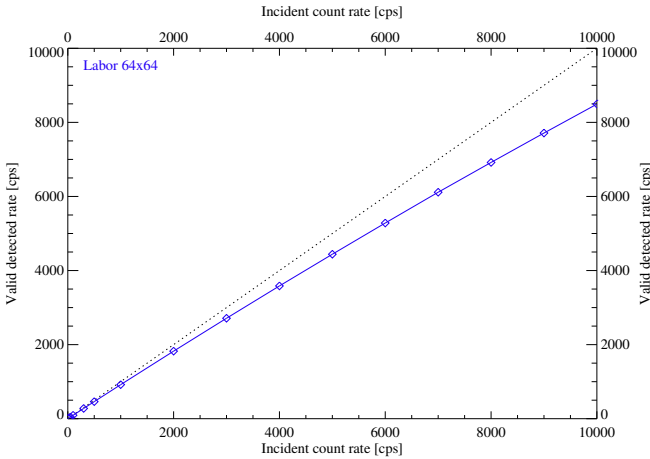


Figure 6.13: Detected valid count rate as function of the input count rate. The dashed line indicates the ideal case, where the output would be identical to the input count rate. The deviation at count rates above 1000 cts s^{-1} is caused by border events and pile-up.

The simulation can reproduce the results obtained in the laboratory with a discrepancy of $\approx 5\%$. The best agreement between the simulation and the measurements was achieved if the σ_{cc} was set to $11 \mu\text{m}$. This value for σ_{cc} lies between the $10 \mu\text{m}$ as quoted by [Strüder \(2000\)](#) and the $12 \mu\text{m}$ reported by [Ulrici et al. \(2005\)](#) for the DePFET matrices.

6.3.3 Pile-up

As next step, the pile-up performance of the simulation code is evaluated by comparing the simulated count rates with laboratory results for different source intensities.

Prior to this evaluation the input count rate for the simulation has to be determined. Therefore the laboratory setup is simulated with a homogenous illumination and the standard frame time of 2 ms for count rates ranging from 1 to $10\,000 \text{ cts s}^{-1}$. The result is shown in Fig. 6.13 where the valid detected count rate is plotted against the input count rate. The deviation from the ideal case, where both rates are identical, is caused by two effects, border events and pile-up. For a homogenous illumination, events at the edge of the detector can be created. These border events

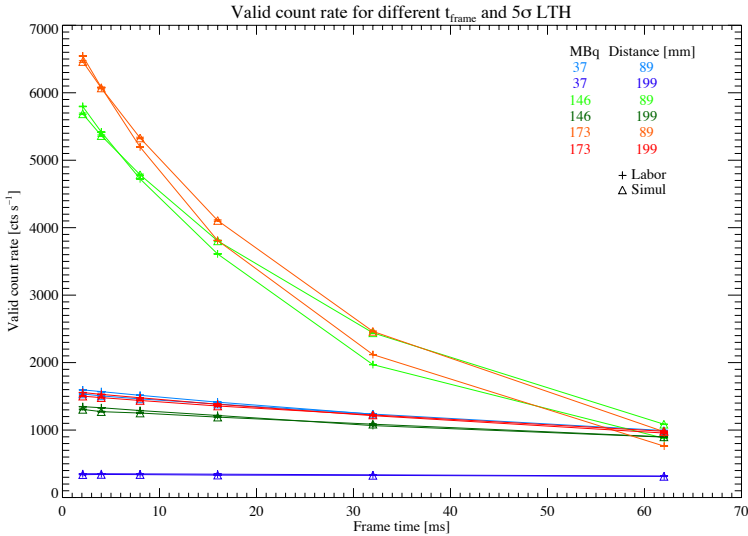


Figure 6.14: Valid detected count rates for different source-distance combinations, if the frame time is increased for the simulation and the laboratory. The decrease of the count rate is caused by pile-up. The simulation reproduces the trends of the laboratory results in principle, but shows a small systematic offset.

are flagged and excluded from the analysis by both the simulation software and the HLLSAS, since charge splitting to the area outside of the structured volume is possible, where the charge is inaccessible for the readout. In the case of the matrix with 64×64 pixel, about $(2 \cdot 64 + 2 \cdot 62)/4096 \approx 6\%$ of the pixels are located directly at the edge. In addition, the software flags events of an inner row as well, when split events to the outermost row are found. For an estimate of the number of affected events, we assume that one side of each pixel ($1/4$) in the second row is adjacent to a border pixel. If only split events are considered (neglecting the 15% single events), another $1/4 \cdot (2 \cdot 62 + 2 \cdot 60)/4096 \approx 1.5\%$ of the events would be identified as a border event in this rough estimate. In the simulation, the input count rate has therefore to be increased by $\approx 7.5\%$ with respect to the detected count rate. At higher count rates, where the loss of detected events cannot be explained solely by the border events anymore, pattern pile-up starts to build up.

The measurements and the simulations presented in the charge splitting section, where with the help of the prolonged frame time a higher photon flux was mimicked, were used for the evaluation of the detector pile-up behavior. When the detected

count rates from the measurements with 2 ms frame time were below 2000 cts s^{-1} the count rate was only increased with the border event percentage of 7.5% in order to derive the simulation input count rates. For measurements exceeding 2000 cts s^{-1} the input count rates were inferred from Fig. 6.13. This has been the case for the 146 MBq and 173 MBq sources at 89 mm distance. From the detected count rates in the laboratory with 5900 and 6660 cts s^{-1} , input count rates of 6600 and 7600 cts s^{-1} have been inferred. To simulated the pile-up behavior, the input count rate has been kept constant and the frame time has been increased again, in order to mimic a source with more counts per frame. The valid detected events for the different source-distance combinations are plotted in Fig. 6.14 for a 5σ LTH.

The simulation describes the behavior of detected count rate and hence the pile-up of the data quite well. The systematic difference visible for the two count rates above 5000 cts s^{-1} is also thought to be due to the asymmetries in the pattern distribution of the currently used matrix which causes more split events than simulation predicts. Nonetheless the trend for the high count rates can clearly be reproduced.

6.3.4 Spectral comparison

For the comparison of spectral performance, a single event spectrum has been extracted from a simulation data set (Fig 6.15). The two Mn K lines can easily be identified, as well as the silicon escape peak at 4.1 keV. The obtained FWHM for the Mn K_α is 134.5 eV and 138.9 eV for the Mn K_β line. This energy resolution is close to the measured values for the back illumination presented in Fig. 5.2, where the energy resolution in terms of FWHM was 133.8 eV and 141.4 eV, respectively. In the laboratory the relative intensities of the Mn K_α :Mn K_β lines were 7.7 : 1, for the simulation a ratio of 7.4 : 1 is obtained. From the number of events recorded under the Gaussian fit of the silicon escape peak, a detection probability of 0.31% can be calculated for a Mn K_α photon to produce a Si K photon which escapes the detector. Considering the background around the escape peak, the calculated probability lies within a reasonable limit of the escape probability specified in the response matrix. For the laboratory back illumination measurement, the escape probability is nearly twice as high (0.57%). This indicates that for a more realistic model of the escape peak effects, like, e.g., the thin dead layers on the backside and the different emission geometries have to be considered.

The fact that the simulated lines look more pronounced is due to the background in the simulation being one order of magnitude lower than the measured one. In the simulation, the background of the single-event spectra only consists of events which originate in the Mn K lines but for which the split partner was either lost in the clear process or was detected in the next frame. In the laboratory, the

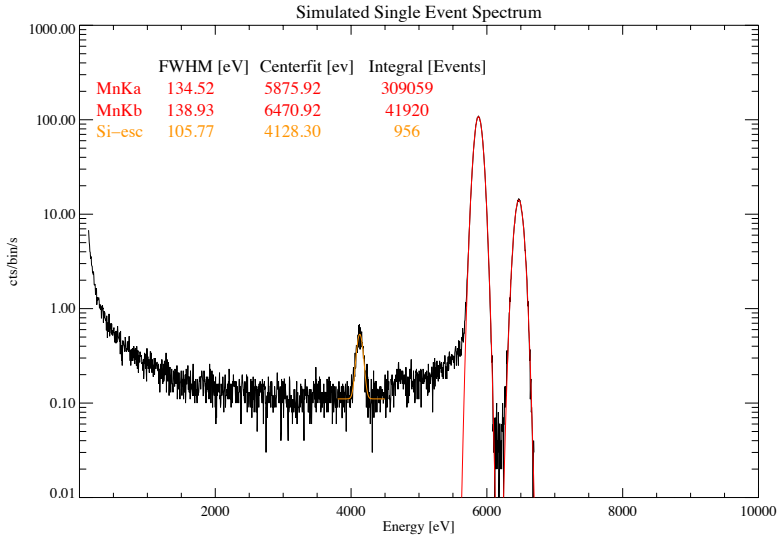


Figure 6.15: Simulated single event spectrum. The Mn-lines and the silicon escape peak are clearly visible. The energy resolution of 134.5 eV FWHM at 5.9 keV is comparable to the laboratory result. The integral value gives the number of events under the Gaussian shape fit curve, resulting in a relative intensity of the Mn K lines of 7.4 : 1.

background additionally has a partial event component. Partial events occur when the photon interaction takes place either close to the interface layer between the aluminum passivation and the p^+ -doped layer of the back contact, or between the back contact layer and the n^- -doped bulk. In these cases, part of the charge cloud is lost when electrons recombine in the p^+ -doped layer. A detailed description of the generation mechanism of partial events and their influence on the spectrum can be found in [Popp et al. \(2000\)](#) and [Kuster et al. \(2005\)](#). In the custom generated response matrix, partial events are not considered and therefore not modeled in the resulting spectrum. For a more realistic response matrix, the charge collection efficiency, which is determined by partial events should be included. This will be done during the pre-phase A study of *IXO* by the Remeis-Sternwarte in Bamberg⁷. The current realization of the response matrix and the event treatment in the code result in a single-event spectrum which reflects all necessary components to a satisfactory degree.

If the simulated and the measured spectra are plotted for the different pattern

⁷Part of the University Erlangen-Nuremberg

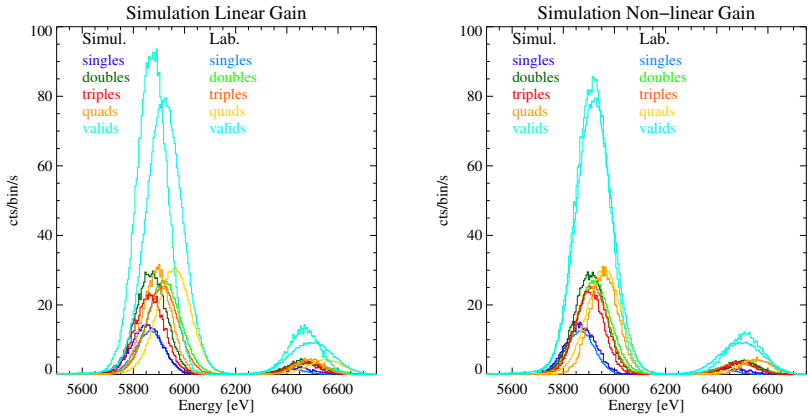


Figure 6.16: Left panel: Comparison of the measured peak positions of the different pattern types to the simulation results where a linear gain was assumed. Right panel: An attempt to model the non-linearity of the CAMEX gain results in a better consistency of simulation and measurement. In both panels forward-backward double events have been excluded, since their charge loss would distort the double-event and the total spectra shown.

types, deviations in the peak positions of the individual components can be seen. In the left panel of Fig. 6.16 for the simulated spectrum all pattern types (single, double, triple, and quadruple events) are detected at the same positions, which correspond to the energies of the Mn K lines. This effect is expected, but stands in contrast to the measurements for which slightly different line energies for each pattern type are detected. This is a direct result of the non-linearity of the CAMEX as described in Section 4.4.1.2, where events with lower energies have a higher gain value. Therefore a double event is recorded with a higher energy than a single event with the same photon energy.

In a short feasibility study we modeled the non-linearity of the CAMEX gain with a skewed parabola, motivated by Fig. 4.11 The result of this proof-of-concept is shown on the right hand side of Fig. 6.16. In this case the non-linearity is just modeled to reproduce the distortion in the spectrum in the energy range from 5–7 keV. Our results indicate that in principle the simulation code allows to include an effect like the non-linearity of the readout electronics, in case this should still be an issue with the next generation of front-end amplifiers (CAMEX and VELA type). Note that, for the doubles events shown in the figures, only the left-right splits are included, since the forward-backward splits suffer from the charge loss described in Sect. 5.2.3 which would distort the spectrum.

6.4 *IXO and Simbol-X simulations*

6.4.1 *Motivation*

The envisaged large collecting area of *IXO* with 3 m^2 at 1.25 keV, necessary for the detection of weak X-ray sources at high redshifts, imposes limitations on the possible observations of Galactic X-ray sources. In the current configuration the Crab nebula has an expected count rate of $\sim 180\,000 \text{ cts s}^{-1}$ on the WFI. A typical Galactic black hole like Cygnus X-1 with a flux of 300 mCrab would still produce a count rate of $\sim 60\,000 \text{ cts s}^{-1}$. For these bright sources pile-up has to be taken into account. However, if a source similar to Cyg X-1, which is located at a distance of 2.5 kpc, would be observed in the next spiral galaxy, the Andromeda nebula ($d = 770 \text{ kpc}$), the count rate would be reduced by $(770/2.5)^2 \sim 10^5$. Such a source would produce a count rate of $\sim 0.6 \text{ cts s}^{-1}$ in *IXO*. This count rate is not high enough to study the source in detail with today's diagnostic tools (e.g., time resolved spectroscopy, time series analysis, energy resolved timing) even with the large collecting area of *IXO*.

It is therefore essential to investigate the instrument performance of the WFI and its window mode, in order to obtain realistic values for the source luminosities at which pile-up will start to deteriorate the measurements. This information is presented in the following and the results emphasize the necessity to accommodate a dedicated instrument with the ability to observe bright Galactic sources with high efficiency, in order to reach the science goals of *IXO*. The realization of such an instrument could be the high time resolution spectrometer (HTRS) which is devoted to the study of phenomena with time variability of the order of $\sim \text{ms}$ and has therefore the capability to deal with high count rates.

The use of the transition edge sensor (TES) for the observation of bright X-ray sources is not discussed within this thesis. For this purpose [Willingale \(2008\)](#) discusses the possibility of a diffusor mounted in front of the TES which reduces the flux by $\sim 38\%$ and redistributes the photons over more pixels, in order to handle higher count rates. Performance simulations of the TES count rate capabilities are currently done by the Remeis-Sternwarte Bamberg.

6.4.2 *IXO pile-up estimations*

For the pile-up study a Crab type spectrum was chosen as input spectrum for the simulation. It serves as template for the energy distribution of a typical Galactic X-ray source.

The spectrum was modeled as an absorbed power-law, taking the canonical values for the Crab as published by [Zombeck \(2007\)](#), with $N_{\text{H}} = 3 \cdot 10^{21} \text{ cm}^{-2}$, power-law index $\Gamma = 2.0$, and a normalization of 10. The background is neglected since the simulation focuses on the determination of the high count rate abilities,

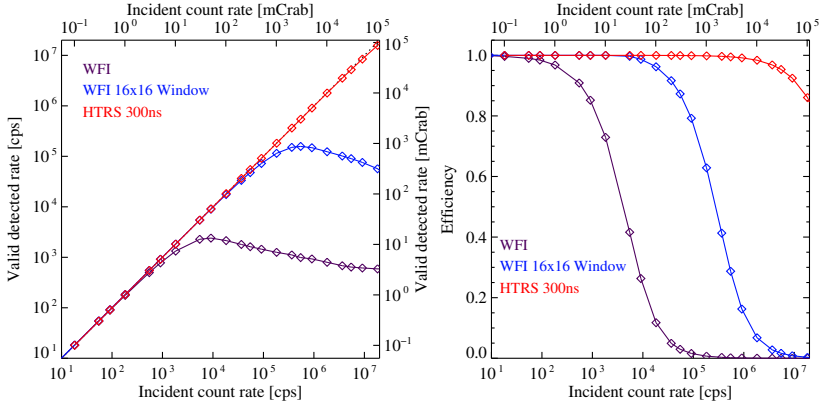


Figure 6.17: Efficiencies of the *IXO* baseline detectors. Left: Detected count rates as function of the input count rate, given in units of counts per second and in mCrab. Right: Detector efficiencies for different input count rates. The detectors are considered to be strongly piled-up when the efficiency drops below 0.9.

where we assume that the spectrum is completely source dominated. In the simulation code, $\sigma_{cc} = 11 \mu\text{m}$ was used for the *IXO* WFI and its window modes. Although the planned pixel size of $100 \mu\text{m}$ is somewhat larger than for the matrix actually used in the laboratory, no significant change of the charge cloud size is expected. This is based on the assumption that through one additional drift-ring, the potential course inside each pixel will not be strongly altered.

The lower energy threshold (LTH) of 150 eV and a constant source count rate were set. For the spatial event distribution on the WFI and its window mode the detector was illuminated by a PSF with $5''$ HPD. For the HRTS, the baseline configuration as described in Sect. 6.2.2 with a dead time of 300 ns and the relative illumination coefficients shown in Fig. 6.5 were used.

In the simulations, the capabilities of the instruments are described through their efficiency, which is here defined as the ratio of the valid detected count rate to the incident count rate on the focal plane instrument. With this definition the filters and entrance windows are included in the instrument description. This means, that even for low count rates the efficiencies of some detectors always stay below 100%. For the current mirror configuration of *IXO*, the Crab produces $180\,000 \text{ cts s}^{-1}$ on the focal plane instruments. The count rates in the plots are usually given in units of counts per second and additionally in mCrab. This approach allows, should the mirror assembly change, that the plots can be adjusted by a simple rescaling

(neglecting hereby second order effects like, e.g., a different PSF).

Source intensities from 10^1 – 10^7 cts s^{-1} , which correspond to a range of 0.1 mCrab up to 100 Crab, have been simulated for the WFI full frame mode, the window mode, and the HTRS. The results are shown in Fig. 6.17. If moderate pile-up is defined as a detector efficiency of <95% and strong pile-up as an efficiency <90%, the WFI operation range is limited to source fluxes lower than 1 mCrab. With the window mode, the observation capabilities can be shifted towards higher count rates through the faster readout, but the observation is limited when strong pile-up is reached at 100–200 mCrab. For the HTRS, the pile-up starts at 10 Crab and becomes moderate at 30 Crab. These efficiency studies emphasize the need for a dedicated instrument able to observe X-ray sources with fluxes above 100 mCrab. The results clearly show that WFI is not suitable for observations of Galactic X-ray sources. The usage of a window mode is limited to observe only moderate bright sources without degradation of the detector response.

Fig. 6.18 illustrates the shift in the pattern fractions at higher rates, the fractions are drawn relative to all detected patterns. The pattern fraction visible at low count rates is given with 57% single, 38% double, 3% triples and 2% quadruple events. In this case, single events dominate the pattern distribution in contrast to the measurements presented in the previous section with 13% single, 49% double, 17% triple, and 21% quadruple events. This shift is caused to a smaller extent by the different pixel sizes ($75\mu\text{m} \leftrightarrow 100\mu\text{m}$), but the main reasons for the different pattern distribution lie in the shape of the input spectrum and the different LTHs. In the case of the laboratory measurements and their simulations, the detector is illuminated with a radioactive source which produces a line spectrum. In contrast the Crab spectrum is modeled by a continuous spectrum with a broad peak and a maximal count rate at ~ 1 keV. The broad peak which extends down to 500 eV causes, in combination with the 150 eV LTH, a suppression of the double events in favor of the single events, in contrast to the measurements. The pattern distribution obtained in the laboratory can therefore not be applied in a straight forward manner to continuous spectra.

Figure 6.19 shows the deformation of the PSF through pile-up for the window mode. For the operation of the 16×16 pixel window mode, the scientifically useable events can only be extracted from the inner 14×14 pixel. Events in the outermost pixels have to be discarded since they can contain split events to and from the outside of the window such that the photon energy cannot be unambiguously reconstructed. The count rate in the outer rows is therefore always set to zero. For the window mode, above a count rate of 0.1 Crab pattern pile-up starts to distort the shape of the PSF. In the extreme case of a 3 Crab illumination, a dip in the center of the PSF evolves. This figure also illustrates the fact that, as optics become better and the HPD gets smaller, more photons are focused into a smaller number

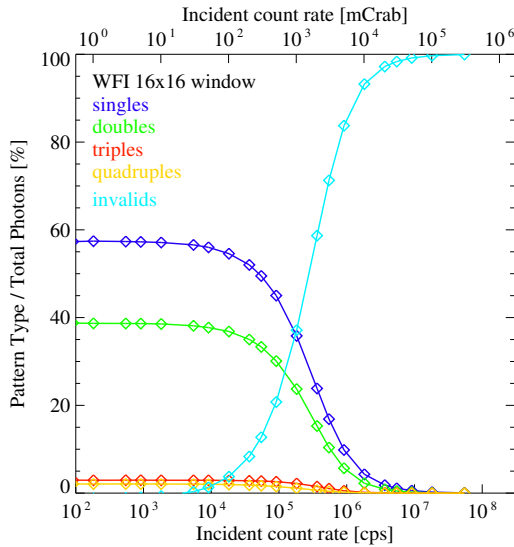


Figure 6.18: Illustration of the shift in the pattern distributions due to the invalid events, simulated for the *IXO* window mode. The pattern fractions are in this case plotted relative to all simulated photons. At count rates above 50 mCrab invalid events start to be recognizable and at 2 Crab the majority of the incident photons are detected in invalid patterns.

of pixels and therefore pile-up becomes more prominent.

Figure 6.19 also shows that if the region-of-interest, in this case chosen as the window mode, is too small for the mirror HPD, variations in the spatial position of the PSF center can cause fluctuations in the detected count rate.

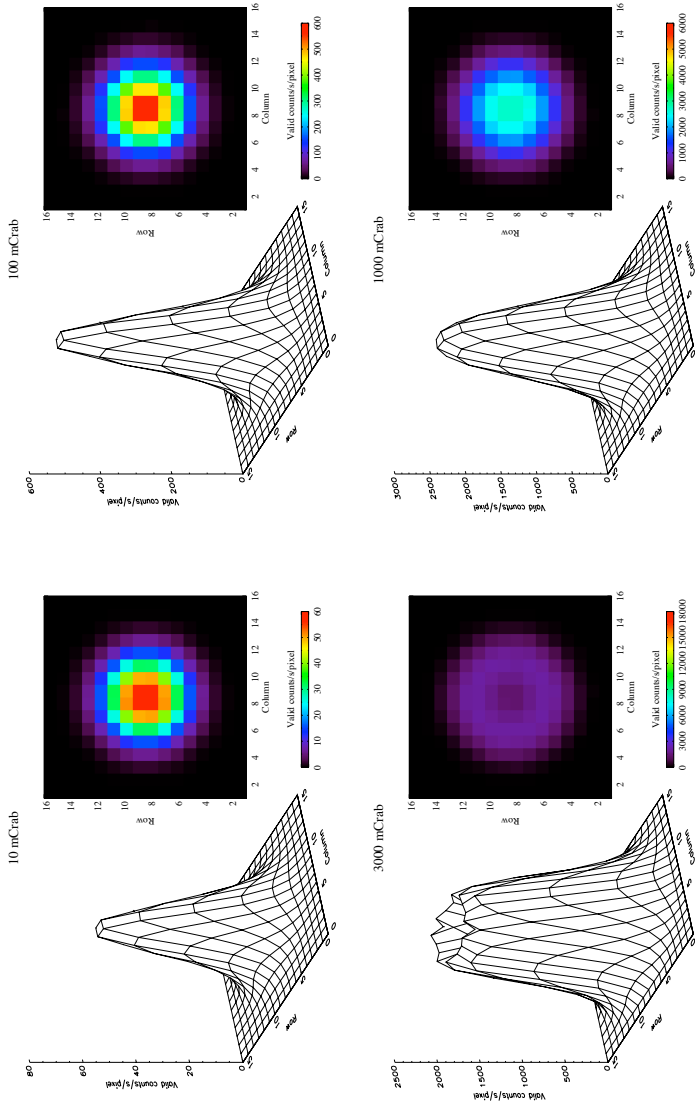


Figure 6.19: Illustration of the PSF deformation caused by pile-up. Shown in clockwise direction, starting at the upper left corner, are the PSFs for source intensities of 0.01, 0.1, 1.0 and 3.0 Crab, as detected in the 16×16 window mode. The color bar is normalized to the expected peak flux in absence of pile-up and is given in units of valid counts $s^{-1} \text{ pixel}^{-1}$.

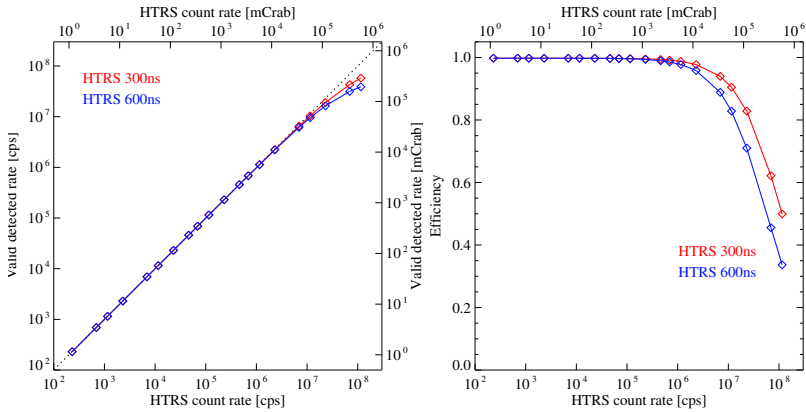


Figure 6.20: Comparison of the HTRS efficiencies between the SDDs with the planned 300 ns and the fall-back option with 600 ns dead time. Above 1 Crab, the efficiency for the two options begin to differ, but even with the fall back option, the efficiency is $>90\%$ for count rates up to 10 Crab.

In the simulation of the HTRS several simplifying assumptions are made. In the case of the HTRS the readout of the events is triggered by the photon arrival. After the photon hit, the readout process of the pixel is assumed to be insensitive to further photon arrivals, until the end of the dead time. This simplification is needed since no decision on the analog and digital front-end electronics has yet been made. Therefore, the correct handling of events which enter the detector during the shaping process of the previous photon cannot be modeled in detail. The second simplification is that for the 37 pixels of the HTRS, no split events are created, all detected events are singles. This assumption is supported by the fact that the individual pixels have an area of 4 mm^2 , which reduces the probability of a photon hit at the detector edge which can create a split event. Split events can be avoided by an aluminum blocking filter at the edges of each SDD. A blocking filter width of $50\text{--}80 \mu\text{m}$ at the SDD edges reduces the efficiency of the detector by $5\text{--}8\%$. A trade-off between the efficiency loss on one hand and the possibility of split events and pattern pile-up, together with the need for an event recombination logic on the other hand has still to be made.

In Figure 6.20, the HTRS has been modeled with the baseline dead time of 300 ns which is based upon a 75 ns shaping time, and the fall-back option with 600 ns dead time (150 ns shaping time). Both options start to differ around 1 Crab, with the 600 ns dead time obviously having a stronger efficiency decrease, but still

sufficiently large to observe sources up to 10 Crab with moderate pile-up. The option with the blocking filter would be drawn in this plot with a constant 92–95% efficiency even at low count rates.

6.4.3 Simbol-X pile-up estimations

Since the low energy detector (LED) of *Simbol-X* is in principle the same detector as the *IXO* WFI except for the larger pixel size, simulations were performed in order to estimate its pile-up behavior. These simulations have been carried out for the full frame (128×128 pixel) and the window mode (32×128 pixel).

In the case of the $625 \mu\text{m}$ pixel size, drift rings are necessary to collect the charge that is generated within the depleted volume of the pixel into the central DePFET. The potential inside the depleted bulk at the edges of the pixels is modified through the negative biasing voltage of the drift rings. The effective potential created together with the backside voltage is therefore not as pronounced as in the case of the small pixels, which results in a larger dispersion of the charge cloud. The simulation should therefore not be performed with the standard charge cloud size of $\sigma_{\text{cc}} = 11 \mu\text{m}$.

To estimate the charge cloud size, simulations using the baseline *Simbol-X* laboratory matrices with pixel sizes of $500 \times 500 \mu\text{m}^2$ were performed. The Mn K line spectrum obtained with the custom created laboratory response was used as input. A low count rate of 1 cts s^{-1} was set in order not to cause pile-up. The LTH was set to a value of 90 eV, which corresponds to a system noise of 18 eV ($5\sigma_{\text{N}}$ threshold). The size of the charge cloud was varied between $12 \mu\text{m}$ and $22 \mu\text{m}$ in order to reproduce the reported pattern distribution by [Lechner et al. \(2008\)](#) with 63% single and 30% double events. Through the large pixel size ($500 \mu\text{m}$) as compared to the charge cloud size ($\sim 10\text{--}20 \mu\text{m}$), the dependence of the pattern distribution on the charge cloud size is not as pronounced as in the case of the $75 \mu\text{m}$ pixel. The dependence of the pattern fraction on the LTH is also not as prominent as in the case of the smaller pixels. Values for the charge cloud between $16\text{--}20 \mu\text{m}$ and LTHs between $75\text{--}100 \text{ eV}$, resulted in pattern distributions which are of the order of $\sim 70\%$ single and $\sim 30\%$ double events. For the simulations therefore $\sigma_{\text{cc}} = 18 \mu\text{m}$ was used.

For the count rate simulation, a Crab type spectrum with the same parameters as used for *IXO* was set up in XSPEC with the *Simbol-X* response matrix introduced in Section 6.2.2. For the *Simbol-X* mirror-detector combination the Crab has a count rate of 8800 cts s^{-1} on the LED. The full frame and the window mode have been illuminated with constant count rates which correspond to source intensities between 0.1 mCrab and 300 Crab and with a $18''$ HPD PSF. The LTH value was set to 150 eV.

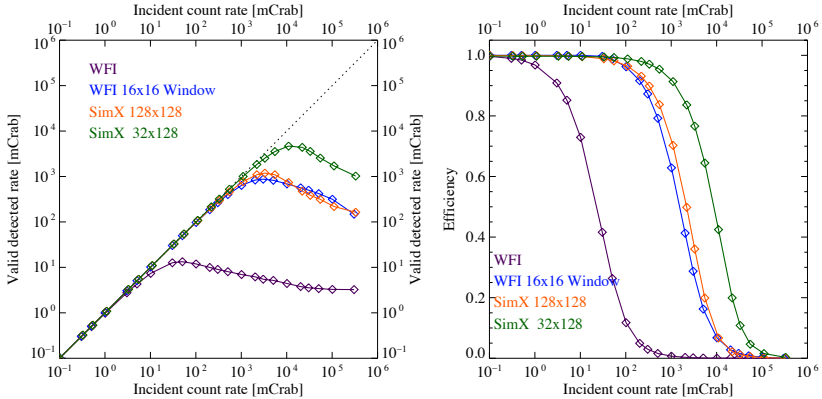


Figure 6.21: Comparison of the count rates and efficiencies of the *IXO* WFI and window mode and the *Simbol-X* modes. Both satellites are complementary and would allow to observe X-ray sources with intensities ranging from 0.001 to 1 Crab with their main instrumentation.

The results the *Simbol-X* simulation are shown in Fig 6.21 together with the results of the *IXO* simulation. In order to compare the instrument sets of the two missions, they are plotted scaled to their input count rate in mCrab. As can be seen, both satellites would have been complementary and would have allowed to observe the X-ray sky, from faint sources up to count rates corresponding to intensities of 1–2 Crab, with high efficiency and a temporal resolution of the order of 16–32 μ s. *Simbol-X* hereby “profits” from the smaller number of LED pixels and the hence resulting shorter frame time as well as from the lower angular resolution of the mirrors as compared to *IXO*.

6.5 Simulation of astrophysical X-ray sources

In the previous sections it has been shown that the event handling of the simulation code correctly reproduces the pattern distribution and the pile-up of the measurements. It has also been shown that the time and energy resolution of the simulations are comparable to the values obtained in the laboratory. To illustrate the possibilities and limitations of the planned *IXO* instrumentation the simulations are extended in this section to astrophysical X-ray sources.

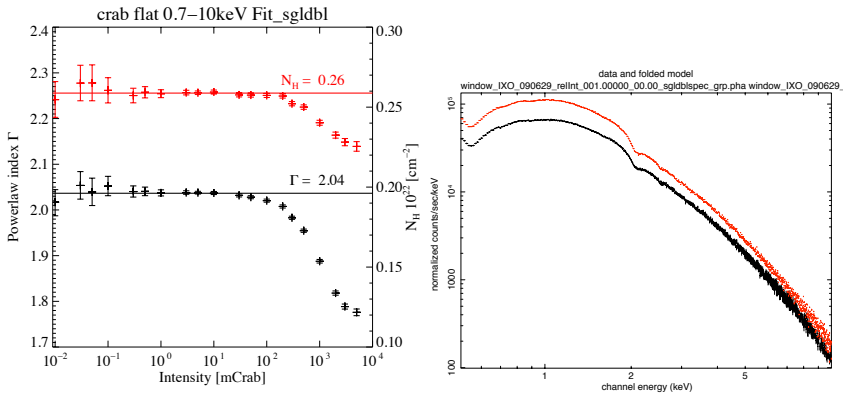


Figure 6.22: Left panel: Fit results of the N_{H} and the power-law index Γ for a combined single-double event spectrum of the Crab for different source intensities (window mode simulation). The error bars indicate the 90% confidence level. Above 100 mCrab, pile-up causes more absorption and a harder spectrum. Note, the error bars at low count rates are determined by low statistics. For low count rates the possible observation time is limited by the memory handling of the code. Right panel: Spectrum with a 1 Crab intensity drawn in black and a 10 mCrab spectrum, rescaled to 1 Crab drawn in red.

6.5.1 The Crab

Probably one of the most observed X-ray sources is the Crab, which is also frequently used as standard candle by X-ray satellites to calibrate their instrument set. An overview of the deduced parameters for the Crab pulsar with different instruments is given by, e.g., [Kirsch et al. \(2005\)](#). As first astrophysical object the Crab is therefore simulated. The input spectrum is identical to the one of the count rate simulations, an absorbed power-law with $N_{\text{H}} = 3 \cdot 10^{21} \text{ cm}^{-2}$, $\Gamma = 2.0$, and the flux at 1 keV is $10 \text{ ph cm}^{-2} \text{ s}^{-1} \text{ keV}^{-1}$ ([Zombeck 2007](#)).

Instead of a constant photon flux we take the pulse profile measured by [Kirsch \(2003\)](#) with *XMM-Newton* EPIC-pn as basis of the light curve (see Fig. 6.25). This pulse profile is scaled such that the average count rate of the profile matches the requested simulation photon flux. The peaks of the pulse profile have therefore a count rate which is ~ 2.5 higher than the average. From this pulse profile, the light curve is created and fed into the simulation.

The input count rates were varied from 0.01 mCrab to 5 Crab for the simulation of the *IXO* window mode. From the event list, spectra for the different pattern types were extracted and regrouped such that each group contained at least 100

counts. The spectra were then fitted with XSPEC and the energy range was limited to 0.7–10 keV. The fit resulted in a power-law index $\Gamma \approx 2.3$ for the single event and $\Gamma \approx 1.8$ for the double event spectra. Both power-law indices differ from the input value of $\Gamma = 2$. Only when the single and double events are combined into one spectrum, the fit results in $\Gamma = 2.04$, as shown in the left panel of Fig. 6.22. In this figure, the evolution of the power-law index Γ and the absorption N_{H} in dependence of the source intensity can be seen. Above 100 mCrab, the spectrum begins to harden. The N_{H} value decreases and the slope of the power-law flattens through the redistribution of the low energy flux towards higher energies.

In the right panel of Fig. 6.22, two window mode spectra are shown. For the spectrum drawn in black the average source intensity was 1 Crab. The red spectrum was obtained with a 10 mCrab source intensity and has been rescaled by a factor of 100, to mimic a 1 Crab spectrum without pile-up. Again, the stronger absorption and the harder spectral index of the piled-up 1 Crab spectrum can clearly be seen.

The lower limit of 0.7 keV was set because below this energy the deviations between the measured spectra and the response matrix are too large and would distort the fit. The behavior of the response matrix indicates that it is based on the EPIC-pn response and incorporates the pattern distribution of the pn-CCD, which could explain the different Γ values of the single and double event spectra. Therefore in the interpretation of the spectral fit results of the single and double event spectra caution has to be taken. Below 0.7 keV, the combined single-double event spectrum exhibits a redistribution of events towards lower energies which can be explained by inter-frame splits.

The inter-frame splits have their origin in the readout strategy of the DePFET matrices. When an event occurs in the row which is currently read out charge splitting into the neighboring rows can occur. If the neighboring row has been read just before, the event will be split over two frames, hence the name inter-frame split. This would cause, e.g., a double event to be detected as two single events in two subsequent frames. The occurrence of inter-frame splits depends on the time of the photon hit in the pixel (before/during the signal sampling, during the clear process, or during the baseline sampling), and whether the charge splitting occurs in or opposite to the readout direction.

The way in which the clear process is implemented in the simulation biases the inter-frame split occurrence. The signal sampling time is omitted and the baseline sampling duration is prolonged (see Fig. 6.3), causing more events to fall in this time span that will be read out in the next frame. Events occurring during the baseline sampling time which split their charge in the readout direction are thus separated into two frames. If we assume that the signal and baseline sampling usually have the same duration, we over estimate the inter-frame splits by a factor of 2 with the current implementation. Events which occur during the

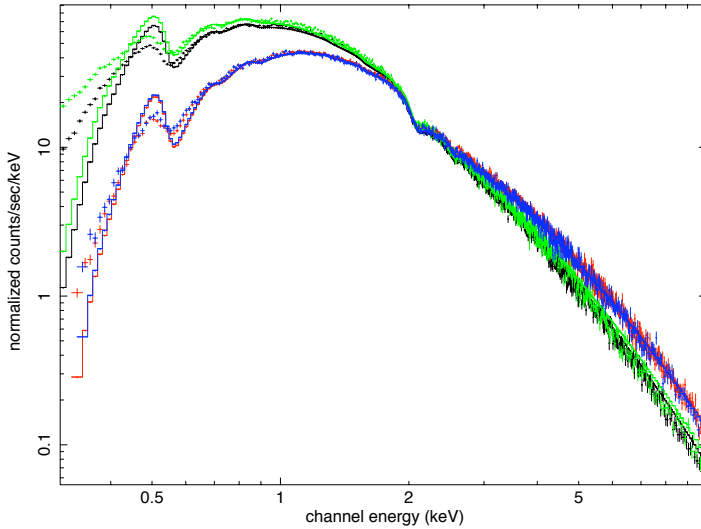


Figure 6.23: Measured Crab spectra and the fitted models for different patterns and instruments. Single events are drawn in black for the WFI and in green for the window mode. Double events are plotted in red for the WFI and in blue for the window mode. The deviations between the model and the spectrum at low energies are created by inter-frame splits.

signal sampling and create a split event opposite to the readout direction, create an inter-frame split as well. But in this case, the split event partner in the row currently read is detected with a PHA value below the noise peak of the detector and will therefore be discarded. The remaining split event will then be read out in the next frame with an energy deficit. Under the premise of an equal probability to create a forward or a backward split and for equal signal and baseline sampling durations, this should balance the over-estimation.

In Figure 6.23, the Crab spectrum is shown for an intensity of 0.1 mCrab, simulated for both the WFI and the window mode, subdivided in single and double event spectra. For the single event spectra the deviations are larger than for the double event spectra. This is caused by the fact that in the pattern distribution more double events exist than triple or quadruple events which are needed to create double events by inter-frame splitting. The frame time is significantly shorter for the window-mode than for the WFI ($16\mu\text{s}$ vs. 1 ms), the probability to create an inter-frame split is therefore higher in the window mode. This effect can be observed when the window mode and the WFI single event spectra are compared.

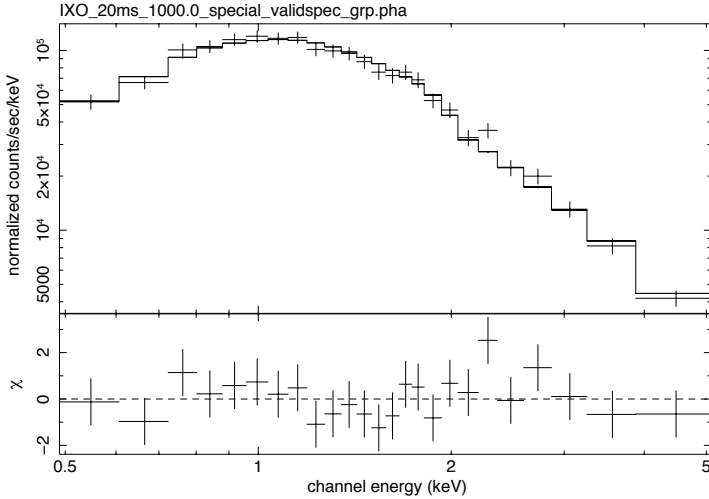


Figure 6.24: This Crab spectrum was obtained in 20 ms with the HTRS and illustrates the possibility to perform time resolved spectroscopy.

For the creation of a more realistic response matrix, the effect of inter-frame splits has to be included. Further a more realistic timing of the signal and baseline sampling has to be implemented in the simulation code.

Through the high count rate efficiency of the HTRS, time resolved spectroscopy in the order of tens of ms is possible for bright galactic X-ray sources. This is illustrated by the spectrum shown in Fig. 6.24 which was obtained for a 20 ms long observation of the Crab. Rough values for the power-law index $\Gamma = 2.1 \pm 0.12$ and the absorption $N_{\text{H}} = 3.2(\pm 0.3) \cdot 10^{21}$ can be already estimated from these data.

As closing summary of the Crab simulations, in Fig. 6.25 the simulated light curves for four consecutive periods are shown for the valid detected count rates of the different IXO instruments (HTRS, WFI, and window mode).

6.5.2 Neutron star eclipses

One interesting example of possible observations which can be undertaken with IXO is the study of neutron star eclipses. In the simulation we model an eclipsing X-ray binary system in which the neutron is obscured by the companion star. We assume an eclipse ingress time of 50 ms, which is inferred from a neutron star radius of 10 km and an orbital velocity of 200 km s^{-1} . The moderately bright 100 mCrab source intensity results in an IXO count rate of $18\,000 \text{ cts s}^{-1}$. The

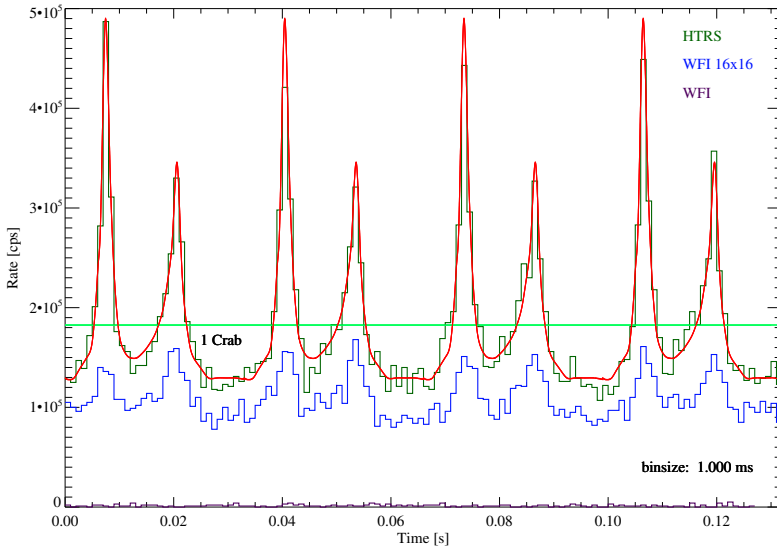


Figure 6.25: Detected Crab light curves of the *IXO* instruments. The Crab input light curve is drawn in red, the horizontal green line indicates the average 1 Crab count rate ($180\,000\text{ cts s}^{-1}$). The valid detected count rate is plotted in dark green for the HTRS, in blue for the window mode, and in violet for the WFI (at the very bottom of the figure). The HTRS is able to sample the light curve with high precision, the window mode shows a reduced count rate where the peaks are only indicated, and the WFI is completely saturated.

ingress itself is linearly approximated and the source intensity during the eclipse drops to $11\,000\text{ cts s}^{-1}$. The non-vanishing count rate during the eclipse accounts for the existence of a hot corona around the neutron star and its accretion disk. The observations of neutron star eclipses allow to study the inner part of the corona, and to deduce from the shape of the ingress geometrical properties of the accretion disk or the neutron star radius. Figure 6.26 shows the obtained light curves for 10 simulated eclipses.

6.5.3 X-ray bursts

As last astrophysical application we present the simulation of an X-ray burst. In many accreting low mass X-ray binary systems with a neutron star as compact object, regular rises of the X-ray luminosity can be observed with a recurrence time of the order of hours to days. The light curves of these so-called X-ray bursts

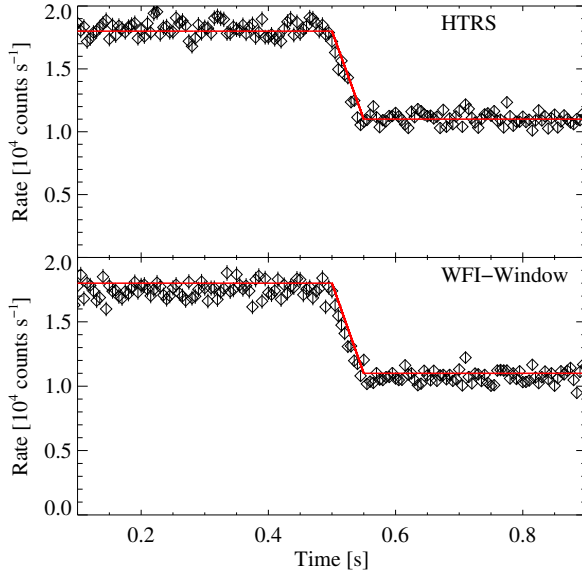


Figure 6.26: Light curve of an eclipsing neutron star. For a 100 mCrab bright neutron star, 10 eclipses have been simulated with the HTRS and the window mode of the WFI. The window mode is operated at its limit, a slight decrease of the “measured” count rate is already visible.

exhibit a fast rise (\sim sec) with an exponential decay (FRED) behavior. For a review of X-ray bursts see, e.g., [Psaltis \(2006\)](#) and [Strohmayer & Bildsten \(2006\)](#).

The origin of these X-ray bursts lies in the matter (H/He) which is accreted from the companion star and is accumulated on the neutron star surface. If sufficient material has been accreted, the base of the H/He-layer becomes dense and hot enough for the CNO-cycle burning to set in. The CNO-cycle is highly temperature dependent and eventually results in a thermonuclear explosion where all available fuel is consumed in a few seconds ([Galloway et al. 2008](#)). The spectral shape of the burst can be described by a blackbody with a temperature kT_{BB} of 2–3 keV, created by an optically thick plasma in thermodynamical equilibrium.

During the burst, the X-ray flux stays approximately constant while the measured blackbody temperature shows a dip ([Strohmayer & Bildsten 2006](#)). This phenomenon occurs when the suddenly increasing photon flux reaches the Eddington luminosity L_{Edd} , which is defined as equilibrium between the outward directed

radiation pressure and the gravitational force. When L_{Edd} is reached the radiation pressure lifts the photospheric layer of the neutron star surface (fast rise) which then falls slowly back to the surface (exponential decay). The radius R can be calculated from

$$L = 4\pi R^2 \sigma T^4 \quad (6.8)$$

where σ is the Stefan-Boltzmann constant. If the distance to the object is known the luminosity L can be inferred from the measured flux. In these photospheric radius expansion (PRE) bursts the luminosity is assumed to reach L_{Edd} . Since L_{Edd} depends on the mass and the radius of the neutron star, they can be calculated from the burst luminosity. With the PRE bursts, it is therefore even possible to estimate the distance to the burst with an accuracy of $\sim 15\%$ as shown by [Kuulkers et al. \(2003\)](#).

The simulation is based on the values reported by [Galloway et al. \(2008\)](#) for the X-ray burster KS 1731–26, measured with *RXTE* in February 1999. For the 20 s duration of the burst, blackbody spectra with an 0.1 s time resolution were created from the measured kT_{BB} values. The luminosity was rescaled with the reported source distance of 7.2 kpc in order to calculate the count rate for the HTRS. An observation was then simulated and from the obtained event lists, spectra were created for each time bin and fitted in *XSPEC* with a blackbody spectrum.

The results of the simulation reproduce all existing features and model the input data quite well (Fig. 6.27). In the peak, the 90% confidence level of the blackbody temperature kT_{BB} is ± 0.1 keV and $\pm 2.6 \cdot 10^{37}$ erg s $^{-1}$ for the luminosity. In the tail the uncertainty of kT_{BB} is ± 0.08 keV and $\pm 2.6 \cdot 10^{36}$ erg s $^{-1}$ for the luminosity.

The higher count rate of the *IXO* HTRS and the consequentially better signal-to-noise ratio (SNR), allows a finer time resolved analysis of the X-ray bursts compared to *RXTE*, and enables observations of even fainter X-ray bursts.

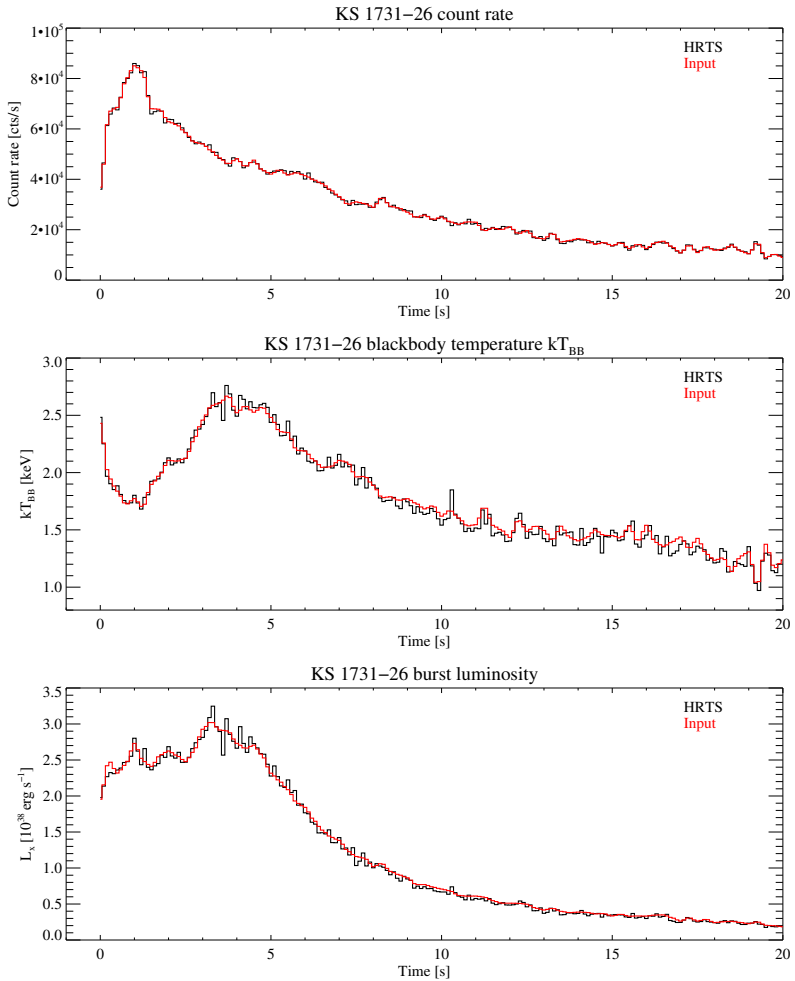


Figure 6.27: X-ray burst of KS 1731-26, red shows the simulation input, black corresponds to the simulated HTRTS results. In the top panel, the detected count rate is shown. The middle panel shows the blackbody temperature kT_{BB} with the temperature dip caused by the radius expansion (0–4 sec). In the bottom panel, the X-ray luminosity in units of $10^{38} \text{ erg s}^{-1}$ is shown with the fast rise and the exponential decay. During the first 5 s, the “flat” top where the luminosity stays approximately constant can be seen.

Summary and Outlook

“Time is what prevents everything from happening at once.”

[John Archibald Wheeler]

7.1 *Summary and Conclusions*

The focus of this thesis is on silicon-based detectors operating in the energy band of 0.1–20 keV on-board the next generation of large aperture X-ray satellites. In the course of the work done, a test setup to operate and characterize prototypes of the DePFET detector was built at the Institut für Astronomie und Astrophysik of the University Tübingen (IAAT) in close collaboration with the Max-Planck-Institut Halbleiterlabor (MPI HLL). The laboratory setup is fully functional and measurements have shown that the DePFET matrices can be operated at IAAT with an energy resolution of ~ 130 eV FWHM at 6 keV. For the currently used source-center matrix, it was shown that charge loss underneath the clear structure is still an open issue. Furthermore, measurements of the temperature dependence of the offset indicate that, for the satellite based operation of the DePFETs, the temperature variations should not exceed 0.2 K.

The experience gained by building the setup and operating the DePFET matrix was essential for the development of a code to simulate the performance of the detector. The focus of the code development was on the correct implementation of the event handling, i.e., a realistic model of the temporal and spatial photon distribution, of the readout cycle, of the charge splitting and event recombination.

Our simulations were validated on the laboratory prototype. Measurements with time variable sources can be reproduced and the correct pulse periods and profiles are detected for sources with high count rates. The accuracy of the timing behavior in the code is only limited towards low count rates by the implemented

photon generation algorithm, but works well for bright sources. Assuming a charge cloud size of $\sigma_{cc} = 11 \mu\text{m}$, the code reproduces accurately the charge splitting of the detector and the shifts in the pattern distribution caused by different lower thresholds and by pile-up. Simulation results have also shown that the count rate decrease caused by pattern pile-up can be reproduced. A small systematic offset was found for the fraction of double events in the pattern distribution, as well as for the count rate behavior. This deviation originates in an asymmetric split distribution of the DePFET matrix, caused by the asymmetric pixel layout. Spectral features detected in the laboratory could also be reproduced with the custom created response matrix to a satisfying degree.

After the successful code validation, we expanded the scope of the simulation and modeled the silicon based detectors of the *International X-ray Observatory*. At a first glance, the short frame times of the WFI and its window mode lead to the false impression that the observation of bright X-ray sources should not pose a problem to *IXO*. But due to the large increase in effective area of *IXO* as compared to current missions this impression is misleading. The simulation results clearly show that with the WFI full frame mode only sources with a flux less than 1 mCrab can be observed without deterioration of the detector performance through pile-up. The WFI window mode allows, with its considerably shorter frame time the observation of sources with fluxes up to ~ 100 mCrab with moderate pile-up. In the current instrument set of *IXO*, the HTRS is the only detector which can be used with high efficiency for sources brighter than 1 Crab. Our results are being used by the *IXO* consortium to further develop the scientific payload of the mission.

The simulation of time variable astrophysical sources like, e.g., the Crab or the X-ray Burster KS 1731–26 illustrate the possibilities offered by a large aperture X-ray mission like *IXO*. Time resolved spectroscopy in the millisecond range and energy resolved timing becomes possible with an energy resolution which *RXTE* cannot provide.

7.2 Outlook

The laboratory setup will be used to continue characterizing DePFET prototypes, as new devices are currently developed by the MPI HLL with, e.g., improved front-end amplifiers like the VELA-Chip or a new CAMEX version. Later on, the laboratory setup can be modified to host larger DePFET prototypes with an increased number of pixels and to test devices with two readout directions. At IAAT, a demonstration model of a new sequencer and an Event Preprocessor are being developed in the course of the *Simbol-X* mission activity. This development is nearly completed and extensive testing and verification are needed. Albeit the

fact that *Simbol-X* has been canceled, the new electronics are valuable for the operation of the current laboratory setup and the testing of new detector prototypes for *IXO*.

The next step for the simulations would be the generation of realistic light curves for fast time variable astrophysical sources, like quasi-periodic oscillations or burst oscillations. These studies would further strengthen the science case for *IXO* and show the need for a dedicated instrument to perform fast timing studies.

As in every software project, there are always things to improve and new features to include. The simulation code can easily be modified if new detector parameters are needed or mission parameters are redefined. The verification of the code shows that the basic work is done but detail improvements can be made by:

- a more realistic model of the baseline and signal sampling, e.g., through the approximation by two linear ramps
- a new photon generation algorithm for the correct handling of low count rates
- an asymmetric Gaussian shape for the charge cloud in order to model the asymmetries in the split distribution
- a King profile for the point-spread function, instead of the Gaussian shape
- including partial events to model the background in a correct manner

The efforts to evaluate the performance of the *IXO* instrumentation will continue during the various development phases of the mission. More specifically, parts and concepts of the detector simulation developed within the framework of this thesis are planned to enter the *IXO* spacecraft simulator, in close collaboration with the Remeis-Sternwarte Bamberg.

Bibliography

- ApPEC. 2007, Status and Perspective of Astroparticle Physics in Europe - Roadmap Phase 1
- Arnaud, K. A. 1996, in *Astronomical Society of the Pacific Conference Series*, Vol. 101, *Astronomical Data Analysis Software and Systems V*, ed. G. H. Jacoby & J. Barnes, 17
- Arnaud, M., Bohringer, H., Jones, C., et al. 2009, *Astronomy*, 2010, 4
- Aschenbach, B. 1985, *Reports of Progress in Physics*, 48, 579
- ASTRONET. 2007, *A Science Vision for European Astronomy*
- Ballet, J. 1999, *A&AS*, 135, 371
- Barret, D., Belloni, T., Bhattacharyya, S., et al. 2008, in *Society of Photo-Optical Instrumentation Engineers (SPIE) Conference Series*, Vol. 7011
- Bavdaz, M., Lumb, D., Peacock, A., Beijersbergen, M., & Kraft, S. 2004, in *Society of Photo-Optical Instrumentation Engineers (SPIE) Conference Series*, Vol. 5488, in press
- Bellazzini, R., Angelini, F., Baldini, L., et al. 2006, *Nucl. Instrum. Methods Phys. Res., Sect. A*, 560, 425
- Benlloch, S., Wilms, J., Edelson, R., Yaqoob, T., & Staubert, R. 2001, *Astrophys. J., Lett.*, 562, L121
- Boella, G., Butler, R. C., Perola, G. C., et al. 1997, *A&AS*, 122, 299
- Bombelli, L., Fiorini, C., Porro, M., Herrmann, S., & Wolfel, S. 2007, *IEEE Transactions on Nuclear Science*, 54, 1359
- Bookbinder, J. 2009, *The International X-ray Observatory*
- Bookbinder, J., Smith, R., Hornschemeier, A., et al. 2008, in *Society of Photo-Optical Instrumentation Engineers (SPIE) Conference Series*, Vol. 7011
- Bradt, H. V. D., Ohashi, T., & Pounds, K. A. 1992, *ARA&A*, 30, 391
- Bregman, J. N., Canizares, C. R., Cen, R., et al. 2009, *Astronomy*, 2010, 24
- Brenneman, L., Miller, J., Nandra, P., et al. 2009, *Astronomy*, 2010, 26
- Collon, M. J., Günther, R., Ackermann, M., et al. 2008, in *Society of Photo-Optical Instrumentation Engineers (SPIE) Conference Series*, Vol. 7011
- Collon, M. J., Kraft, S., Günther, R., et al. 2006, in *Society of Photo-Optical Instrumentation Engineers (SPIE) Conference Series*, Vol. 6266
- Costa, E., Bellazzini, R., Bregeon, J., et al. 2008, in *Society of Photo-Optical Instrumentation Engineers (SPIE) Conference Series*, Vol. 7011
- Davis, J. E. 2001, *ApJ*, 562, 575
- Davis, J. E. 2002, in *High Resolution X-ray Spectroscopy with XMM-Newton and Chandra*, ed. G. Branduardi-Raymont
- Deutsche Forschungsgemeinschaft. 2003, *Status and Prospects of Astronomy in Germany 2003–2016 Memorandum*

- Ehle, M., de la Calle, I., Diaz Trigo, M., et al. 2008, XMM-Newton User's Handbook, 2nd edn., XMM-Newton SOC Team
- Evans, R. D. 1955, *The Atomic Nucleus* (McGraw-Hill Book Company (New York Toronto London))
- Fabian, A. C., Churazov, E., Donahue, M., et al. 2009, *Astronomy*, 2010, 73
- Fano, U. 1947, *Phys. Rev.*, 72, 26
- Ferrando, P., Arnaud, M., Briel, U., et al. 2009, in *American Institute of Physics Conference Series*, Vol. 1126, American Institute of Physics Conference Series, ed. J. Rodriguez & P. Ferrando, 3–8
- Ferrando, P., Arnaud, M., Briel, U., et al. 2006, in *Society of Photo-Optical Instrumentation Engineers (SPIE) Conference Series*, Vol. 6266
- Fiore, F., Arnaud, M., Briel, U., et al. 2008, *Memorie della Societa Astronomica Italiana*, 79, 38
- Fiore, F., Arnaud, M., Briel, U., et al. 2009, in *American Institute of Physics Conference Series*, Vol. 1126, American Institute of Physics Conference Series, ed. J. Rodriguez & P. Ferrando, 9–14
- Fischer, P., Andricek, L., Herrmann, S., et al. 2007, *Nuclear Instruments and Methods in Physics Research A*, 582, 843
- Fischer, P., Neeser, W., Trimpl, M., Ulrici, J., & Wermes, N. 2003, *Nuclear Instruments and Methods in Physics Research A*, 512, 318
- Forman, W., Jones, C., Cominsky, L., et al. 1978, *ApJS*, 38, 357
- Friedrich, P. 2008, *Wolter Optics*, ed. J. E. Trümper & G. Hasinger, *Astronomy and Astrophysics Library* (Springer (Berlin, Heidelberg)), 41–50
- Fritz, S. 2004, Master's thesis, Institut für Astronomie und Astrophysik der Universität Tübingen
- Galloway, D. K., Muno, M. P., Hartman, J. M., Psaltis, D., & Chakrabarty, D. 2008, *ApJS*, 179, 360
- Gatti, E. & Rehak, P. 1984, *Nucl. Instrum. Methods Phys. Res., Sect. A*, 225, 608
- Giacconi, R., Branduardi, G., Briel, U., et al. 1979, *ApJ*, 230, 540
- Giacconi, R., Gursky, H., Paolini, F. R., & Rossi, B. B. 1962, *Phys. Rev. Lett.*, 9, 439
- Gilli, R., Comastri, A., & Hasinger, G. 2007, *A&A*, 463, 79
- Heilmann, R. K., Ahn, M., & Schattenburg, M. L. 2008, in *Society of Photo-Optical Instrumentation Engineers (SPIE) Conference Series*, Vol. 7011
- Henke, B. L., Gullikson, E. M., & Davis, J. C. 1993, *Atomic Data and Nuclear Data Tables*, 54, 181
- Hering, E., Bressler, K., & Gutekunst, J. 2005, *Elektronik für Ingenieure und Naturwissenschaftler*, 5th edn. (Springer (Berlin, Heidelberg, New York))
- Horowitz, P. & Hill, W. 1999, *Die hohe Schule der Elektronik*, 4th edn. (Elektor-Verlag, Aachen)
- IXO-IWG. 2009, *IXO Payload Definition Document*, Tech. rep., ESA
- Jansen, F., Lumb, D., Altieri, B., et al. 2001, *A&A*, 365, L1
- Kang, S. X., Sun, X., Ju, X., et al. 2002, *Nuclear Instruments and Methods in Physics Research B*, 192, 365
- Kemmer, J. & Lutz, G. 1987, *Nucl. Instrum. Methods Phys. Res., Sect. A*, 253, 365
- . 1988, *Nucl. Instrum. Methods Phys. Res., Sect. A*, 273, 588
- Kemmer, J., Lutz, G., Prectel, U., et al. 1990, *Nucl. Instrum. Methods Phys. Res., Sect. A*, 288, 92
- Kendziorra, E., Colli, M., Kuster, M., et al. 1999, in *Society of Photo-Optical Instrumentation Engineers (SPIE) Conference Series*, ed. O. H. Siegmund & K. A. Flanagan, Vol. 3765, 204–214

- Kern, D. 2002, Einführung in die Halbleiterlehre, Lecture
- Kilbourne, C. A., Doriese, W. B., Bandler, S. R., et al. 2008, in Society of Photo-Optical Instrumentation Engineers (SPIE) Conference Series, Vol. 7011
- Kimmel, N., Hartmann, R., Holl, P., et al. 2006a, in Society of Photo-Optical Instrumentation Engineers (SPIE) Conference Series, ed. D. A. Dorn & A. D. Holland, Vol. 6276
- Kimmel, N., Hiraga, J. S., Hartmann, R., Meidinger, N., & Strüder, L. 2006b, Nucl. Instrum. Methods Phys. Res., Sect. A, 568, 128
- Kirsch, M. 2003, In-Orbit-Kalibration der EPIC-pn-Kamera auf XMM-Newton in hoch zeitauflösenden Modes und Pulsphasenspektroskopie des Crab-Pulsars, Dissertation, Institut für Astronomie und Astrophysik der Universität Tübingen
- Kirsch, M. G., Briel, U. G., Burrows, D., et al. 2005, in Society of Photo-Optical Instrumentation Engineers (SPIE) Conference Series, ed. O. H. W. Siegmund, Vol. 5898, 22–33
- Klein, P., Cesura, G., Fischer, P., et al. 1997, Nucl. Instrum. Methods Phys. Res., Sect. A, 392, 254
- Knoll, G. F. 2000, Radiation Detection and Measurement, 3rd edn. (John Wiley & Sons (New York, Chichester, Weinheim, Brisbane, Toronto, Singapore))
- Kokubun, M., Nakazawa, K., Watanabe, S., et al. 2008, in Society of Photo-Optical Instrumentation Engineers (SPIE) Conference Series, Vol. 7011
- Komitee für Astroteilchenphysik. 2006, Astroteilchenphysik in Deutschland
- Koyama, K., Tsunemi, H., Dotani, T., et al. 2007, PASJ, 59, 23
- Kuster, M., Cebrián, S., Rodríguez, A., et al. 2005, in Society of Photo-Optical Instrumentation Engineers (SPIE) Conference Series; UV, X-Ray, and Gamma-Ray Space Instrumentation for Astronomy XIV., ed. O. H. W. Siegmund, Vol. 5898, 236–246
- Kuulkers, E., den Hartog, P. R., in't Zand, J. J. M., et al. 2003, A&A, 399, 663
- Laurent, P., Lechner, P., Authier, M., et al. 2008, Memorie della Societa Astronomica Italiana, 79, 32
- Leahy, D. A., Darbro, W., Elsner, R. F., et al. 1983, ApJ, 266, 160
- Lechner, P., Andricek, L., Briel, U., et al. 2008, in Society of Photo-Optical Instrumentation Engineers (SPIE) Conference Series, Vol. 7021
- Lechner, P., Andricek, L., Heinzinger, K., et al. 2006, in Nuclear Science Symposium Conference Record IEEE, Vol. 3, 1595–1604
- Lechner, P., Fiorini, C., Hartmann, R., et al. 2001, Nucl. Instrum. Methods Phys. Res., Sect. A, 458, 281
- Leo, W. R. 1993, Techniques for Nuclear and Particle Physics, 2nd edn. (Springer (Berlin, Heidelberg, New York, London, Paris, Tokyo, Hong Kong, Barcelona, Budapest))
- Lumb, D. H. 2000, Experimental Astronomy, 10, 439
- Lutz, G. 1999, Semiconductor Radiation Detectors, 1st edn. (Springer (Berlin, Heidelberg, New York, Barcelona, Hong Kong, London, Milan, Paris, Tokyo))
- Lutz, G. 2005, Nuclear Instruments and Methods in Physics Research A, 549, 103
- . 2006, Journal of Synchrotron Radiation, 13, 99
- Lutz, G., Andricek, L., Eckardt, R., et al. 2007a, Nuclear Instruments and Methods in Physics Research A, 572, 311
- Lutz, G., Andritschke, R., Andricek, L., et al. 2007b, Nuclear Instruments and Methods

- in *Physics Research A*, 580, 960
- Lutz, G., Buttler, W., Bergmann, H., et al. 1988, *nimpra*, 263, 163
- McEntaffer, R. L., Cash, W., & Shipley, A. 2008, in *Society of Photo-Optical Instrumentation Engineers (SPIE) Conference Series*, Vol. 7011
- Meidinger, N., Andricek, L., Bonerz, S., et al. 2004, in *Society of Photo-Optical Instrumentation Engineers (SPIE) Conference Series; X-Ray and Gamma-Ray Instrumentation for Astronomy XIII*, ed. K. A. Flanagan & O. H. W. Siegmund, Vol. 5165, 26–36
- Meidinger, N., Andritschke, R., Hälker, O., et al. 2006, in *Society of Photo-Optical Instrumentation Engineers (SPIE) Conference Series; High Energy, Optical, and Infrared Detectors for Astronomy II*, ed. D. A. Dorn & A. D. Holland, Vol. 6276
- Meuris, A., Limousin, O., Lugiez, F., et al. 2009, in *American Institute of Physics Conference Series*, Vol. 1126, American Institute of Physics Conference Series, ed. J. Rodriguez & P. Ferrando, 25–30
- Miller, J., Nowak, M., Nandra, P., et al. 2009, *Astronomy*, 2010, 208
- Mitsuda, K., Bautz, M., Inoue, H., et al. 2007, *PASJ*, 59, 1
- Müller, R. 1991, *Grundlagen der Halbleiter-Elektronik*, 6th edn. (Springer (Berlin, Heidelberg, New York, Barcelona, London, Paris, Tokyo, Hong Kong, Barcelona, Budapest))
- Nandra, K. 2009, *Astronomy*, 2010, 220
- Oosterbroek, T. 2009, HTRS: sizing and positioning for IXO CDF design, Tech. rep., ESA
- Owens, A. & Peacock, A. 2004, *Nuclear Instruments and Methods in Physics Research A*, 531, 18
- Paerels, F., Méndez, M., Agueros, M., et al. 2009, *Astronomy*, 2010, 230
- Pareschi, G., Attinà, P., Basso, S., et al. 2008, in *Society of Photo-Optical Instrumentation Engineers (SPIE) Conference Series*, Vol. 7011
- Perić, I. 2004, PhD thesis, Universität Bonn
- Perotti, F. & Fiorini, C. 1999, *Nuclear Instruments and Methods in Physics Research A*, 423, 356
- Pfeffermann, E., Briel, U. G., Hippmann, H., et al. 1987, in *Society of Photo-Optical Instrumentation Engineers (SPIE) Conference Series*, Vol. 733, 519
- Popp, M., Hartmann, R., Soltau, H., et al. 2000, *Nuclear Instruments and Methods in Physics Research A*, 439, 567
- Porro, M., Ferrari, G., Fischer, P., et al. 2006, *IEEE Transactions on Nuclear Science*, 53, 401
- Predehl, P., Hasinger, G., Böhringer, H., et al. 2006, in *Society of Photo-Optical Instrumentation Engineers (SPIE) Conference Series; Space Telescopes and Instrumentation II: Ultraviolet to Gamma Ray*, ed. M. J. L. Turner & G. Hasinger, Vol. 6266
- Psaltis, D. 2006, *Accreting neutron stars and black holes: a decade of discoveries*, ed. W. H. G. Lewin & M. van der Klis (Cambridge University Press), 1–38
- Schanz, T., Tenzer, C., Maier, D., Kendziorra, E., & Santangelo, A. 2009, in *American Institute of Physics Conference Series*, Vol. 1126, American Institute of Physics Conference Series, ed. J. Rodriguez & P. Ferrando, 31–34
- Scholze, F., Henneken, H., Kuschnerus, P., et al. 1999, *Nuclear Instruments and Methods in Physics Research A*, 439, 208
- Spieler, H. 2006, *Semiconductor Detector Systems*, ed. R. J. Nicolas & H. Kamimura, *Semiconductor Science and Technology* (Oxford University Press)
- Stefanescu, A., Bautz, M. W., Burrows,

- D. N., et al. 2009, *Nucl. Instrum. Methods Phys. Res., Sect. A*, submitted
- Strohmayer, T. & Bildsten, L. 2006, *New views of thermonuclear bursts*, ed. W. H. G. Lewin & M. van der Klis (Cambridge University Press), 113–156
- Strüder, L. 2000, *Nucl. Instrum. Methods Phys. Res., Sect. A*, 454, 73
- Strüder, L., Bräuninger, H., Meier, M., et al. 1990, *Nuclear Instruments and Methods in Physics Research A*, 288, 227
- Strüder, L., Briel, U., Dennerl, K., et al. 2001, *A&A*, 365, L18
- Strüder, L., Enghauser, J., Hartmann, R., et al. 2003, *Nuclear Instruments and Methods in Physics Research A*, 512, 386
- Strüder, L., Hasinger, G., Holl, P., et al. 2004, in *Society of Photo-Optical Instrumentation Engineers (SPIE) Conference Series; X-Ray and Gamma-Ray Instrumentation for Astronomy XIII*, Vol. 5165, 10–18
- Strüder, L. & Meidinger, N. 2008, *CCD Detectors*, ed. J. E. Trümper & G. Hasinger, *Astronomy and Astrophysics Library* (Springer (Berlin, Heidelberg)), 51–71
- Strüder, L. & Moser, H. G. 2007, *The MPI Halbleiterlabor - Research Activities*
- Sze, S. M. 1981, *Physics of semiconductor devices*, 2nd edn. (Wiley)
- Tagliaferri, G., Basso, S., Borghi, G., et al. 2009, in *American Institute of Physics Conference Series*, Vol. 1126, *American Institute of Physics Conference Series*, ed. J. Rodriguez & P. Ferrando, 35–40
- Tenzer, C. 2008, PhD thesis, Institut für Astronomie und Astrophysik der Universität Tübingen
- Thompson, A., Attwood, D., Gullikson, E., et al. 2001, *X-ray Data Booklet*, Lawrence Berkeley National Laboratory, University of California, Berkeley, CA 94720
- Tietze, U. & Schenk, C. 2002, *Halbleiter-Schaltungstechnik*, 12th edn. (Springer (Berlin, Heidelberg, New York))
- Tomsick, J. A., Remillard, R. A., Kaaret, P., Barret, D., & Schnittman, J. 2009, *Astronomy*, 2010, 298
- Treis, J. 2005, *Large format CCD/DEPFET arrays*, Tech. rep., ESA
- Treis, J., Andritschke, R., Hartmann, R., et al. 2009, *Journal of Instrumentation*, 3, 3012
- Treis, J., Bombelli, L., Eckart, R., et al. 2006a, in *Society of Photo-Optical Instrumentation Engineers (SPIE) Conference Series; High Energy, Optical, and Infrared Detectors for Astronomy II*, ed. D. A. Dorn & A. D. Holland, Vol. 6276
- Treis, J., Fischer, P., Hälker, O., et al. 2004, in *Society of Photo-Optical Instrumentation Engineers (SPIE) Conference Series; Optical and Infrared Detectors for Astronomy*, ed. J. D. Garnett & J. W. Beletic, Vol. 5501, 89–100
- Treis, J., Fischer, P., Hälker, O., et al. 2005a, *IEEE Transactions on Nuclear Science*, 52, 1083
- , 2006b, *Nuclear Instruments and Methods in Physics Research A*, 568, 191
- Treis, J., Fischer, P., Hälker, O., et al. 2005b, in *Society of Photo-Optical Instrumentation Engineers (SPIE) Conference Series; UV, X-Ray, and Gamma-Ray Space Instrumentation for Astronomy XIV*, ed. O. H. W. Siegmund, Vol. 5898, 256–266
- Turner, M. & Hasinger, G. 2007, *XEUS - Physics of the Hot Evolving Universe*, Tech. rep., ESA
- Turner, M. J. L., Abbey, A., Arnaud, M., et al. 2001, *A&A*, 365, L27
- Ulrici, J., Fischer, P., Klein, P., et al. 2005, *Nuclear Instruments and Methods in Physics Research Section A*, 547, 424
- Weisskopf, M. C., Brinkman, B., Canizares, C., et al. 2002, *PASP*, 114, 1
- Wells, A. A., Gehrels, N. A., White, N. E., et al. 2004, in *Society of Photo-Optical*

- Instrumentation Engineers (SPIE) Conference Series; UV and Gamma-Ray Space Telescope Systems, ed. G. Hasinger & M. J. L. Turner, Vol. 5488, 403–414
- White, N. E. & Peacock, A. 1988, *Memorie della Societa Astronomica Italiana*, 59, 7
- Willingale, R. 2008, unpublished report
- Winkler, C., Courvoisier, T. J.-L., Di Cocco, G., et al. 2003, *A&A*, 411, L1
- Wölfel, S. 2007, PhD thesis, Halbleiterlabor der Max-Planck-Institute für Physik und für extraterrestrische Physik
- Wölfel, S., Herrmann, S., Lechner, P., et al. 2006, *Nuclear Instruments and Methods in Physics Research A*, 566, 536
- Wolter, H. 1952, *Annalen der Physik*, 445, 94
- Zhang, C., Lechner, P., Lutz, G., et al. 2006, *Nuclear Instruments and Methods in Physics Research A*, 568, 207
- , 2008a, *Nuclear Instruments and Methods in Physics Research A*, 588, 389
- Zhang, W. W., Bolognese, J., Byron, G., et al. 2008b, in *Society of Photo-Optical Instrumentation Engineers (SPIE) Conference Series*, Vol. 7011
- Zombeck, M. 2007, *Handbook of Space Astronomy and Astrophysics*, 3rd edn. (Handbook of Space Astronomy and Astrophysics: Third Edition, by Martin Zombeck, Published by Cambridge University Press, Cambridge, UK, 2007.)

Acknowledgements

Many people deserve my gratitude for helping me during my PhD thesis, among them are:

Prof. Dr. Andrea Santangelo, for the possibility to write an experimental thesis in astronomy and for always having an “open” door when it was necessary and providing advice when needed.

Prof. Dr. Jörn Wilms, who is with his enthusiasm and dedication to astronomy always an inspiring source of motivation. The simulations would not have been possible without his continuous support and advice in the first place.

Dr. Eckhard Kendziorra, for his mentoring throughout all the years. He ALWAYS had an idea where to look for when things did not work as they were intended to. His ability to find money to pay for laboratory equipment and travel expenses is unrivaled.

Dr. Thorsten Nagel, for the many discussions about astronomy and for the day-to-day support in academic life. He and Dr. Ingo Kreykenbohm always found time for me and my “Ich habe da mal eine IDL-Frage”.

Giuseppe Distratis, for the not only theoretical assembly and disassembly of various pieces of hardware and for many stimulating conversations about, but not limited to, physics. In the course of the years, he became a true friend.

Without the help and the knowledge of Olaf Lutz, Wolfgang Gäbele, Siegbert Renner, and Klaus Lehmann from the electronic and mechanic work shop, the laboratory setup would not have been possible.

In the collaboration with the MPI HLL, Peter Lechner, Johannes Treis, and Sven Herrmann deserve a special thanks.

The “Bamberger Jungs und Mädels” for their warm welcome during my regular stays at the Dr. Remeis-Sternwarte, especially Christian Schmid for the in-depth discussions about the simulations and the joint code debugging.

The members of the institute, especially the Espresso Runde and #ait, which help to form the friendly and open working environment of IAAT. Daniel Kusterer, Slawomir Suchy and Ruth Kowalski for their friendship and many comforting coffee breaks. Agnes Hoffmann, Sonja Fritz and Chris Tenzer for sharing the ups and downs of a PhD thesis.

My office mate Stefan Schwarzburg for many discussions about programming, computers and operating systems. His programming tips helped to ease the daily work. Together we shared some music and the one or the other small game. By the way Stefan, the coffee is ready! :-)

My parents who have always believed in me and supported me in any conceivable way.

Last but not least I need to thank Wiebke for her unconditional support and understanding throughout all these years and the patience during the last couple of months. Without her help I would not have been able to do this thesis at all.

Curriculum vitae

- 22.06.1977 born in Mutlangen, Germany
09.1983 – 06.1987 Elementary School (Grundschule) Mutlangen
09.1987 – 06.1993 Secondary School (Realschule) Mutlangen
09.1993 – 06.1996 Technical High School (Technisches Gymnasium)
Schwäbisch Gmünd
06.1996 High-School Graduation
07.1996 – 04.1997 Military Service (German Air Force)
10.1997 – 10.2004 Eberhard Karls University Tübingen
major: physics
08.2000 – 06.2001 Montana State University, Bozeman, major: physics
07.2003 – 08.2004 Preparation of Diploma-Thesis: “Eigenschaften von
Detektoren für den schnellen Auslesekanal auf XEUS”
under the supervision of R. Staubert at the Eberhard
Karls Universität Tübingen; Institute of Astronomy
and Astrophysics (IAAT)
10.2004 Diploma
11.2004 – Scientific employee at the IAAT
11.2004 – 08.2009 Preparation of this thesis entitled “Development of
high throughput X-ray instrumentation for fast timing
studies” under the supervision of Prof. A. Santangelo
and Prof. J. Wilms (U. Erlangen-Nuremberg) at the
IAAT

My academic teachers have been the professors and lecturers:

- Applied Physics* : D. Kern, E. Plies, D. Wharam
Astronomy and Astrophysics : A. Santangelo, R. Staubert, K. Werner, J. Wilms
Chemistry : H. Ebert, J. Strähle
Experimental Physics : H. Clement, F. Gönnerwein, P. Grabmayr,
: W. Hartmann, R. Hübener, R. Kleiner, O. Lutz,
: G. Wagner, C. Zimmermann
Mathematics : H. Kaul, M. Wolff
Theoretical Physics : R. Avci, B. Link, H. Mütter, H. Reinhardt

Lebenslauf

- 22.06.1977 geboren in Mutlangen
09.1983 – 06.1987 Grundschule Mutlangen
09.1987 – 06.1993 Realschule Mutlangen
09.1993 – 06.1996 Technisches Gymnasium Schwäbisch Gmünd
06.1996 Abitur
07.1996 – 04.1997 Grundwehrdienst
10.1997 – 10.2004 Eberhard Karls Universität Tübingen
Studiengang: Diplom Physik
08.2000 – 06.2001 Montana State University, Bozeman, Physikstudium
07.2003 – 08.2004 Anfertigung der Diplomarbeit: “Eigenschaften von Detektoren für den schnellen Auslesekanal auf XEUS” unter Anleitung von R. Staubert an der Eberhard Karls Universität Tübingen; Institut für Astronomie und Astrophysik (IAAT)
10.2004 Diplom
11.2004 – Wissenschaftlicher Angestellter am IAAT
11.2004 – 08.2009 Anfertigung der Dissertation “Development of high throughput X-ray instrumentation for fast timing studies” unter Anleitung von Prof. A. Santangelo und Prof. J. Wilms (Universität Erlangen-Nürnberg) am IAAT

Meine akademischen Lehrer waren die Professoren und Dozenten:

- Angewandte Physik* : D. Kern, E. Plies, D. Wharam
Astronomie und Astrophysik : A. Santangelo, R. Staubert, K. Werner, J. Wilms
Chemie : H. Ebert, J. Strähle
Experimentalphysik : H. Clement, F. Gönnerwein, P. Grabmayr,
: W. Hartmann, R. Hübener, R. Kleiner, O. Lutz,
: G. Wagner, C. Zimmermann
Mathematik : H. Kaul, M. Wolff
Theoretische Physik : R. Avci, B. Link, H. Müther, H. Reinhardt